Next generation organic light-emitting diode system technology based on NEMS/MEMS

NEMS/MEMS による次世代有機 EL システム技術に関する研究

July 2018

Hiroyuki KUWAE

桑江　博之

Next generation organic light-emitting diode system technology based on NEMS/MEMS

NEMS/MEMS による次世代有機 EL システム技術に関する研究

July 2018

Hiroyuki KUWAE

桑江　博之

Waseda University

Graduate School of Advanced Science and Engineering

Department of Nanoscience and Nanoengineering

Research on Microsystems

Committee:

Professor
Dr. Shuichi Shoji
Faculty of Science and Engineering
Waseda University

Professor
Dr. Hiroshi Kawarada
Faculty of Science and Engineering
Waseda University

Professor
Dr. Takashi Tanii
Faculty of Science and Engineering
Waseda University

Professor
Dr. Jun Mizuno
Research Organization for Nano and Life Innovation
Waseda University

Next-generation organic light-emitting system technology based on NEMS/MEMS

by

Hiroyuki Kuwae

Submitted to the Department of Nanoscience and Nanoengineering in July 2018, in partial fulfillment of the requirements for the degree of Doctor of Engineering

Abstract

A next-generation organic light-emitting diode (OLED) system based on nano- and microelectromechanical systems (NEMS/MEMS) is presented. A key achievement in this work is the improvement of the properties of the OLED system by utilizing the concept of NEMS/MEMS; that is, controlling mechanical and electrical characteristics by nano- or microscale fine structuring. This approach enables functionalization of OLEDs without depending on organic materials. A novel strategy to fabricate nanostructures for optoelectronics devices using ultraviolet nanoimprint lithography is presented in Chapter 2. Chapter 3 and 4 present methods to modulate glass properties by nanopatterning and the properties of indium tin oxide by micropatterning, respectively. Improvement of the optoelectronic properties of OLEDs by fabricating a nanopatterned current flow region is discussed in Chapter 5. The developed highly functionalized OLED system not only should become a fundamental technology for next-generation OLEDs, but also represents a breakthrough for organic electronic devices.

Thesis Supervisor: Shuichi Shoji

Title: Professor

Acknowledgment

Twenty years have passed since I admired a scientist in my first year of elementary school. Here, I have completed my doctoral thesis and graduated from the doctoral course at Waseda University. All of the results presented here were achieved with the support of many contributors and collaborators.

I would like to express my sincere gratitude to my advisor, Prof. Shuichi Shoji at the faculty of Science and Engineering of Waseda University for his continuous support of my Ph.D. study with his enthusiasm and immense knowledge. He has inspired me to pursue such a career in the MEMS field. I am glad to have belonged to his exciting laboratory.

My sincere thanks also go to Prof. Jun Mizuno at the Research Organization for Nano and Life Innovation, Waseda University. His guidance helped me in all the time of daily research, but more importantly, provided mentorship for my professional and personal development. I am blessed to have had this opportunity to conduct research with him.

I would like to deeply thank to my dissertation committee, Prof. Hiroshi Kawarada and Prof. Takashi Tanii at the faculty of Science and Engineering of Waseda University, for finding the time in their busy schedules to review my doctoral thesis. They gave me insightful comments and support and fruitful comments to improve this thesis.

I am thankful to Prof. Tetsushi Sekiguchi. He always gave me appropriate advice, especially regarding a presentation for my doctor course entrance exam and writing funding applications. I would also like to thank Ms. Reiko Nishikiori for all of her kind support.

I would like to thank all of the Prof. Shoji laboratory members. I express my appreciation to Dr. Takashi Kasahara for showing me the “style” of a Ph.D. Dr. Akiko Okada and Dr. Masatsugu Nimura kindly supported me with their considerate advice. I acknowledge my colleagues who shared the laboratory with me and provided encouragement: Mr. Takenari Sudo, Masaki Oyama, Kaneko Yuji, Shinya

Yamada, Ayaka Iguchi, and Masanori Kono. Dr. Hidetoshi Shinohara, Dr. Kentaro Ishibashi, Dr, Weixin Fu, Dr. Dong Hyum Yoon, Dr. Daiki Tanaka, Mr. Tsubasa Funabashi, Mr. Hayata Mimatsu, Ms. Miho Tsuwaki, Mr. Toru Takiguchi, Mr. Hirokazu Noma, Mr. Bo Ma, Mr. Naofumi Kobayashi, Mr. Tasushi Kaneda, Mr. Kazuya Nomura, Mr. Nakanishi Kanki, Mr. Bingyang Xu, Mr. Atsuki Nobori, Ms. Haruka Suzaki, Mr. Hayate Yamazaki, Mr. Kosuke Sakamoto, Mr. Takumi Kamibayashi, Mr. Seren Maeda, Mr. Kenichi Atsumi, Ms. Mayuko Shiozawa, Mr. Keito Miwa, Mr. Kosuke Yamada, Ms. Akari Otsuka, and Ms Akiko Fujiwara have helped and supported me. I have learned so much from our daily discussions and enjoyed working with you.

I would also like to extend my gratitude to Prof. Chihaya Adachi at Kyushu University for providing helpful comments that aided the OLED research. It was an amazing experience and honor for me to join the ERATO project organized by him. In addition, I acknowledge the following members from his laboratory: Dr. Kou Yoshida, Dr. Munetomo Inoue, Mr. Atushi Nitta, and Mr. Yu Shiihara; OLEDs were an uncharted field for me, and their discussions with me were valuable.

Although not all of their names are included here, I thank all of the people who have collaborated with me.

Finally, yet most importantly, I give my faithful gratitude to my parents, Yoshiyuki and Yasuko, and my sister, Yuki for their selfless love and perpetual support all my life. I sincerely express my appreciation to my partner, Chiaki Uehara. You have stayed with me all the time. This work is dedicated to you all.

Contents

List of figures and tables

List of abbreviations

AFM	Atomic force microscopy
ALD	Atomic layer deposition
ASE	Amplified spontaneous emission
CV	Cyclic voltammetry
DC	Direct current
EB	Electron beam
EL	Electroluminescence
EQE	External quantum efficiency
FRET	Förster resonance energy transfer
HOMO	Highest occupied molecular orbital
IC	Integrated circuit
ICP-RIE	Inductively coupled plasma reactive ion etching
ISC	Intersystem crossing
ITO	Indium tin oxide
LOS	Liquid organic semiconductor
LUMO	Lowest occupied molecular orbital
MEMS	Microelectromechanical system
NEMS	Nanoelectromechanical system
NGL	Next-generation lithography
NIL	Nanoimprint lithography
OLED	Organic light-emitting diode
OSLD	Organic semiconductor laser diode
PES	Photoemission spectroscopy
PET	Polyethylene terephthalate
PL	Photoluminescence
PLQY	Photoluminescence quantum yield
RF	Radio frequency
RIE	Reactive ion etching
RISC	Reverse intersystem crossing
SAM	Self-assembled monolayer
SCE	Saturated calomel electrode
SEM	Scanning electron microscopy
SHA	Singlet–heat annihilation
SPA	Singlet–polaron annihilation

SSA	Singlet–singlet annihilation
STA	Singlet–triplet annihilation
TADF	Thermally activated delayed fluorescence
TTA	Triplet–triplet annihilation
UV	Ultraviolet
UV-vis	Ultraviolet–visible
VUV	Vacuum ultraviolet light gas

Chemical abbreviations

APTES	3-Aminopropyltriethoxysilane
Alq_3	Tris(8-hydroxyquinolinato)aluminum
BCP	2,9-Dimethyl-4,7-diphenyl-1,10-phenanthroline
BSB-Cz	4,4´-Bis[(N- carbazole)styryl]biphenyl
DPA	9,10-Diphenylanthracene
GaN	Gallium nitride
GOPTS	3-Glycidodyloxypropyltriethoxysilane
HMDS	Hexamethyldisilazane
MeCN	Acetonitrile
NLQ	1-Naphthaleneacetic acid 2-ethylhexyl ester
PLQ	1-Pyrenebutyric acid 2-ethylhexyl ester
PoPy2	Phenyldipyrenyl phosphine oxide
TMAH	Tetramethylammonium hydroxide
fac-$Ir(ppy)_3$	Fac-tris(2-phenylpyridine)iridium
mCP	N,N-Dicarbazolyl-3,5-benzene
α-NPD	4,4´-Bis[N-(1-naphthyl)-N-phenylamino]biphenyl

Chapter 1
Introduction

Organic electronic devices containing organic semiconductors currently attract huge attention because of their numerous favorable properties. Various organic electronic applications have been developed, such as organic light-emitting diodes (OLEDs), organic thin-film transistors, and organic photovoltaics [1]. Among these applications, OLEDs have reached the commercialization stage, capitalizing on their useful features including flexibility, surface emission, low driving voltage, high response speed, and material diversity. MarketsandMarkets™ estimated that the OLED market will grow at a compound average growth rate of 15.2% between 2017 and 2023, forecasting that it will reach 48.81 Billion USD by 2023 [2]. As compared with inorganic electronic devices, organic electronic devices have undeniable advantages in terms of their fabrication process. Fabrication of inorganic electronic devices generally requires temperatures of over 500 °C because they are formed using semiconductor manufacturing processes. In contrast, because organic electronic devices contain organic materials, they are fabricated with temperatures below 200 °C, which can lower the processing power consumption. In addition, organic compounds are typically soluble in organic solvent or water. Therefore, large-area and cost-effective processes can be used to produce printed electronics. Based on these superior features, OLEDs will become increasingly important devices in the future internet of things society. Further development of features such as flexibility and luminescence characteristics is needed to realize next-generation OLEDs.

This thesis presents a novel highly functionalized OLED system using nano- and microelectromechanical systems (NEMS/MEMS), which have been developed based on inorganic semiconductor technology. By combining with NEMS/MEMS, the characteristics of the proposed OLED system are improved without depending on the properties of organic materials. That is, the mechanical and electrical properties of the OLEDs are controlled using NEMS/MEMS fine structures.

1.1 Organic light-emitting diodes

Organic materials are generally composed of insulating carbon skeletons. In 1950, electrical conductivity of organic materials was first discovered by Akamatsu and Inokuchi [1-3]; these materials were called “organic semiconductors”. In 1953, Bernanose realized luminescence from a thin polymer film containing an organic dye by applying a strong alternating electric field [4]. He explained that the luminescence is based on an already known mechanism that does not require carrier injection, although the mechanism is understood as a secondary fluorescence of the organic dye excited by ultraviolet (UV) light from a glow discharge at the present time. Attempts to investigate electroluminescence (EL) by carrier injection were then made in the 1960s. Pope confirmed EL emission from a single crystal of anthracene (thickness = 10–20 μm) sandwiched between two silver paste electrodes driven by a direct current (DC) of 400 V [5]. In this experiment, a current density of 100 μA/cm^2 was injected. However, this was a low value because they used a thick single-crystal film. Bilayer OLEDs consisting of stacked thin films with different functions were proposed by Tang and VanSlyke in 1987, leading to a breakthrough in OLED research [6]. Their OLEDs had a p-type hole transport layer and n-type light-emitting electron transport layer composed of tris(8-hydroxyquinolinato)aluminum (Alq_3). Subsequently, Adachi [7] reported three-layer OLEDs with a structure of hole transport layer/emitting layer/electron transport layer, which subsequently became the basic device architecture of OLEDs.

The performance of OLEDs depends not only on device architecture but also on their component organic molecules, which have wide flexibility of molecular structure. When luminescence is produced by an electrical field, i.e., EL, an organic molecule is excited from its ground state to a singlet excited state or a triplet excited state to form a singlet or triplet exciton, respectively. Statistically, there is a 1:3 formation ratio of singlet to triplet excitons [8,9]. Thus, generally 25% of excited molecules emit fluorescence originating from singlet excitons and 75% of excited molecules emit phosphorescence originating from triplet excitons. First-generation OLEDs were based on fluorescent materials. From the 1980s, there was considerable

interest in phosphorescent materials as high-efficiency OLED emitters, although they required low temperature operation to realize phosphorescence. In 1999, Forrest and Thompson got an inspiration from a report by Watt's group [10], in which they mentioned that fac-tris(2-phenylpyridine)iridium (fac-Ir(ppy)$_3$) shows high internal quantum efficiency at room temperature, which sparked the development of high-performance phosphorescent OLEDs (second-generation OLEDs) [11]. Here, the external quantum efficiency (EQE: η_{ext}) of the OLED is given by the following equation:

$$\eta_{ext} = \gamma \times \beta \times \Phi \times \eta_p \quad (1.1)$$

where γ is the charge balance factor, β is the exciton production efficiency, Φ is the photoluminescence (PL) quantum efficiency (also called PLQY), and η_p is the light out-coupling efficiency. In addition, $\gamma \times \beta \times \Phi$ is called the internal quantum efficiency. The estimated theoretical limitation of η_{ext} of a fluorescent OLED is 5% (γ = 1, β = 25%, Φ = 100%, and η_p = 20%) [12]. In contrast, η_{ext} of reported phosphorescent OLEDs has reached 8% at room temperature. Phosphorescent materials can utilize both singlet and triplet excitons for phosphorescent emission by taking advantage of the intersystem crossing (ISC) from singlet to triplet excited states of nearly 100% in complexes containing metals such as osmium [13], platinum [14], and iridium [10,11]. Therefore, they can achieve an exciton production efficiency of 100% in theory. Phosphorescent materials are highly promising as emissive materials in OLEDs, although there remain several associated challenges: use of rare metals, exciton quenching at high current density, and difficulty fabricating OLEDs that emit blue phosphorescence. To overcome these issues, Endo and Adachi developed third-generation OLEDs using thermally activated delayed fluorescence (TADF) materials in 2009 [115]. Although TADF materials emit fluorescence, they show high internal quantum efficiency comparable to that of phosphorescent materials. The energy gap between the lowest singlet excited state and lowest triplet excited state of TADF materials is quite small. Thus, up-conversion from the lowest triplet excited state to the lowest singlet excited state, called reverse intersystem

crossing (RISC), can be achieved by thermal energy at room temperature (e.g., 0.026 eV at 300 K). In theory, an internal quantum efficiency of 100% can be realized by harvesting the triplet excitons, which are typically lost through nonradiative decay processes in fluorescent materials.

As described above, OLEDs have been developed mainly focusing on device architecture and novel organic molecules.

1.2 Beyond OLEDs

Since their initial reports, OLEDs have been continually researched with the aim of realizing high-performance devices and development of applications. From the viewpoints of organic molecules and device architecture, there have been studies on long persistent luminescent [16], water- and oxygen-resistant OLEDs [17], OLEDs using single fission (theoretical internal quantum efficiency > 100%) [18], high- performance OLEDs with TADF assisted fluorescence systems [19], and liquid OLEDs [20]. From the viewpoint of applications, there is huge interest in developing large-area and/or flexible OLEDs and high-power OLEDs, such as organic semiconductor laser diodes (OSLDs) [21,22]. Development of next-generation OLEDs requires attention from diverse standpoints, not only those of organic molecules and device architecture.

1.3 Nano/micro-electromechanical systems

Integrated circuit (IC) technology using inorganic semiconductors was started by Shockley at Nokia Bell Labs in 1947. Since then, transistor integration has been investigated for performance improvement, as can be seen in the progress of large-scale integration, very large-scale integration, and ultra-large-scale integration. Such transistor integration has been led by the proposal of Moore's law, which states that the number of transistors in an IC doubles every two years. This law became a basis for the international technology roadmap for semiconductors (ITRS) and powered the advance of our information society by the miniaturization of transistor size, although it has now reached the fundamental limitation in transistor

scaling. In 2007, ITRS defined the concept of "More than Moore" [23], which aims to promote integration of devices with various functions, whereas Moore's law promoted integration of the transistors in ICs. More than Moore means integration of not only ICs but also devices that cannot be realized by increasing of number of transistors, such as radio-frequency (RF) modules, sensors, and actuators. The concept of More than Moore may be used to realize system-in-package and system-on-chip technology. Organic electronics including OLEDs are thought to fit the More than Moore concept.

NEMS/MEMS is another technology that belongs to the More than Moore category. NEMS/MEMS based on inorganic semiconductor IC technology are integrated electronic components and actuators. Research on NEMS/MEMS began in about 1970 at Stanford University, and the name MEMS has been commonly used in the United States since 1987. The name NEMS started to be used when the miniaturization of device size became a focus. In NEMS/MEMS technology, devices are fabricated by forming nano/microscale fine structures. For example, a piezo pressure sensor consists of a thinned silicon membrane with resistance [24]. A change of outer pressure is detected as a piezoresistive effect induced by the stress generated in the silicon membrane [25]. Micropatterned boron-doped areas function as p-type piezoresistors and the piezoresistive effects has enhanced by thinning the silicon layer. Micro-total analysis systems are a type of MEMS consisting of micropumps, microchannels, microreactors, and sensors [26]. Of particular interest in this work is utilizing NEMS/MEMS concepts such as enhanced surface tension effects achieved by minimization of the channel width, and locally controlled thermal/pressure/electrical energy effects. Moreover, the formation of surface microstructure on silicon can alter it characteristics to give black silicon [27], which strongly absorbs light, or porous silicon [28], which can emit visible light.

1.3.1 NEMS/MEMS in inorganic light-emitting diodes

NEMS/MEMS technology or its concept has already been applied to inorganic light-emitting diodes (LEDs). A gallium nitride (GaN) substrate with a

SiO_2 nanomask, called nano-FIELO, was developed to improve the internal quantum efficiency of high-power LEDs [29]. The nanomask structure controls and suppresses generation of dislocations during epitaxial growth of GaN on a sapphire substrate. Moth-eye structures consisting of nanopatterns smaller than the emission wavelength of an LED can improve the EQE of inorganic LEDs by creating a graded refractive index medium that decreases the reflection of light [30]. Optical resonators, which are several times larger than the emission wavelength, are essential components of inorganic LED-based lasers.

1.3.2 NEMS/MEMS in OLEDs

NEMS/MEMS are considered to an important technology for not only inorganic LEDs but also next-generation OLEDs. Some research combining NEMS/MEMS and OLEDs has already been reported, although it simply involved changing the emission layer from an inorganic material to an organic material; for example, OLEDs with a light extraction structure [31]. In 2006, Matsushima reported an OLED containing a heat-sink structure to protect the heat-sensitive organic layers from Joule heating [32]. His report was based on the synthesis technology of NEMS/MEMS and OLEDs in the true sense of the word, i.e. changing the characteristics of OLEDs by nano/microscale fine structuring. Since then, few studies combining NEMS/MEMS and OLED technology have been reported until recently. Kasahara reported microfluidic OLEDs [33], which combined liquid OLEDs and microfluidic MEMS technology, to utilize the features of liquid organic semiconductors. Shim also combined liquid OLEDs and MEMS [34]; he prepared a backside reservoir for EL emission recovery by MEMS fabrication technology. Komino demonstrated in-plane anisotropic molecular orientation in a spin-coated film using one-dimensional fluid flow induced by microchannels [35]. Such studies are still sparse, so further development of novel NEMS/MEMS-based OLED systems is desired.

1.4 Theme of this thesis

This thesis addresses development of a novel highly functionalized OLED utilizing NEMS/MEMS. The concept of the thesis is illustrated in Fig. 1.1. The mechanical and electrical properties of the proposed OLED system are improved by nano- or microscale fine structuring. Next-generation OLEDs system are constructed by summing up developed technologies. This system enables to improve OLED performance without depending on the properties of the component organic materials. A brief outline of this thesis is depicted in Fig. 1.2 and described below.

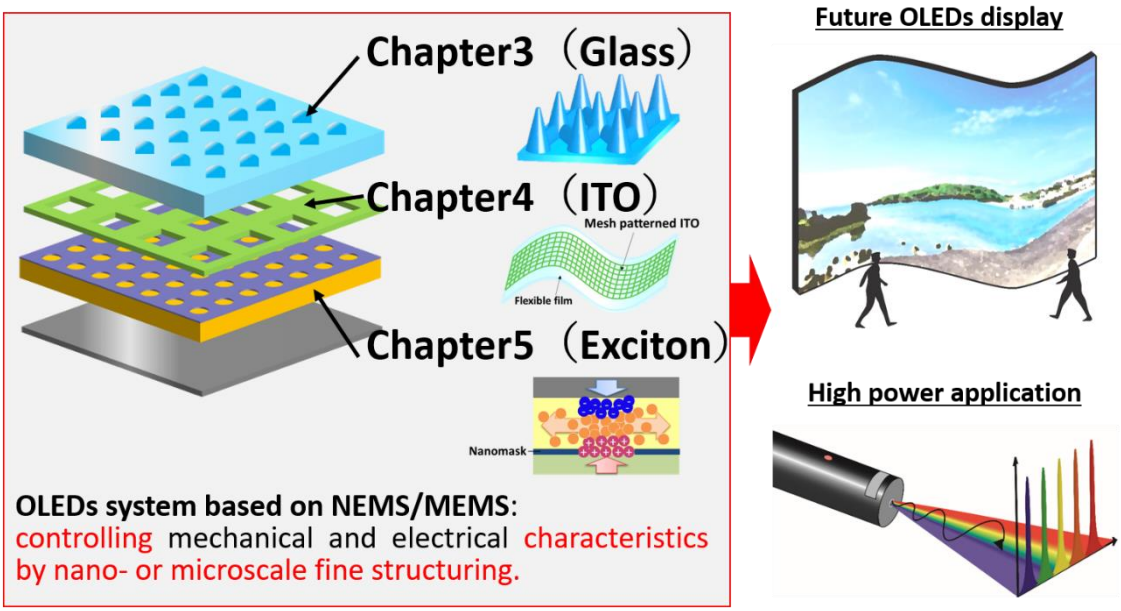

Figure 1.1 Concept of this thesis: an OLED system based on NEMS/MEMS.

Chapter 2, entitled "Nanofabrication method combining ultraviolet nanoimprint lithography and anisotropic wet etching," presents a novel strategy to fabricate nanostructures by UV-nanoimprint lithography (NIL). Nanofabrication processes have underpinned development of optoelectronic devices, and UV-NIL is one such promising technique. To enhance the potential of UV-NIL, we combine it with the NEMS/MEMS fabrication method anisotropic wet etching. The resolution of the method does not depend on that of the original imprint mold in the proposed method.

In Chapter 3, “Durable self-cleaning glass with bridged glass nanopillar,” we develop bridged glass nanopillar structures with high scratch resistance for use as self-cleaning glass. To maintain glass clean is important for OLED displays, and it can be achieved by self-cleaning effects using a superhydrophilic or -hydrophobic glass surface. The proposed glass nanopillar provides such wetting properties. Furthermore, the sub-micron bridge structure that connects each glass nanopillar increases the mechanical toughness of the nanopillars.

In Chapter 4, entitled “Flexible indium tin oxide with simple micromesh-patterning,” highly flexible transparent indium tin oxide (ITO) electrodes are developed for use in flexible OLEDs. Micromesh patterning of ITO lowers its tensile stress and hinders crack propagation. The proposed patterned ITO electrodes are fabricated by photolithography and wet etching. The resistance increase ratio of a mesh-patterned ITO electrode after bending 1000 times was at least two orders of magnitude lower than that of a planar ITO electrode.

Chapter 5 “Suppression of external quantum efficiency roll-off in nanopatterned organic light-emitting diodes” describes a novel methodology to suppress EQE roll-off caused by singlet–polaron annihilation (SPA). A nanopatterned resist mask layer on an ITO electrode allows the generated excitons to escape from the current flow region by decreasing the area of the current flow region to close to the exciton diffusion length. The current density at which the EQE was half of its initial value in the proposed OLEDs was approximately 41 times that of a conventional OLED without the nanopatterned mask layer. The dependence of roll-off suppression behavior on the size and shape of the nanopatterns was well explained by a SPA model that considered exciton diffusion.

Chapter 6 “Conclusion” presents a summary of the thesis and considers the broader implications of the results. Future prospects for next-generation OLED systems with NEMS/MEMS are also provided.

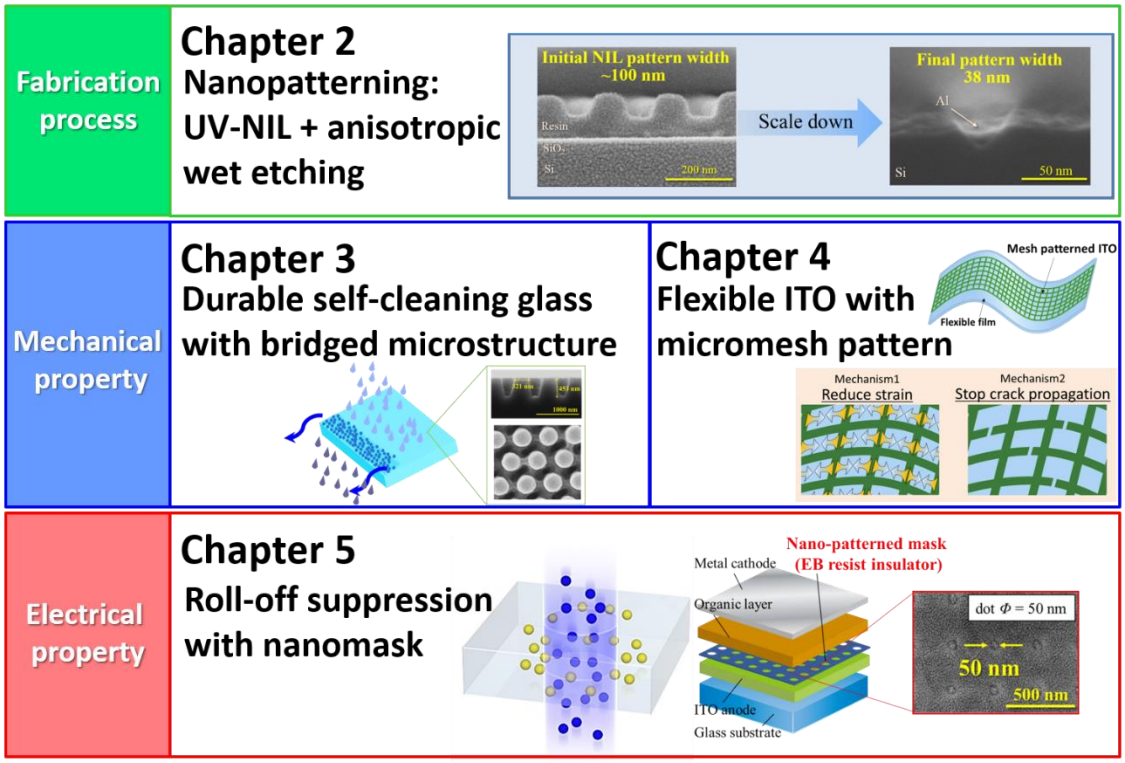

Figure 1.2 Brief outline of this thesis.

Reference

[1] S. Ogawa, Organic Electronics Materials and Devices, Springer, 2015.

[2] MarketstandMarkets™, OLED Market by Display Application (Smartphone, TV, Automotive, NTE), Panel Type (Rigid, Flexible), Technology, Size, Material (FMM RGB, WOLED), Lighting Application (General, Automotive), Panel Type, & Vertical, and Geography - Global Forecast to 2023, 2017.

[3] H. Akamatu and H. Inokuchi, "On the Electrical Conductivity of Violanthrone, Iso - Violanthrone, and Pyranthrone," J. Chem. Phys., vol. 18, pp. 810-811, 1950.

[4] A. Bernanose, M. Comte and P. Vouaux, "A new method of emission of light by certain organic compounds," J.Chim.Phys, vol. 50, pp. 64-68, 1953.

[5] M. Pope, H. Kallmann and P. Magnante, "Electroluminescence in organic crystals," J. Chem. Phys., vol. 38, pp. 2042-2043, 1963.

[6] C. W. Tang and S. A. VanSlyke, "Organic electroluminescent diodes," Appl. Phys. Lett., vol. 51, pp. 913-915, 1987.

[7] C. Adachi, S. Tokito, T. Tsutsui and S. Saito, "Electroluminescence in organic films with three-layer structure," Jpn. J. Appl. Phys., vol. 27, pp. L269, 1988.

[8] W. Helfrich and W. Schneider, "Recombination radiation in anthracene crystals," Phys. Rev. Lett., vol. 14, pp. 229, 1965.

[9] W. Helfrich and W. Schneider, "Transients of volume - controlled current and of recombination radiation in anthracene," J. Chem. Phys., vol. 44, pp. 2902-2909, 1966.

[10] K. King, P. Spellane and R. J. Watts, "Excited-state properties of a triply ortho-metalated iridium (III) complex," J. Am. Chem. Soc., vol. 107, pp. 1431-1432, 1985.

[11] M. Baldo, S. Lamansky, P. Burrows, M. Thompson and S. Forrest, "Very high-efficiency green organic light-emitting devices based on electrophosphorescence," Appl. Phys. Lett., vol. 75, pp. 4, 1999.

[12] J. Kim, P. K. Ho, N. C. Greenham and R. H. Friend, "Electroluminescence emission pattern of organic light-emitting diodes: Implications for device

efficiency calculations," J. Appl. Phys., vol. 88, pp. 1073-1081, 2000.

[13] Y. Ma, H. Zhang, J. Shen and C. Che, "Electroluminescence from triplet metal—ligand charge-transfer excited state of transition metal complexes," Synth. Met., vol. 94, pp. 245-248, 1998.

[14] S. Lamansky, P. Djurovich, D. Murphy, F. Abdel-Razzaq, H. Lee, C. Adachi, P. E. Burrows, S. R. Forrest and M. E. Thompson, "Highly phosphorescent bis-cyclometalated iridium complexes: synthesis, photophysical characterization, and use in organic light emitting diodes," J. Am. Chem. Soc., vol. 123, pp. 4304-4312, 2001.

[15] H. Uoyama, K. Goushi, K. Shizu, H. Nomura and C. Adachi, "Highly efficient organic light-emitting diodes from delayed fluorescence," Nature, vol. 492, pp. 234-238, 2012.

[16] R. Kabe and C. Adachi, "Organic long persistent luminescence," Nature, vol. 550, pp. 384, 2017.

[17] K. Morii, M. Ishida, T. Takashima, T. Shimoda, Q. Wang, M. K. Nazeeruddin and M. Grätzel, "Encapsulation-free hybrid organic-inorganic light-emitting diodes," Appl. Phys. Lett., vol. 89, pp. 183510, 2006.

[18] N. V. Korovina, S. Das, Z. Nett, X. Feng, J. Joy, R. Haiges, A. I. Krylov, S. E. Bradforth and M. E. Thompson, "Singlet fission in a covalently linked cofacial alkynyltetracene dimer," J. Am. Chem. Soc., vol. 138, pp. 617-627, 2016.

[19] H. Nakanotani, T. Higuchi, T. Furukawa, K. Masui, K. Morimoto, M. Numata, H. Tanaka, Y. Sagara, T. Yasuda and C. Adachi, "High-efficiency organic light-emitting diodes with fluorescent emitters," Nat. Commun., vol. 5, pp. 4016, 2014.

[20] D. Xu and C. Adachi, "Organic light-emitting diode with liquid emitting layer," Appl. Phys. Lett., vol. 95, pp. 207, 2009.

[21] F. Hide, M. A. Diaz-Garcia, B. J. Schwartz, M. R. Andersson, Q. Pei and A. J. Heeger, "Semiconducting polymers: a new class of solid-state laser materials," Science, vol. 273, pp. 1833-1836, 1996.

[22] M. Baldo, R. Holmes and S. Forrest, "Prospects for electrically pumped organic

lasers," Phys. Lett. B, vol. 66, pp. 035321, 2002.

[23] Semiconductor Industry Association, 2007 International Technology Roadmap for Semiconductors (ITRS). 2007.

[24] Y. Kanda and A. Yasukawa, "Hall-effect devices as strain and pressure sensors," Sensor. Actuator., vol. 2, pp. 283-296, 1981.

[25] C. S. Smith, "Piezoresistance effect in germanium and silicon," Phys. Rev., vol. 94, pp. 42, 1954.

[26] T. Vilkner, D. Janasek and A. Manz, "Micro total analysis systems. Recent developments," Anal. Chem., vol. 76, pp. 3373-3386, 2004.

[27] H. Jansen, M. de Boer, R. Legtenberg and M. Elwenspoek, "The black silicon method: a universal method for determining the parameter setting of a fluorine-based reactive ion etcher in deep silicon trench etching with profile control," J. Micromech. Microeng., vol. 5, pp. 115, 1995.

[28] A. Nishida, K. Nakagawa, H. Kakibayashi and T. Shimada, "Microstructure of visible light emitting porous silicon," Jpn. J. Appl. Phys., vol. 31, pp. L1219, 1992.

[29] A. Okada, S. Shoji, H. Shinohara, H. Goto, H. Sunakawa, T. Matsueda, A. Usui, A. A. Yamaguchi and J. Mizuno, "Fabrication of low dislocation density GaN template by nano-channel FIELO using nanoimprint lithography," J. Photopolym. Sci. Technol., vol. 26, pp. 69-72, 2013.

[30] H. Ono, Y. Ono, K. Kasahara, J. Mizuno and S. Shoji, "Fabrication of high-intensity light-emitting diodes using nanostructures by ultraviolet nanoimprint lithography and electrodeposition," Jpn. J. Appl. Phys., vol. 47, pp. 933, 2008.

[31] B. J. Matterson, J. M. Lupton, A. F. Safonov, M. G. Salt, W. L. Barnes and I. D. Samuel, "Increased Efficiency and Controlled Light Output from a Microstructured Light - Emitting Diode," Adv. Mater., vol. 13, pp. 123-127, 2001.

[32] T. Matsushima, H. Sasabe and C. Adachi, "Carrier injection and transport characteristics of copper phthalocyanine thin films under low to extremely high

current densities," Appl. Phys. Lett., vol. 88, pp. 033508, 2006.

[33] T. Kasahara, S. Matsunami, T. Edura, J. Oshima, C. Adachi, S. Shoji and J. Mizuno, "Fabrication and performance evaluation of microfluidic organic light emitting diode," Sens. Actuators. A Phys., vol. 195, pp. 219-223, 2013.

[34] C. Shim, S. Hirata, J. Oshima, T. Edura, R. Hattori and C. Adachi, "Uniform and refreshable liquid electroluminescent device with a back side reservoir," Appl. Phys. Lett., vol. 101, pp. 113302, 2012.

[35] T. Komino, H. Kuwae, A. Okada, W. Fu, J. Mizuno, J. Ribierre, Y. Oki and C. Adachi, "In-Plane Anisotropic Molecular Orientation of Pentafluorene and Its Application to Linearly Polarized Electroluminescence," ACS Appl. Mater. Interfaces, vol. 9, pp. 27054-27061, 2017.

Chapter 2
Novel nanofabrication method combining ultraviolet nanoimprint lithography and anisotropic wet etching

Nanofabrication methods are the basis of the proposed OLED system. In this chapter, a novel strategy to fabricate nanostructures, which combines UV-NIL and anisotropic wet etching, is presented. The resolution of the proposed method does not depend on that of the original imprint mold. Atomically sharp V-shaped grooves are formed by anisotropic wet etching using an SiO_2 etching mask fabricated by NIL. Atomic-scale precision is prepared by anisotropic etching using tetramethylammonium hydroxide (TMAH) solution containing a small amount of surfactant at room temperature. Using the V-shaped grooves as a template, Al_2O_3/Al is deposited and then etched by angled Ar-ion milling after planarization with thick resin. Sub-50-nm metal structures were achieved with 62% size reduction of the initial mold structure.

The contents of this chapter have been published in the following journal article:

"Sub-50-nm structure patterning by combining nanoimprint lithography and anisotropic wet etching without considering original mold resolution", Microelectronic Engineering, vol. 169, pp. 39–42, 2017 [1].

2.1 Introduction

Nanofabrication processes have underpinned the development of optoelectronic devices including OLEDs [2-4], semiconductor ICs [5-7], and nanofluidic devices [8]. Fine patterning techniques that can create feature sizes that conventional photolithography cannot achieve are required for further technological development. The resolution of conventional photolithography (CD) is given by

$$\mathrm{CD} = k_1 \lambda / NA \tag{2.1}$$

where k_1 is the resolution factor related to all the other processes, NA is the numerical aperture of the optical system, and λ is the wavelength. CD is limited in a conventional lithography system ($\lambda = 193$ nm, $NA > 1$ in KrF immersion lithography) [9]. A number of next-generation lithography (NGL) techniques including electron beam (EB) lithography [10], extreme UV lithography [11], multi-patterning [12], directed self-assembly lithography [13,14], and NIL [5,6,15-18] have been developed.

UV-NIL has attracted attention as a promising NGL technique to fabricate nanometer-scale patterns in a large area [15-17]. NIL was first developed by Chou at Princeton University in 1995 using a thermoplastic resin; this process was coined thermal-NIL [5]. Heisman demonstrated UV-NIL using a UV-curable resin a year later [15]. As compared with other technologies, UV-NIL is a simple nanolithography process that is low-cost, high-throughput, and has high dimensional precision. Sub-nanometer NIL patterning has been reported and NIL still has potential for higher resolution patterning [18]. In UV-NIL, a resist pattern is fabricated by deforming the physical shape of the resist, meaning that the size of imprinted pattern is limited by the quality and scale of the NIL mold. Thus, a high-quality fine nanoscale mold is required for high-resolution patterning. Recently, Peroz developed sub-10-nm NIL with a hydrogen silsesquioxane fine mold coated with Al_2O_3 by atomic layer deposition (ALD) [17]. An atomic-scale (0.3 nm) stepped polymer pattern fabricated with a stepped sapphire mold has been reported by Tan [18]. Although fine nanoscale UV-NIL patterns have been obtained, most of them have used specially fabricated

molds. Therefore, the preparation of a high-quality fine mold is a major barrier to improving the NIL process.

In this work, we propose a fine nanostructure fabrication method combining UV-NIL and silicon anisotropic wet etching that does not depend on the resolution of the imprint mold. Silicon anisotropic wet etching is widely used to fabricate three-dimensional patterns for MEMS devices on single-crystal wafers [19-22]. In anisotropic etchants, Si (111) surfaces are etched more slowly than other crystal plane surfaces [23], and thus sharp self-organized V-shaped grooves form on Si (100) wafers.

The proposed method enables fine, size-controllable nanoscale structure patterning without a finely patterned mold. A schematic of the proposed method is shown in Fig. 2.1. The wet etching mask pattern is transferred from the mold by UV-NIL. Sharp V-shaped grooves are formed by silicon anisotropic wet etching and then filled with a metal. Ar-ion milling is performed until the desired nanoscale V-shaped groove structures are obtained.

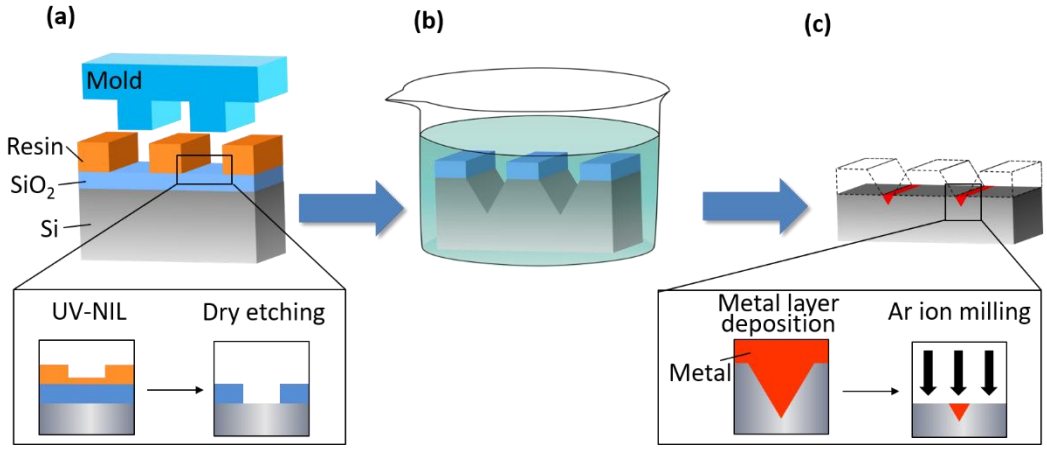

Figure 2.1 Schematic illustration of fine nanostructure fabrication by combining UV-NIL and silicon anisotropic wet etching. (a) Patterning the wet etching mask from the UV-NIL mold. (b) Sharp V-shaped groove formation by silicon anisotropic wet etching. (c) Ar-ion milling.

2.2 Experiment

Ultrafine nanoscale patterning was achieved by the following process. An n-type Si (100) substrate with 100-nm-thick layer of thermal SiO_2 was cleaned by conventional ultrasonication followed by O_2 plasma treatment (RIE-10NR, Samco Inc.). A 150-nm-thick layer of UV-curable resin (PAK-01, Toyo Gosei Co., Ltd.) was spin coated on the substrate. The imprint mold, which was coated with a fluorine release layer, had a line-and-space pattern with a linewidth of 100 nm, pitch of 200 nm, and height of 100 nm. The imprint process was performed under a pressure of 2.8 MPa with 1000 mJ/cm^2 in a vacuum of 0.2 kPa using our custom-built UV-NIL machine [24]. The resist pattern was further subjected to high-power UV light (JU-C1500, Japan Technology System Co.) after demolding to ensure complete curing and provide high etching resistance. Following residual layer etching with O_2 plasma, the resist pattern was etched into the SiO_2 layer using an inductively coupled plasma-reactive ion etching (ICP-RIE) system (RIE-100iPH, Samco Inc.). The details of the etching conditions are summarized in Table 2.1. In the etching step, a small amount of oxygen gas was added to prevent formation of a carbon-fluorine polymer layer through the reaction of the resin and C_3F_8 gas [4,25]. Finally, the remaining resin was removed by O_2 plasma etching.

Buffered hydrofluoric acid (BHF 110U, Daikin Industries, Ltd.) was used to remove the native oxide layer and the damaged layer by dry etching, and then the sharp V-shaped groove structures were formed by silicon anisotropic etching for 90 min with an SiO_2 mask. The etching solution was 25 wt% TMAH (Kanto Chemical Co. Inc.) containing 0.01 wt% non-ionic surfactant (Triton X-100, Acros Organics). The surfactant was added to improve the etching anisotropy and to decrease the surface roughness [26-28]. While anisotropic wet etching is generally performed above 60 °C [22,26-28], we conducted etching at room temperature to ensure that the etching rate was as low as possible to achieve atomic-level etching control. Subsequently, the SiO_2 mask was removed using buffered hydrofluoric acid.

A 3-nm Al_2O_3 dielectric barrier layer was deposited by ALD (SUNALE R-150, Picosan) by alternating the trimethylaluminum precursor and H_2O oxidant at 350 °C.

Next, a 30-nm metal (Al) layer was deposited by ion beam sputtering (IBS; M820, Hakuto) using an ion beam voltage of 950 V and current of 80 mA. The substrate was coated with a 750-nm-thick resin layer (SU-8, Microchem Co.) to planarize the sample surface. Finally, Ar-ion milling (IMR-3-8, Hitachi) was performed at an accelerating voltage of 400 V and ion beam current of 30 mA for 72 min. To achieve a homogeneous etching rate of the different materials, the substrate was etched at a high glancing angle [29,30].

Table 2.1 Dry etching conditions used to fabricate the SiO_2 mask.

Etching material	Gas flow (sccm)		ICP/RF power (W)	Pressure (Pa)	Time (s)
	O_2	C_3F_8			
Residual layer	5.0	0	50/20	1	60
SiO_2 layer	1.0	20	300/50	1	80

2.3 Results and discussion

3.1 Mold pattern transfer process

UV-NIL and dry etching were performed to transfer the wet etching mask pattern to SiO_2 from the mold. A cross-sectional scanning electron microscopy (SEM) image of the imprinted pattern on the UV-curable resin is shown in Fig. 2.2(a). A line-and-space pattern with a 95-nm line width and 192-nm pitch was formed without major defects. A thick residual layer was observed because of the low vacuum conditions used during the imprinting process; however, the layer was completely removed without profile changes via O_2 plasma etching (Fig. 2.2(b)). The imprinted mold pattern was etched in the SiO_2 layer (Fig. 2.2(c)) with an etching selectivity close to 1. The replicated wet etching mask pattern had a pitch of 194 nm and width of 104 nm with an error of less than 5% compared with the original mold pattern.

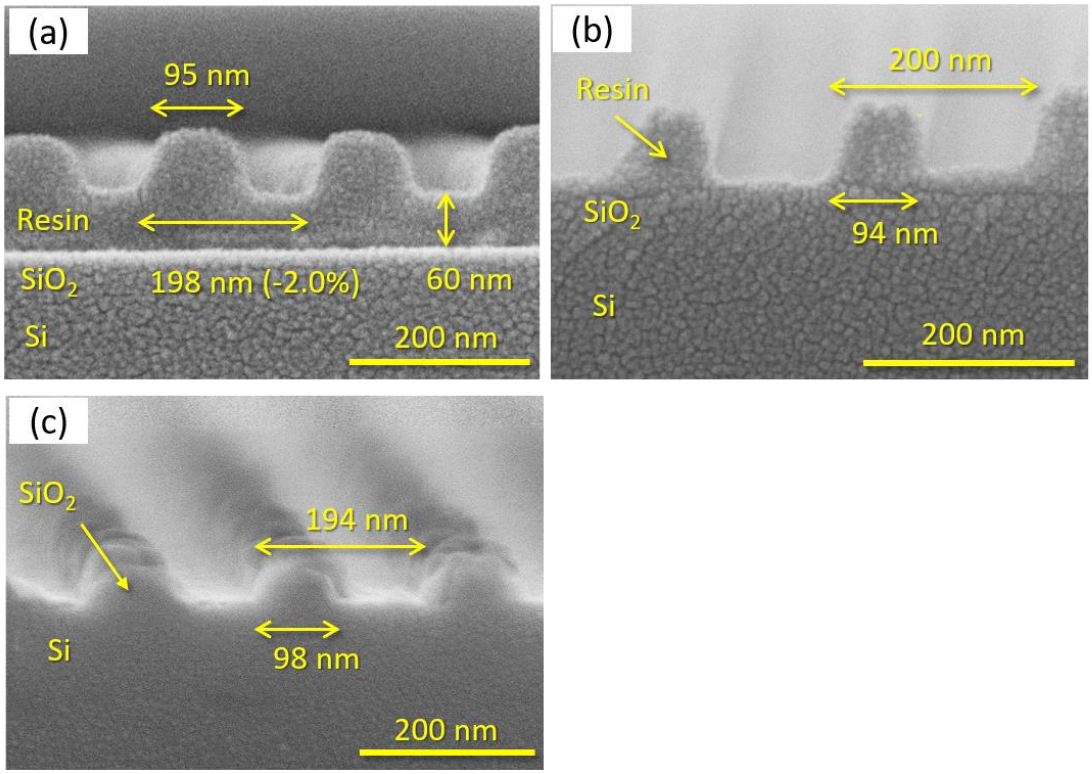

Figure 2.2 Cross-sectional SEM images of (a) imprinted pattern with a width of 100 nm on the UV-curable resin, (b) imprinted pattern after residual layer etching, and (c) mold pattern after etching of the underlying SiO_2 layer [1].

3.2 Atomically sharp V-shaped groove formation

Figure 2.3 shows the etch depth of the Si (100) surface as a function of etching time at room temperature using the TMAH etching system with a surfactant. The etching rate (R_a) was estimated from the plots to be 1.1 nm/min, which is two orders of magnitude smaller than that under conventional high-temperature conditions [26,27]. In addition, R_a agreed well with the theoretical value of 1.4 nm/min calculated by [27,31]

$$R_a = A_0 exp(-E_a/RT) \tag{2.2}$$

where A_0 is the frequency factor, E_a is the activation energy, R is the gas constant, and T is the temperature. In the calculations, we used $A_0 = 7.62 \times 10^{13}$ /s, $E_a/R = -9.07 \times 10^3$ K, and $T = 297$ K [26,27]. These results indicate that the etching

process is controlled with atomic-scale precision.

A cross-sectional SEM image of the V-shaped grooves formed by the TMAH etching system is shown in Fig. 2.4. The V-shaped grooves were fabricated using the SiO_2 mask prepared by UV-NIL. The angle of 54.6° between the surface and side wall of each V-shaped groove was close to the typical angle of 54.7° for anisotropic etching of Si (100) substrate, which formed between the Si (100) and Si (111) planes [23]. Furthermore, ultra-narrow structures with a width of 9 nm were observed in the valleys of the V-shaped grooves. Because the protruding regions of the rough side wall created by dry etching were selectively etched, the line edge roughness decreased after etching, and V-shaped grooves with smooth side walls were obtained. Our results demonstrate that slow TMAH etching at room temperature with a surfactant is useful for atomic-scale Si etching and sharp V-shaped groove formation.

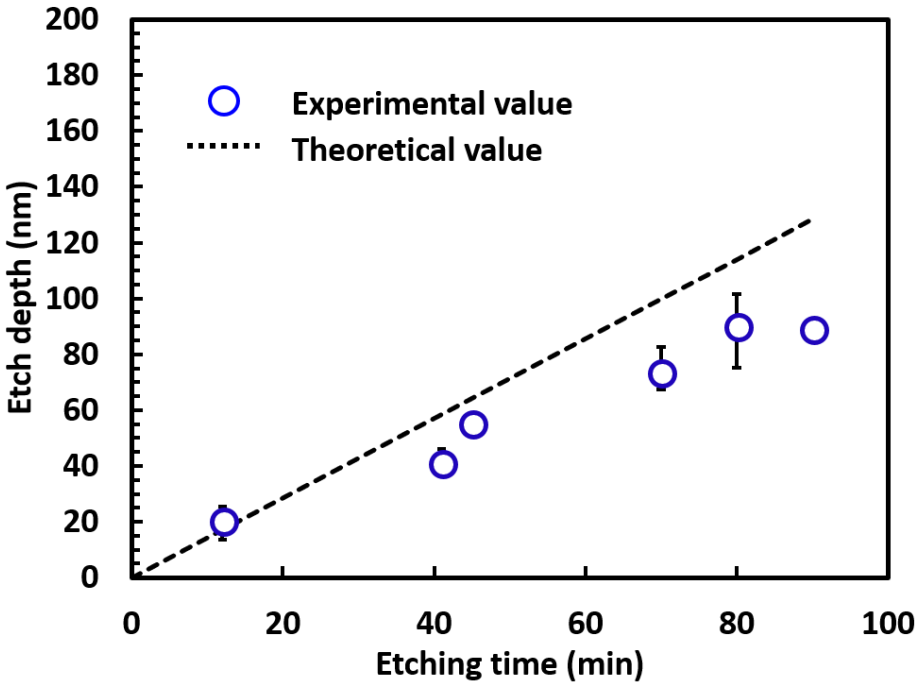

Figure 2.3 Etch depth of the Si (100) surface as a function of etch time using the room-temperature TMAH etching system with surfactant. The dashed line shows the theoretical etching rate [1].

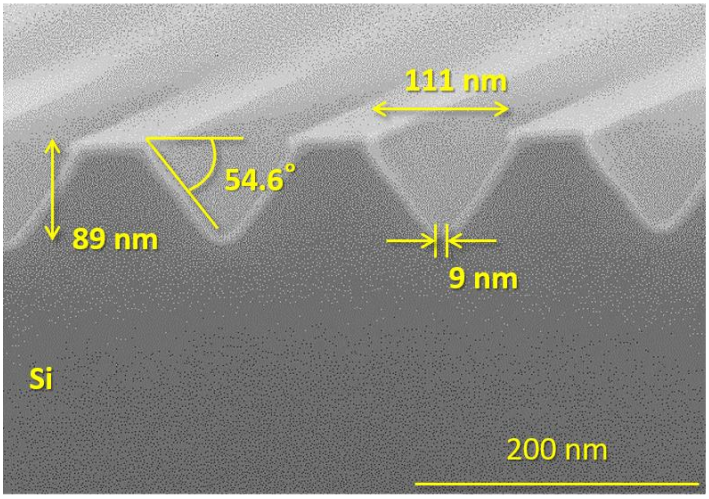

Figure 2.4 Cross-sectional SEM image of the V-shaped grooves with 9-nm ultra-narrow structures formed using the room-temperature TMAH etching system and SiO_2 mask prepared by UV-NIL [1].

3.3 Pattern minimization

Figure 2.5 shows an SEM image of the resin-coated sample after Al_2O_3 and Al deposition. The Al_2O_3/Al layers on the V-shaped groove structures are clearly visible and the patterned surface was uniformly planarized by the thick resin layer. After planarization, the patterns were etched by Ar-ion milling (Fig. 2.6). Fig. 2.6(a) and (b) show that a uniformly etched surface was obtained, indicating that a homogeneous milling rate between different materials was achieved by using a high glancing angle of 70°, as reported in previous studies [29,30]. As shown in Fig. 2.6(c), the minimum pattern was formed after 70 min of etching. The final pattern had a width of 38 nm and height of 18 nm, which indicated that fine Al patterns with reduction ratio of 62% versus the initial mold patterns were successfully produced. Based on these results, we believe that our proposed method can provide fine nanopatterns without considering the original mold quality and size, offering new possibilities for NIL processes.

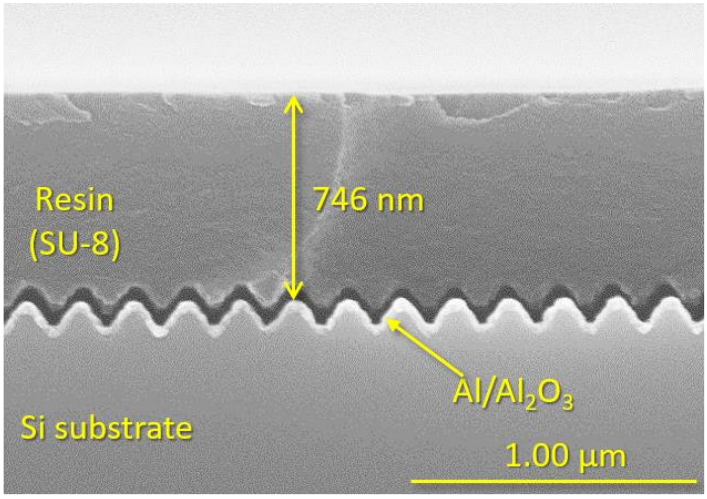

Figure 2.5 Cross-sectional SEM image of the uniformly planarized resin coated V-shaped grooves after Al_2O_3 and Al deposition [1].

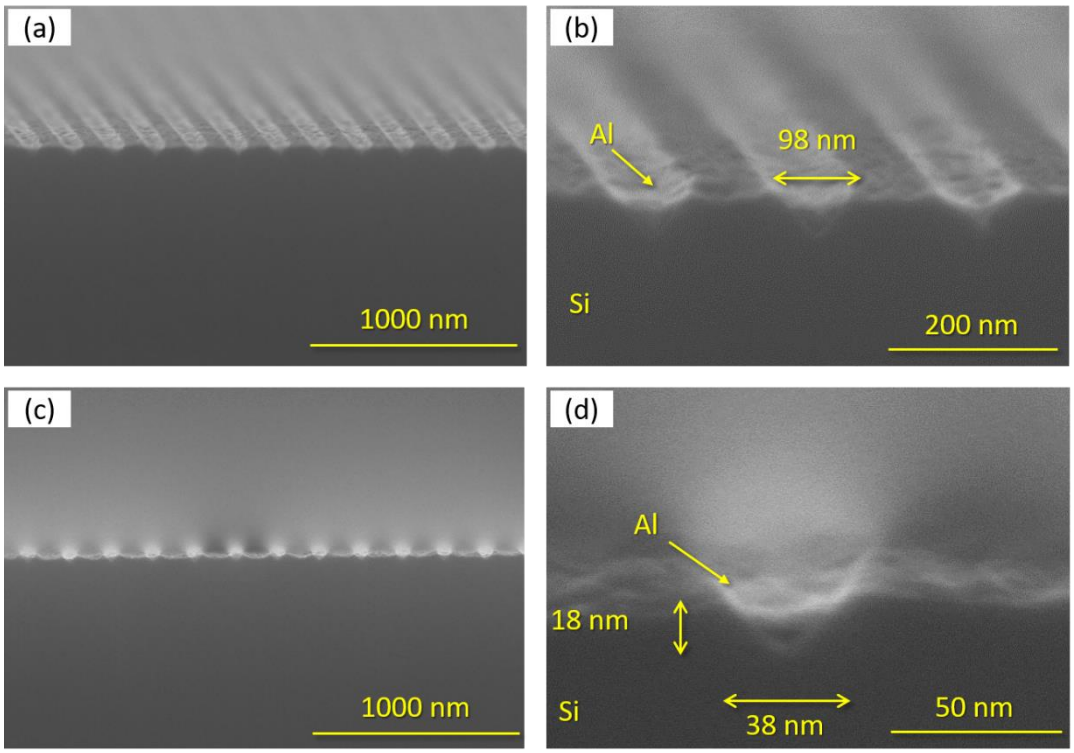

Figure 2.6 Cross-sectional SEM images of the patterns obtained after Ar-ion milling at a high glancing angle: (a) low- and (b) high-magnification images of the pattern with a width of 98 nm during the etching process; (c) low- and (d) high-magnification images of the minimized pattern with a width of 38 nm and height of 18 nm obtained by etching for 70 min [1].

3.4 Summary

We have developed a novel method to fabricate fine nanostructures by NIL and anisotropic wet etching. The fabricated metal structure consisting of the valleys of the V-shaped grooves was 62% of the initial mold size. In addition, we performed atomically controlled anisotropic wet etching at room temperature with TMAH containing a surfactant. These results show that the developed method is a promising technique for advanced NIL. The structure fabricated using this method is also applicable as a new fine nanoscale mold after removing the metal. In addition, we expect that optimization of process conditions would allow us to obtain patterns with sub-10-nm structures without a specific mold.

References

[1] H. Kuwae, A. Okada, S. Shoji and J. Mizuno, "Sub-50-nm structure patterning by combining nanoimprint lithography and anisotropic wet etching without considering original mold resolution," Microelectron. Eng., vol. 169, pp. 39-42, 2017.

[2] K. Hayashi, H. Nakanotani, M. Inoue, K. Yoshida, O. Mikhnenko, T. Nguyen and C. Adachi, "Suppression of roll-off characteristics of organic light-emitting diodes by narrowing current injection/transport area to 50 nm," Appl. Phys. Lett., vol. 106, pp. 093301, 2015.

[3] H. Kuwae, A. Nitta, K. Yoshida, T. Kasahara, T. Matsushima, M. Inoue, S. Shoji, J. Mizuno and C. Adachi, "Suppression of external quantum efficiency roll-off of nanopatterned organic-light emitting diodes at high current densities," J. Appl. Phys., vol. 118, pp. 155501, 2015.

[4] Okada, S. Shoji, H. Shinohara, H. Goto, H. Sunakawa, T. Matsueda, A. Usui, A. Yamaguchi and J. Mizuno, "Fabrication of Low Dislocation Density GaN Template by Nano-channel FIELO Using Nanoimprint Lithography," J. Photopolym. Sci. Technol., vol. 26, pp. 69-72, 2013.

[5] S. Y. Chou, P. R. Krauss and P. J. Renstrom, "Imprint of sub-25 nm vias and trenches in polymers," Appl. Phys. Lett., vol. 67, pp. 3114-3116, 1995.

[6] S. Y. Chou, and P. R. Krauss, "Imprint lithography with sub-10 nm feature size and high throughput," Microelectron. Eng., vol. 35, pp. 237-240, 1997.

[7] M. Ieong, B. Doris, J. Kedzierski, K. Rim and M. Yang, "Silicon device scaling to the sub-10-nm regime," Science, vol. 306, pp. 2057-2060, Dec 17, 2004.

[8] L. J. Guo, X. Cheng and C. Chou, "Fabrication of size-controllable nanofluidic channels by nanoimprinting and its application for DNA stretching," Nano Lett., vol. 4, pp. 69-73, 2004.

[9] S. Owa and H. Nagasaka, "Immersion lithography; its potential performance and issues," in Optical Microlithography XVI, 2003, pp. 724-734.

[10] C. Vieu, F. Carcenac, A. Pepin, Y. Chen, M. Mejias, A. Lebib, L. Manin-Ferlazzo, L. Couraud and H. Launois, "Electron beam lithography: resolution limits and

applications," Appl. Surf. Sci., vol. 164, pp. 111-117, 2000.

[11] C. Wagner and N. Harned, "EUV lithography: Lithography gets extreme," Nat. Photonics, vol. 4, pp. 24-26, 2010.

[12] C. Lim, S. Kim, Y. Hwang, J. Choi, K. Ban, S. Cho, J. Jung, E. Kang, H. Lim and H. Kim, "Positive and negative tone double patterning lithography for 50nm flash memory," in SPIE 31st International Symposium on Advanced Lithography, 2006, pp. 615410-615410-8.

[13] R. A. Segalman, "Patterning with block copolymer thin films," Mater. Sci. Eng. R Rep., vol. 48, pp. 191-226, 2005.

[14] S. Darling, "Directing the self-assembly of block copolymers," Prog. Polym. Sci., vol. 32, pp. 1152-1204, 2007.

[15] J. Haisma, M. Verheijen, K. Van Den Heuvel and J. Van Den Berg, "Mold-assisted nanolithography: A process for reliable pattern replication," J. Vac. Sci. Technol. B, vol. 14, pp. 4124-4128, 1996.

[16] M. Beck, M. Graczyk, I. Maximov, E. Sarwe, T. Ling, M. Leil, and L. Montelius, "Improving stamps for 10 nm level wafer scale nanoimprint lithography," Microelectron. Eng., vol. 61-62, pp. 441-448, 2002.

[17] C. Peroz, S. Dhuey, M. Cornet, M. Vogler, D. Olynick and S. Cabrini, "Single digit nanofabrication by step-and-repeat nanoimprint lithography," Nanotechnology, vol. 23, pp. 015305, 2011.

[18] G. Tan, N. Inoue, T. Funabasama, M. Mita, N. Okuda, J. Mori, K. Koyama, S. Kaneko, M. Nakagawa and A. Matsuda, "Formation of 0.3-nm-high stepped polymer surface by thermal nanoimprinting," Appl. Phys. Express, vol. 7, pp. 055202, 2014.

[19] J. M. Bustillo, R. T. Howe and R. S. Muller, "Surface micromachining for microelectromechanical systems," Proc IEEE, vol. 86, pp. 1552-1574, 1998.

[20] M. Hoffmann and E. Voges, "Bulk silicon micromachining for MEMS in optical communication systems," J. Micromech. Microeng., vol. 12, pp. 349, 2002.

[21] D. Burt, P. Dobson, L. Donaldson, and J. Weaver, "A simple method for high yield fabrication of sharp silicon tips," Microelectron. Eng., vol. 85, pp. 625-630,

2008.

[22] S. Migita, Y. Morita, M. Masahara and H. Ota, "Fabrication and demonstration of 3-nm-channel-length junctionless field-effect transistors on silicon-on-insulator substrates using anisotropic wet etching and lateral diffusion of dopants," Jpn. J. Appl. Phys., vol. 52, pp. 04CA01, 2013.

[23] J. Kim, U. Plachetka, C. Moormann and H. Kurz, "Fabrication of inverse micro/nano pyramid structures using soft UV-NIL and wet chemical methods for residual layer removal and Si-etching," Microelectron. Eng., vol. 110, pp. 403-407, 2013.

[24] N. Nagai, H. Ono, K. Sakuma, M. Saito, J. Mizuno and S. Shoji, "Copper multilayer interconnection using ultravaiolet nanoimprint lithography with a double-deck mold and electroplating," Jpn. J. Appl. Phys., vol. 48, pp. 115001, 2009.

[25] E. Kay, J. Coburn and A. Dilks, "Plasma chemistry of fluorocarbons as related to plasma etching and plasma polymerization," in Plasma Chemistry III, 1980, pp. 1-42.

[26] P. Pal, K. Sato, M. A. Gosalvez, Y. Kimura, K. Ishibashi, M. Niwano, H. Hida, B. Tang and S. Itoh, "Surfactant adsorption on single-crystal silicon surfaces in TMAH solution: orientation-dependent adsorption detected by in situ infrared spectroscopy," J. Microelectromech. Syst., vol. 18, pp. 1345-1356, 2009.

[27] M. Gosalvez, B. Tang, P. Pal, K. Sato, Y. Kimura and K. Ishibashi, "Orientation- and concentration-dependent surfactant adsorption on silicon in aqueous alkaline solutions: explaining the changes in the etch rate, roughness and undercutting for MEMS applications," J. Micromech. Microeng., vol. 19, pp. 125011, 2009.

[28] B. Schurink, W. Berenschot, M. Tiggelaar, and R. Luttage, "Highly uniform sieving structure by corner lithography and silicon wet etching," Microelectron. Eng., vol. 144, pp. 12-18, 2015.

[29] Stewart and M. Thompson, "Microtopography of surfaces eroded by ion-bombardment," J. Mater. Sci., vol. 4, pp. 56-60, 1969.

[30] S. Somekh, "Introduction to ion and plasma etching," J. Vac. Sci. Technol., vol. 13, pp. 1003-1007, 1976.

[31] K. J. Laidler, "The development of the Arrhenius equation," J. Chem. Educ., vol. 61, pp. 494, 1984.

Chapter 3
Durable self-cleaning glass with bridged glass nanopillars

Glass is a key component of OLED displays as well as many other optical devices. High transparency is important in such devices. In this chapter, we developed a bridged glass nanopillar structure with high scratch resistance for use as self-cleaning glass. The glass nanopillars are joined to each other with a bridge structure. The bridged glass nanopillars are fabricated using anisotropic Talbot photolithography and reactive ion etching (RIE). Atomic force microscopy (AFM) and SEM analyses showed that the bridged glass nanopillar structure was successfully fabricated by photolithography and dry etching. The scratch resistance of the bridged glass nanopillars was improved seven times as compared with that of the nanopillars without the bridge structure in friction tests using a flannel cloth. Furthermore, the bridged glass nanopillars did not collapse during high-stress friction tests using steel wool. The self-cleaning effect of the bridged glass nanopillars with superhydrophilic or -hydrophobic behavior was demonstrated by spraying water droplets on the bridged nanopillar structured surface. We expect that the proposed bridged glass nanopillars will be highly promising self-cleaning glass.

The contents of this chapter have been published in the following journal article:

"橋架け構造により高い擦り耐性を実現するガラスナノピラーの作製", 電気学会論文誌 E（センサ・マイクロマシン部門誌）, vol. 137, pp. 72-77, 2017 [1].

3.1 Introduction

Glass substrates are widely used in many applications such as OLED displays [2], smartphones [3], MEMS devices and solar cells [4,5] because of their high thermal and chemical stability and favorable optical properties [6-8]. In particular, the high optical transmittance of glass substrates is one of their most important properties when used in practical situations. To maintain the high transparency of glass substrates, there has been considerable interest in self-cleaning glass, which allows rain to wash away particulate contaminants on the glass surface without wiping [9-18]. The mechanism of self-cleaning glass is categorized into two types: a self-cleaning effect based on the superhydrophilicity of the glass surface [10,11,17,18] and that derived from superhydrophobicity of the glass surface [9,22]. Contaminants on superhydrophilic glass surfaces are flushed away by the spreading of water droplets under the contaminants. In contrast, contaminants on a superhydrophobic glass surface are carried away by rolling water droplets. There have been number of reports on self-cleaning glasses, such as glass surfaces with a TiO_2 coating [11,18] and protruding structures [9,12,15,16]. TiO_2-coated self-cleaning glass is widely known, although intense UV irradiation is required to maintain its photoinduced hydrophilicity. Meanwhile, the glass surface with protruding structures exhibits superhydrophilicity or superhydrophilicity that provides an excellent self-cleaning function without any external power. This is because the wettability of a glass surface is dramatically affected by surface topology, as indicated by the Wentzel equation [19]:

$$\cos\phi = r\cos\theta, \qquad r = \frac{actual\ surface\ area}{geometric\ surface\ area} \tag{2.1}$$

where ϕ is the apparent contact angle, r is the roughness factor, and θ is the contact angle of the ideal surface. Recently, self-cleaning glass with fine protruding structures on its surface has become a subject of growing interest [12]. In addition, periodic nanopillar structures, which act as a graded refractive index medium, can also improve optical transparency by eliminating light reflection at the surface by

the moth-eye effect [20,21].

Recent studies have reported that glass substrates with glass nanopillars, which were mainly fabricated by RIE, exhibited self-cleaning effects [15,21]. These structures show superhydrophilicity ascribed to hydrophilicity of the glass substrate itself or superhydrophobicity following hydrophobic treatment, such as self-assembled monolayer (SAM) formation [22] or fluorine coating [21,23]. Glass nanopillars show self-cleaning effects without photoirradiation because of the Wenzels effect. In addition, they have high thermal and chemical resistance resulting from the stability of glass, although the nanopillars are easily fractured when scratched because of stress concentration at the bottom angular corner of the nanopillar. Moreover, high plasma power is required to fabricate glass nanopillars by RIE. However, trench formation occurs at the edge of the nanopillars because of specular reflection of high-energy ions by the sidewall [24,25]. The trench structures further degrade the mechanical toughness of the nanopillars. Therefore, glass nanopillars with high scratch resistance are required for practical use.

In this study, we propose a glass nanopillar structure with bridges connecting nanopillars to increase mechanical durability. Each glass nanopillar is joined to adjacent nanopillars in four directions to suppress stress concentration, as shown in Fig. 3.1. Talbot lithography is used to prepare the bridged structure [25]. The mechanical properties of the bridged nanopillars are evaluated both analytically and experimentally. Additionally, the self-cleaning effect of the glass with the bridged glass nanopillar structure is also demonstrated.

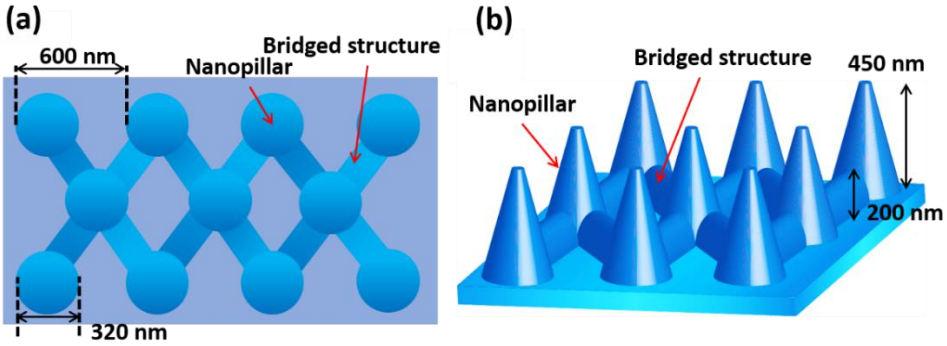

Figure 3.1 Design of the bridged glass nanopillar structure. (a) Top and (b) tilted view [1].

3.2 Experiment

3.2.1 Fabrication

Figure 3.2 illustrates the fabrication process of the bridged glass nanopillars. A fused-silica glass substrate (AGC Electronics Co., 4-inch diameter, 1-mm thick) was used as the base material. A positive photoresist (THMR-iP4300 HP, Tokyo Ohka Kogyo Co.) was spin-coated on the substrate to produce a 600-nm-thick photoresist layer.

The resist pattern of the bridged nanopillars was fabricated as a dry etching mask using anisotropic Talbot photolithography [25]. In an ordinary photolithography method, a resist layer is irradiated with parallel light from the exposure source, so a vertical pattern without bridge structures is created. Conversely, in Talbot photolithography, light scattered anisotropically using a pinhole and lens is exposed to the resist layer through a phase-shifting mask. The resulting light with an intensity distribution, which can produce bridge structures through interference. The exposed part was removed with a developing solution at room temperature. The resist pattern was designed to have a diameter of 320 nm, height of 450 nm, aspect ratio of 1.25, pitch of 600 nm, and height of the bridge structures of 200 nm.

The resist pattern was transferred to the glass substrate by ICP-RIE (RIE-101iPH, Samco Inc.,). The ICP-RIE power/bias was 500 W/100 W with a mixture of Ar and C_3F_8 gases. The flow rates of Ar and C_3F_8 were 50 and 8 sccm, respectively, to produce nanopillar sidewalls with a high taper angle (>80°) [26]. The etching conditions are summarized in Table 3.1. Finally, the remaining resin was removed by O_2 plasma etching. Glass nanopillars without bridge nanostructures were also prepared as a reference by ordinary photolithography. The mask pattern for the reference glass nanopillars was design to have a diameter of 330 nm, height of 580 nm, aspect ratio of 1.71, and pitch of 600 nm.

3.2.2 Evaluation

The resist patterns and glass nanopillars were observed using AFM

(Nanonavi L-trace, Hitachi High-Technologies Co.) and SEM (S8240, Hitachi High-Technologies Co.). The scratch resistance of the glass nanopillars was evaluated using a friction test system (TRIBOGEAR Type 38, Shintokagaku Co.) using various applied loads and scratching materials. The evaluation conditions are summarized in Table 3.2. In addition, the directional dependence of the scratch resistance was investigated. The surface condition of the scratched glass nanopillars was observed by a laser microscope (VK9500, Keyence) and SEM. The optical transparency of the glass was evaluated using an ultraviolet–visible (UV-vis) spectrophotometer (U-3900, Hitachi High-Technologies, Ltd.).

The self-cleaning effect of the glass nanopillars was evaluated using particle contaminants (Kanto Chemical Co., Inc.) in accordance with JIS Z-8901 Kanto Loam Class 7 Test Dusts (The Association of Powder Process Industry and Engineering, Japan). The particles had a density of 2.9–3.1 g/cm^2. The chemical composition of the contaminants is stated in Table 3.3. The contaminants were dispersed on the sample surface. Water droplets (50 mL) were then sprayed on the sample surface.

The self-cleaning effect of the sample after hydrophobic treatment was also evaluated. A fluorine-based solution (HD-1101Z, Harves Co, Ltd.) was used for hydrophobic SAM treatment of the glass nanopillars [22]. Before the hydrophobic SAM treatment, the surfaces of the nanopillars were treated by vacuum ultraviolet irradiation (VUV) in the presence of O_2 gas using a 172-nm Xe_2 excimer lamp (UER20-172, Ushio Inc.) [27-29]. The VUV- treated samples were immersed into the HD-1101Z solution for 1 h and then baked at 80 °C for 10 min. Finally, the surfaces were rinsed with hydrofluoroether (NOVEC7100, Sumitomo 3M Ltd.) at room temperature for 10 min to remove extra SAMs. The contact angles of the surfaces were characterized using a contact angle meter (LCD-400S, Kyowa Interface Science Co. Ltd.) with deionized water (2 μL) at room temperature.

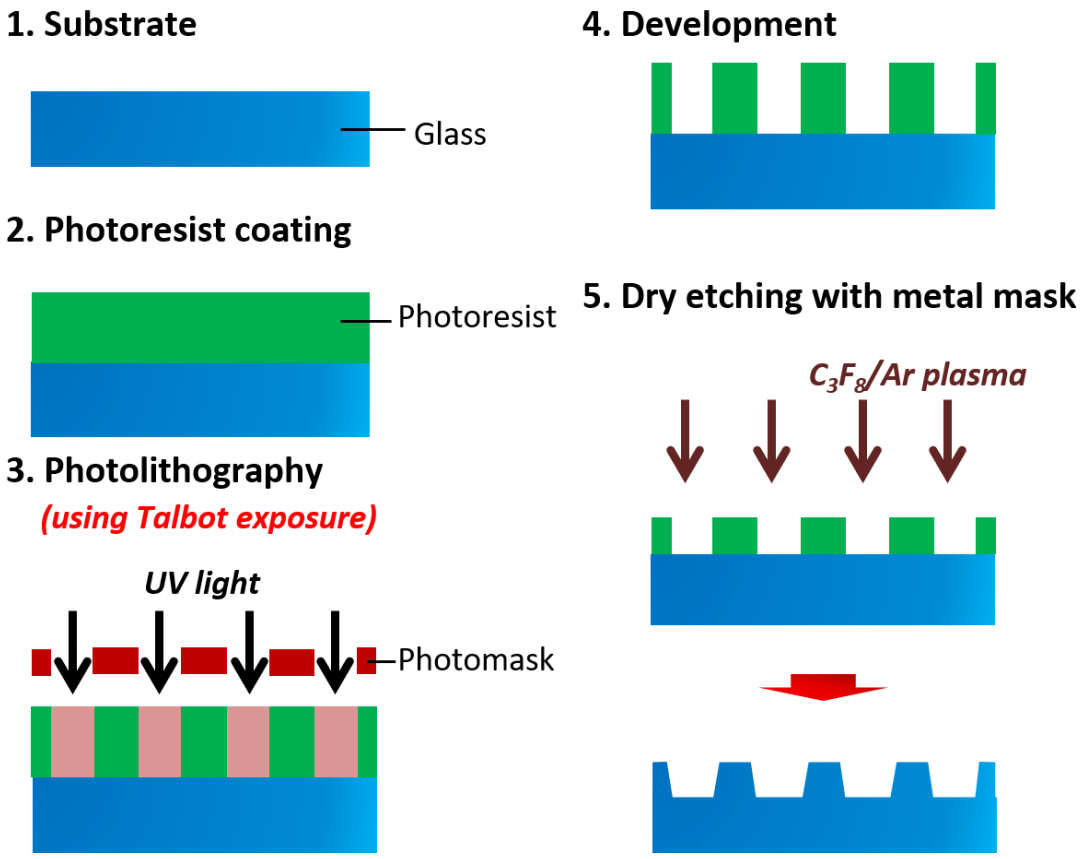

Figure 3.2 Fabrication process of the bridged glass nanopillars [1].

Table 3.1 Dry etching condition the glass nanopillars.

Gas	C_3F_8: 8 sccm	
	Ar: 50 sccm	
RF power	ICP	500 W
	BIAS	100 W
Pressure	1st	10 Pa
	2nd	10 Pa
Time	110 s	

Table 3.2 Conditions used in friction tests.

	Glass without bridged structure	Glass with bridged structure	
Test method	Flannel cloth	Flannel cloth	Steel wool
Velocity	1200 mm/min		
Range	30 mm		
Repeating Times	1000 times	1000 times	10 times
Load	100 g, 200 g, 750 g	750 g	750 g

Table 3.3 Composition of the particle contaminants used in self-cleaning tests.

Chemical compositions	Percentage by mass (%)
SiO_2	34-40
Al_2O_3	26-32
Fe_2O_3	17-23
CaO	0-3
MgO	0-7
TiO_2	0-4

3.3 Results and discussion

3.3.1 Numerical simulation using the finite element method

To verify the concept of the bridged glass nanopillar structure, the stress distribution when it was scratched were simulated using the finite element method (COMSOL Multiphysics software ver. 5.1, COMSOL AB.) with triangular elements. The bridged glass nanopillars and the reference glass nanopillars without bridged structure with and without a trench were evaluated in elastic regime. The height of the bridged glass nanopillars was changed to examine the effect of pillar height on scratch resistance. The bottom of the structure was fixed, and force was applied to

the upper left corner of the pillar horizontally. The density, Young's modulus, and Poisson ratio used in the calculations were 2203 kg/m^3, 73.1 × 10^9 Pa, and 0.17, respectively. The material data were taken from COMSOL data library. Details of the simulation conditions are summarized in Table 3.4.

Table 3.4 Design of the nanopillars used in the simulation. The curved part of the bridged structures was designed to contact a circle (radius = 100 nm). α was determined to form a smooth curve near an intersection of the circle and pillars. No. 1 and No. 3 had the same values as the fabricated glass nanopillars.

	Substrate [nm]	Trench [nm]	Bridge [nm]	Pillar [nm] (Top of substrate – top of pillar.)
No.1	400	-50	0	400
No.2	400	0	0	400
No.3	400	0	50 + α	400
No.4	400	0	50 + α	450
No.5	400	0	50 + α	500

Figure 3.3 shows the simulation results of the stress distribution in the glass nanopillars. The maximum stress of the models is summarized in Fig. 3.4. In the glass nanopillars without the bridge structure (No. 1 and No. 2), stress was strongly concentrated at the bottom angular corner of the nanopillars. Moreover, the presence of a trench led to higher maximum stress. Meanwhile, as shown in Fig. 3.3(c) (No. 3), the stress concentration at the bottom of the nanopillars was dispersed by introducing the bridge structure. The maximum stress of the bridged nanopillar was 42% lower than that of the glass nanopillar with a trench. The bridged nanopillars also showed lower maximum stress than that of the nanopillars without the bridge structure even when the height of the bridged glass nanopillars was increased (No. 4 and No. 5). These results indicate that the bridged glass nanopillar structure should suppress nanopillar collapse because the bridged structure disperses stress concentration. The prevention of trench formation achieved by including the bridge

structure should also lead to decreased stress concentration.

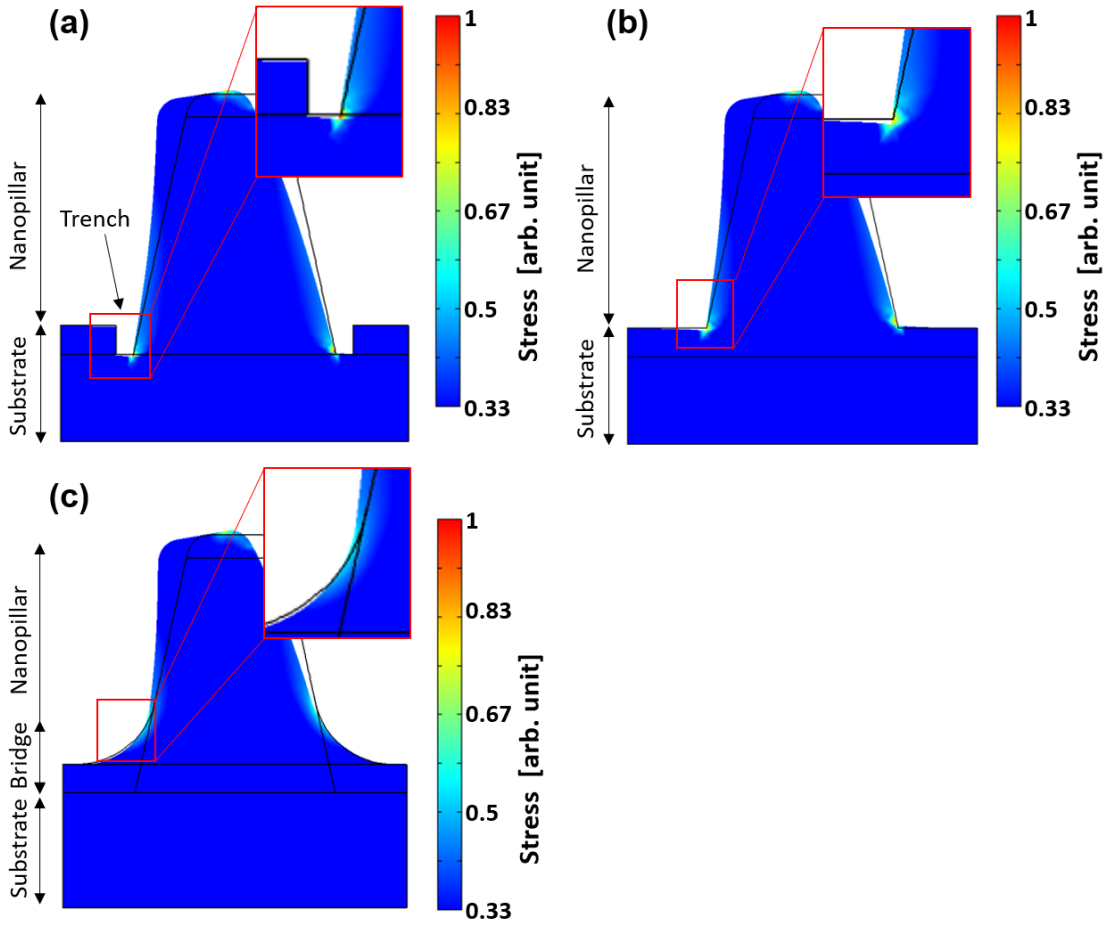

Figure 3.3 Simulation of stress distribution in (a) a glass nanopillar with a trench (No. 1), (b) a glass nanopillar without a trench (No. 2), and (c) a glass nanopillar with the bridge structure (No. 3) [1].

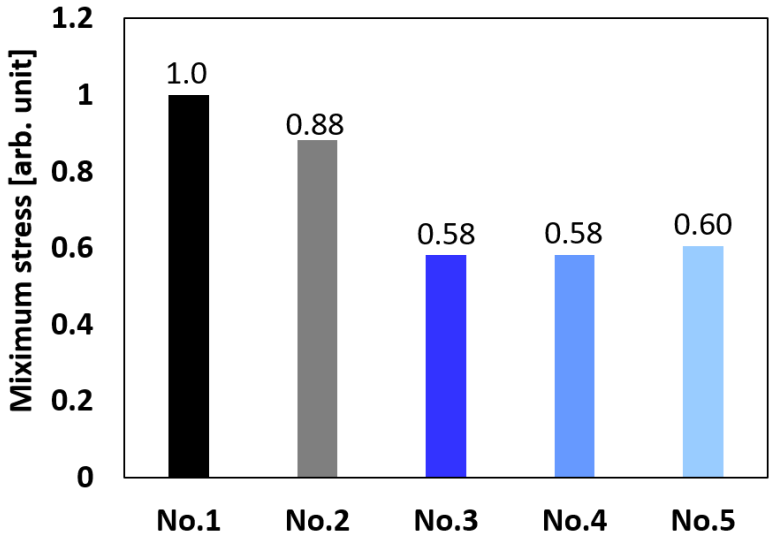

Figure 3.4 Calculated maximum stress of the simulation models.

3.3.2 Fabrication of bridged glass nanopillars

AFM and SEM images of the resist pattern obtained using conventional photolithography are shown in Fig. 3.5. The resist pattern contains independent pillars because the resist layer was exposed by parallel light through the mask. In contrast, as shown in Fig. 3.6, the resist pattern obtained using Talbot lithography possessed a bridge structure that connected the pillars with each other in four directions. This bridge structure was obtained because the light interference induced an intensity distribution of the UV light source [25]. The fabricated resist pattern without the bridged structure had a measured diameter of 328 nm, height of 681 nm, and pitch of 600 nm. The pattern with the bridge structure had a diameter of 321 nm, height of 453 nm, pitch of 600 nm, and bridge height of 189 nm.

The resist patterns were transferred to the whole surfaces of glass substrates by RIE. As shown in Fig. 3.7(a), glass nanopillars without the bridge structure were successfully formed but had a trench at the edge of edge nanopillar caused by specular reflection of ions by the sidewall [15]. Figure 3.7(b) shows that the bridge structure was inherited from the resist pattern in the bridged glass nanopillars. In addition, the bridged nanopillars did not contain obvious trenches. It is widely accepted that the gradual sidewall of the bridge structure helps to avoid

concentration of specularly reflected ions at the base of nanopillars, thereby suppressing trench formation.

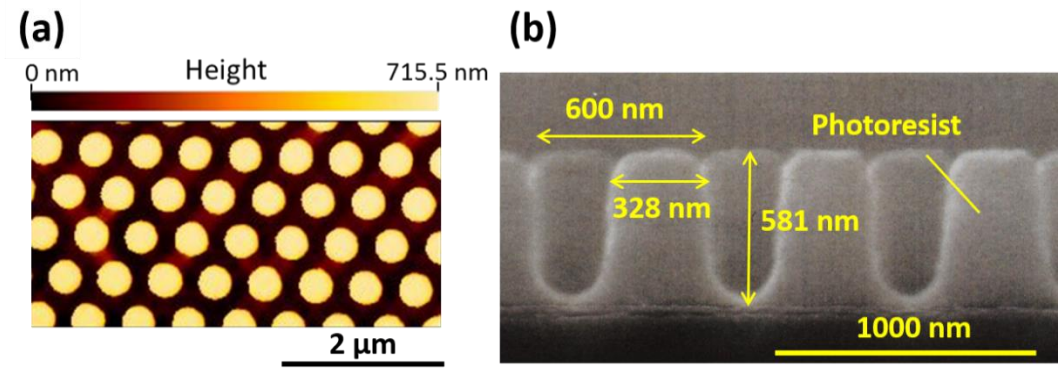

Figure 3.5 (a) AFM image and (b) cross-sectional SEM image of the photoresist nanopattern without the bridged structure [1].

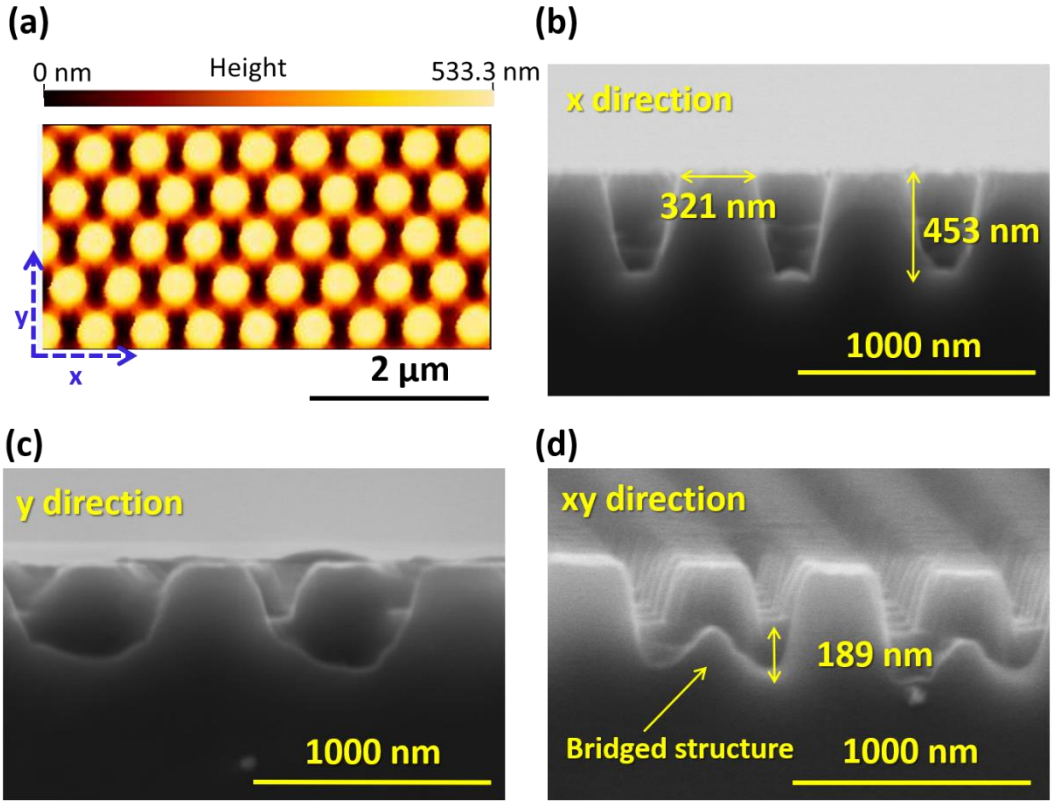

Figure 3.6 (a) AFM image and (b)–(d) cross-sectional SEM images of the photoresist nanopattern with the bridge structure [1].

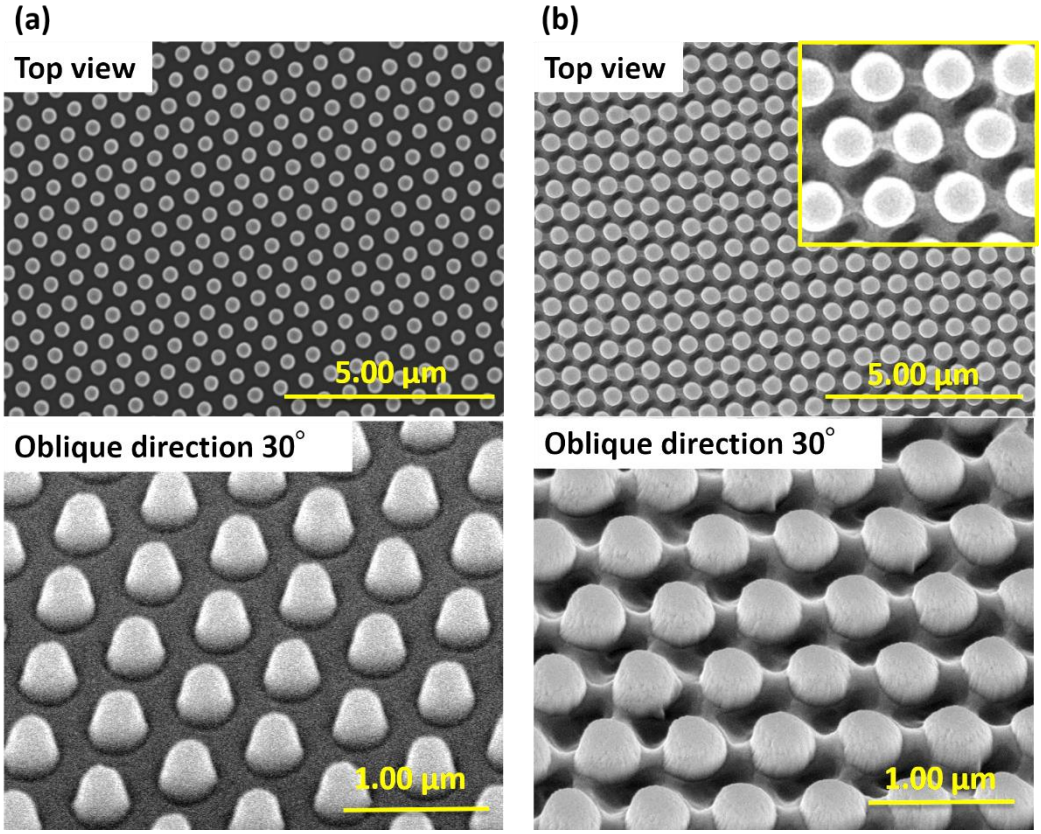

Figure 3.7 SEM images of glass nanopillars fabricated by dry etching using photoresist masks (a) without and (b) with the bridge structure [1].

3.3.3 Performance evaluation of bridged glass nanopillars

Figure 3.8 and 3.9 show results of friction tests of the glass nanopillars without and with the bridge structure, respectively. For the nanopillars without the bridge structure, scratch patterns were formed using a flannel cloth with the minimum load (100 g), as shown in Fig. 3.8(b), and the damage became progressively worse with increasing load. Figure 3.8(e) and (f) illustrate that the glass nanopillars collapsed from the edge of their bases. It is considered that this collapse behavior was caused by the stress concentration at their bases, as predicted by the simulation. In contrast, the bridged glass nanopillars did not collapse even when the highest load of 750 g was applied, which is consistent with the simulation results. The white spots in Fig. 3.9(d) are remnants of the flannel cloth used in friction testing. Moreover, as shown in Fig. 3.10, the sample was not damaged when scratched

vertically, horizontally, and diagonally on its surface. These results indicate that the scratch resistance of the bridged glass nanopillars has no directional dependence.

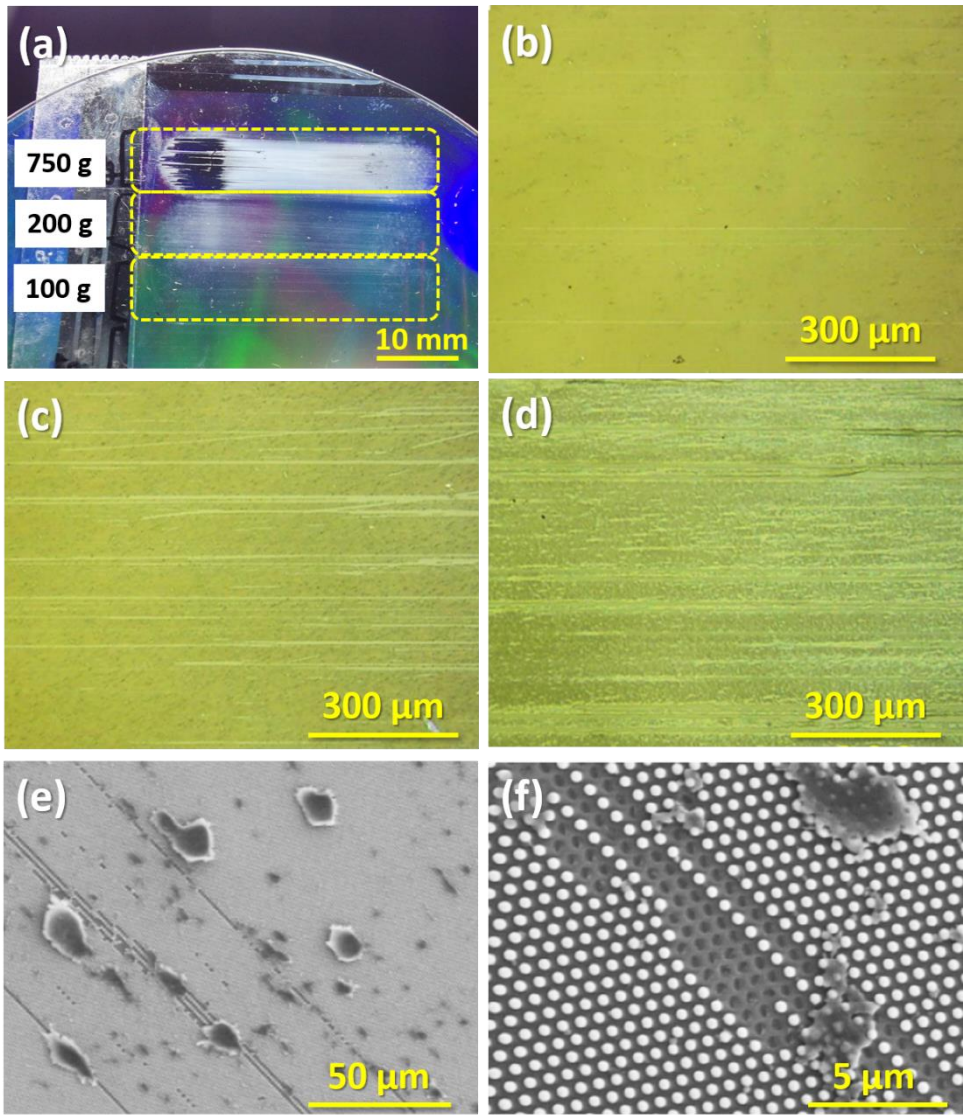

Figure 3.8 Results of friction testing of the glass nanopillars without the bridge structure. (a) Photograph of the sample surface after friction testing. Optical microscope images of surfaces tested under a load of (b) 100 g, (c) 200 g, and (d) 750 g. (e, f) SEM images of damage caused using a 750-g load [1].

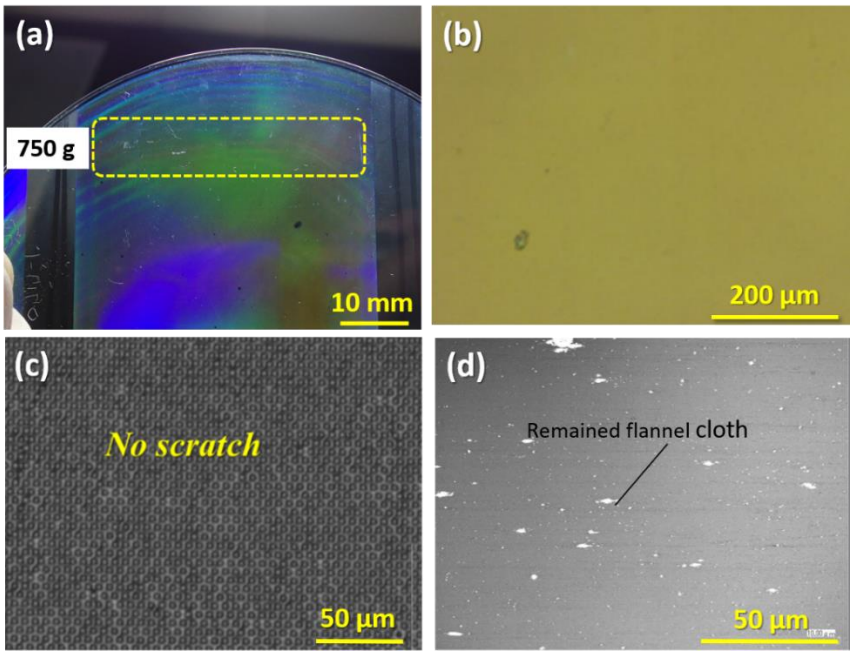

Figure 3.9 Results of friction testing of glass nanopillars with the bridge structure. (a) Photographic, (b) optical, (c) laser, and (d) SEM images of the sample surface after testing [1].

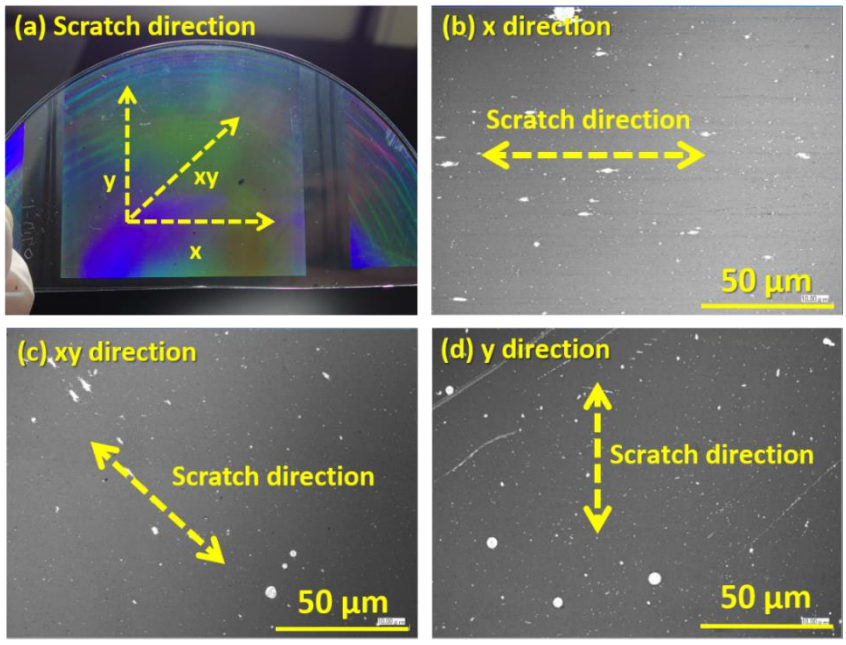

Figure 3.10 Directional dependence of the scratch resistance of the bridged glass nanopillars. (a) Photograph of the sample surface indicating scratch directions. (b–d) SEM images of the scratched surfaces. White spots are contamination from the flannel cloth used in the friction tests [1].

A high-stress friction test using steel wool was then performed on the bridged glass nanopillars under a load of 750 g. Figure 3.11 reveals that the bridged nanopillars did not break during the test; instead, the nanopillars were shaved from the top by the steel wool. This result indicates that the bridged glass nanopillars have higher scratch resistance than that of the bare glass substrate Therefore, the bridged glass nanopillars are strong enough for practical use.

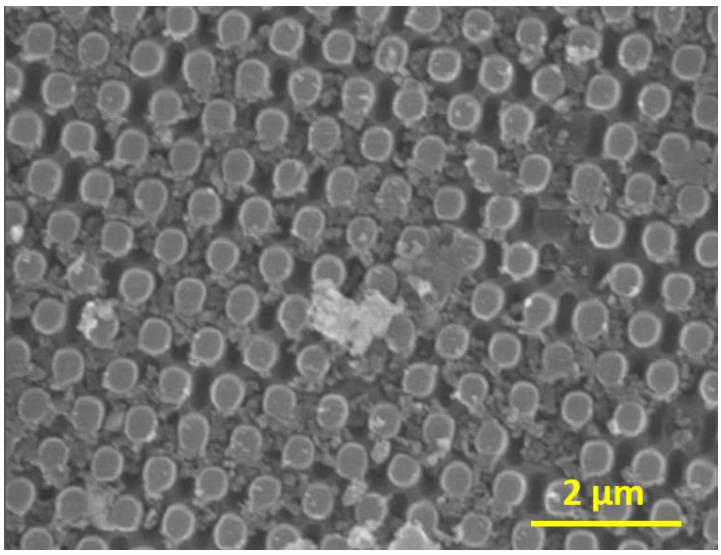

Figure 3.11 SEM image of bridged glass nanopillars after high-stress friction testing using steel wool [1].

The optical properties of the glass substrate with bridged glass nanopillars was evaluated using UV-vis spectroscopy. Figure 3.12 shows the light transmittance of the glass substrates. The characteristics in the wavelength (λ) range from= 600 to 800 nm are shown, because they decrease monotonically at shorter λ. Above λ = 750 nm, the transmittance of the glass with bridged glass nanopillars was higher than that of the bare glass. However, it decreased dramatically and was inferior to that of the bare glass below λ = 750 nm. The increase of transmittance induced by the bridged glass nanopillars at λ > 750 nm can be explained by the moth-eye effect [21,30]. This effect also predicts that the transmittance of the sample with bridged glass nanopillars should be increased up to λ = 600 nm because the pitch of the

nanopattern is 600 nm. This result agrees with the bluish appearance of the bridged glass nanopillars (Fig. 3.9(a)) Therefore, the bridged nanopillar structure needs to be further optimized from the viewpoint of optical property to maximize transmittance.

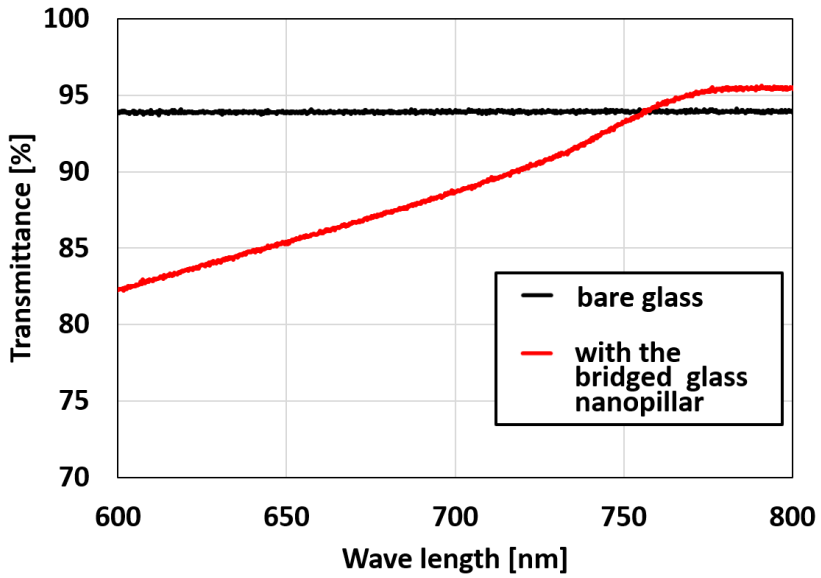

Figure 3.12 Light transmittance of glass substrates with and without bridged glass nanopillars.

3.3.4 Self-cleaning test

The wettability of samples with and without bridged glass nanopillars was determined by water contact angle measurements. Wettability is directly related to self-cleaning ability [9-11,17,18,22]. The water contact angles of glass substrates without and with the bridged glass nanopillars were 62° and less than 5°, respectively. These results indicate that the nanopillars increased the wettability of the sample to provide a superhydrophilic surface, which can be explained by the Wenzel equation (Eq. (2.1)) [18]. Water droplets could not stick to the SAM-treated glass with bridged glass nanopillars, indicating that the sample was superhydrophobic, which can also be attributed to the Wenzel effect.

Figure 3.13 shows the results of self-cleaning tests on glass substrates with and without the bridged nanopillar structure. For the bare glass substrate (Fig.

3.13(b)), contaminants remained on the surface after washing. In contrast, no marked contamination remained on the glass substrate with the bridged glass nanopillars after spraying with water droplets. This result can be explained by the wettability of the glass substrate with bridged glass nanopillars as follows: (i) when a substrate is superhydrophilic, evenly spread water passes between the substrate and contaminants, lifting the contaminants slightly from the nanopillars so that they are then flushed away [10,11,17,18], or (ii) when a substrate is superhydrophobic, contaminants are easily collected and flushed away by the action of the rolling water droplets [9,21]. From these results, we concluded that the bridged glass nanopillar structure has both high durability and self-cleaning ability.

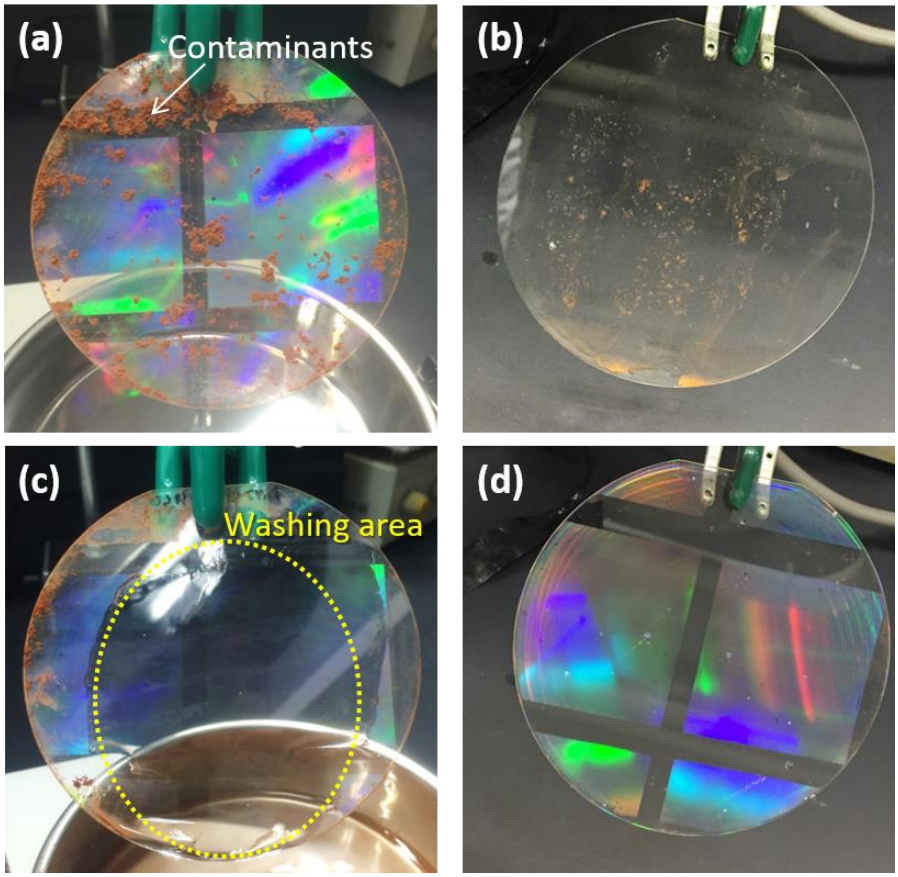

Figure 3.13 Photographs of the glass substrates in self-cleaning tests. (a) Glass substrate with the bridged nanopillar structure before washing, and after washing (b) bare glass, (c) glass substrate with the bridged nanopillar structure, and (d) hydrophobic SAM-treated glass substrate with the bridged nanopillar structure [1].

3.4 Summary

In this study, we developed a bridged glass nanopillar structure with high mechanical durability. The bridged nanopillars were fabricated by Talbot photolithography and RIE. The improved scratch resistance of the bridged nanopillars compared with that of nanopillars without bridges was confirmed by finite element analysis. Stress concentration was suppressed by introducing a bridge structure that joined adjacent pillars in four directions. The bridge structure showed not only high scratch resistance in all directions, but also higher scratch resistance than that of the bare glass substrate. In addition, the bridged nanopillars displayed self-cleaning ability. The developed bridged glass nanopillars are a highly promising technology for functionalized glass used in displays.

Reference

[1] 桑江博之, 須藤健成, 岡田愛姫子, 高山公介, 庄子習一 and 水野潤, "橋架け構造により高い擦り耐性を実現するガラスナノピラーの作製," 電気学会論文誌 E (センサ・マイクロマシン部門誌), vol. 137, pp. 72-77, 2017.

[2] C. D. Müller, A. Falcou, N. Reckefuss, M. Rojahn, V. Wiederhirn, P. Rudati, H. Frohne, O. Nuyken, H. Becker and K. Meerholz, "Multi-colour organic light-emitting displays by solution processing," Nature, vol. 421, pp. 829, 2003.

[3] D. Gallegos, K. D. Long, H. Yu, P. P. Clark, Y. Lin, S. George, P. Nath and B. T. Cunningham, "Label-free biodetection using a smartphone," Lab. Chip, vol. 13, pp. 2124-2132, 2013.

[4] C. M. Lampert, "Large-area smart glass and integrated photovoltaics," Sol. Energy Mater. Sol. Cells, vol. 76, pp. 489-499, 2003.

[5] A. Masuda, "Development of high efficiency flexible solar cells," Synthesiology English Edition, vol. 4, pp. 194-201, 2012.

[6] R. Behr, M. Karson and J. Minor, "Reliability analysis of window glass failure pressure data," Struct. Saf., vol. 11, pp. 43-58, 1991.

[7] M. Itoh, K. Inoue, K. Iwata, M. Mitsuzuka and T. Kakigano, "New highly heat-resistant polymers containing silicon: poly (silyleneethynylenephenylene ethynylene) s," Macromolecules, vol. 30, pp. 694-701, 1997.

[8] N. Yamaguchi, T. Nakamura, K. Tadanaga, A. Matsuda, T. Minami and M. Tatsumisago, "Direct Formation of Zn− Al Layered Double Hydroxide Films with High Transparency on Glass Substrate by the Sol− Gel Process with Hot Water Treatment," Cryst. Growth Des., vol. 6, pp. 1726-1729, 2006.

[9] C. Neinhuis and W. Barthlott, "Characterization and distribution of water-repellent, self-cleaning plant surfaces," Ann. Bot., vol. 79, pp. 667-677, 1997.

[10] X. Feng, L. Feng, M. Jin, J. Zhai, L. Jiang and D. Zhu, "Reversible super-hydrophobicity to super-hydrophilicity transition of aligned ZnO nanorod films," J. Am. Chem. Soc., vol. 126, pp. 62-63, 2004.

[11] K. Meilert, D. Laub and J. Kiwi, "Photocatalytic self-cleaning of modified cotton textiles by TiO2 clusters attached by chemical spacers," J. Mol. Catal. A

Chem., vol. 237, pp. 101-108, 2005.

[12] X. Zhao, Q. Zhao, J. Yu and B. Liu, "Development of multifunctional photoactive self-cleaning glasses," J. Non Cryst. Solids, vol. 354, pp. 1424-1430, 2008.

[13] A. Chabas, T. Lombardo, H. Cachier, M. H. Pertuisot, K. Oikonomou, R. Falcone, M. Verità and F. Geotti-Bianchini, "Behaviour of self-cleaning glass in urban atmosphere," Build. Environ., vol. 43, pp. 2124-2131, 2008.

[14] K. Katsumata, S. Okazaki, C. E. Cordonier, T. Shichi, T. Sasaki and A. Fujishima, "Preparation and characterization of self-cleaning glass for vehicle with niobia nanosheets," ACS Appl. Mater. Interfaces, vol. 2, pp. 1236-1241, 2010.

[15] M. Sakhuja, J. Son, H.V. Le, X. Baojuan, L.K. Verma, H.C. Zeng, H. Yang, A.J. Danner and C.S. Bhatia, "Nanopatterned and self-cleaning glass substrates for solar cell packaging," in 2nd International Conference on Control, Instrumentation and Automation (ICCIA), 2011, pp. 96-101.

[16] L. Kou and C. Gao, "Making silica nanoparticle-covered graphene oxide nanohybrids as general building blocks for large-area superhydrophilic coatings," Nanoscale, vol. 3, pp. 519-528, 2011.

[17] Y. Lai, Y. Tang, J. Gong, D. Gong, L. Chi, C. Lin and Z. Chen, "Transparent superhydrophobic/superhydrophilic TiO2-based coatings for self-cleaning and anti-fogging," J. Mater. Chem., vol. 22, pp. 7420-7426, 2012.

[18] S. Anandan, T. Narasinga Rao, M. Sathish, D. Rangappa, I. Honma and M. Miyauchi, "Superhydrophilic graphene-loaded TiO2 thin film for self-cleaning applications," ACS Appl. Mater. Interfaces, vol. 5, pp. 207-212, 2012.

[19] R. N. Wenzel, "Resistance of solid surfaces to wetting by water," Ind. Eng. Chem., vol. 28, pp. 988-994, 1936.

[20] Y. Lin, K. Su, P. Tsai, F. Chuang and Y. Yang, "Fabrication and characterization of transparent superhydrophilic/superhydrophobic silica nanoparticulate thin films," Thin Solid Films, vol. 519, pp. 5450-5455, 2011.

[21] K. Park, H. J. Choi, C. Chang, R. E. Cohen, G. H. McKinley and G. Barbastathis,

"Nanotextured silica surfaces with robust superhydrophobicity and omnidirectional broadband supertransmissivity," ACS Nano, vol. 6, pp. 3789-3799, 2012.

[22] W. Kubo and S. Fujikawa, "Au double nanopillars with nanogap for plasmonic sensor," Nano Lett., vol. 11, pp. 8-15, 2010.

[23] B. Kobrin T. Zhang, M. T. Grimes, K. Chong, M. Wanebo, J. Chinn and R. Nowak, "An improved chemical resistance and mechanical durability of hydrophobic FDTS coatings," J. Phys. Conf. Ser., vol. 34, pp. 454-457, 2006.

[24] R. J. Hoekstra, M. J. Kushner, V. Sukharev and P. Schoenborn, "Microtrenching resulting from specular reflection during chlorine etching of silicon," J. Vac. Sci. Technol. B, vol. 16, pp. 2102-2104, 1998.

[25] H. H. Solak, C. Dais and F. Clube, "Displacement Talbot lithography: a new method for high-resolution patterning of large areas," Opt. Express, vol. 19, pp. 10686-10691, 2011.

[26] T. Ujiie, T. Kikuchi, T. Ichiki and Y. Horiike, "Fabrication of quartz microcapillary electrophoresis chips using plasma etching," Jpn. J. Appl. Phys., vol. 39, pp. 3677, 2000.

[27] H. Shinohara, T. Kasahara, S. Shoji and J. Mizuno, "Studies on low-temperature direct bonding of VUV/O3-, VUV-and O2 plasma-pre-treated poly-methylmethacrylate," J. Micromech. Microeng., vol. 21, pp. 085028, 2011.

[28] T. Kasahara, S. Shoji and J. Mizuno, "Surface modification of polyethylene terephthalate (PET) by 172-nm excimer lamp," Trans. JIEP, vol. 5, pp. 47-54, 2012.

[29] A. Okada, S. Shoji, M. Nimura, A. Shigetou, K. Sakuma and J. Mizuno, "Vacuum Ultraviolet Irradiation Treatment for Reducing Gold–Gold Bonding Temperature," Mater. Trans., vol. 54, pp. 2139-2143, 2013.

[30] P. Clapham and M. Hutley, "Reduction of lens reflexion by the “Moth Eye” principle," Nature, vol. 244, pp. 281, 1973.

Chapter 4
Flexible indium tin oxide with simple micromesh patterning

Flexible transparent electrodes are important components for flexible electronic devices. In this chapter, highly bendable transparent ITO electrodes with a mesh pattern for use in flexible electronic devices are described. The mesh patterns are shown to lower tensile stress and suppress crack propagation. Simulations using the finite element method confirmed that the mesh patterns decreased tensile stress by more than 10% because the strain was shared with the flexible film when the electrodes were bent. The patterned ITO electrodes are fabricated by simple photolithography and wet etching processes. The resistance increase ratio of a mesh-patterned ITO electrode after 1000 times bending was at least two orders of magnitude lower than that of a planar ITO electrode. In addition, crack propagation was stopped by the mesh pattern of the ITO electrode. A mesh-patterned ITO electrode was used in a liquid-based OLED. The current density–voltage–luminance ($J-V-L$) curves of the OLEDS did not alter even if it was bended 100 times. These results indicate that the developed mesh-patterned ITO electrodes are useful for flexible electronic devices.

The contents of this chapter have been published in the following journal article:

"Highly flexible transparent electrodes based on mesh-patterned rigid indium tin oxide", Scientific Reports, vol. 8, pp. 2825, 2018 [1].

4.1 Introduction

Flexible electronic devices, such as OLEDs, touch panels, and organic solar cells have attracted attention because of their unique properties, for example light weight, conformability, high mechanical stability, and high formability [2]. These devices are used in novel applications, including portable and wearable devices, and they are expected to enrich people's lives. As important components of flexible electronic devices, electrodes that are flexible, transparent in the visible light range, chemically and physically stable, and display favorable electrical properties, such as appropriate work function and high conductance, are required.

Recently, extensive effort has been devoted to develop flexible transparent electrodes for use in flexible electronics; for example, Ag nanowires [3,4], Al nanowire networks [5], an Au nanosquare mesh [6], poly-(3,4-ethylenedioxythiophene):poly(styrenesulfonic acid) films [7], and carbon nanotubes [8,9]. Flexibility of these advanced electrodes was realized owning to material ductility or malleability. In conventional electrodes, nano/micro structures are used to get transparency [10-12]. Patterns, especially honeycomb structure, maintain the strength of the material while increasing flexibility [13]. However, there are few flexible transparent electrodes that fulfill all the above-mentioned requirements.

ITO has been widely used for transparent electrodes because it possesses the following advantages as compared with other transparent electrodes though it is being expensive: excellent optical transparency (>90% at 550 nm) [14], high electrical conductivity ($<1\times10^{-3}$ Ω·cm) [15], and an appropriate work function for hole injection (4.4–4.5 eV) [16,17]. Moreover, ITO shows high chemical and physical durability [18], and high workability [19]. However, conventional ITO electrodes are not suitable for use in flexible devices as ITO forms cracks easily due to its rigidity arising from its ionic bonds. Cracks in ITO lead to electrical failure of devices [20-23]. Many novel ITO-based flexible transparent electrodes have been developed to prevent ITO from cracking, including ITO nanowires [18], ITO nanoparticles [20], an ITO/CuS nanosheet network composite film [21], ITO grown by a continuous roll-to-roll sputtering process [24], and a Ag nanowire-embedded ITO film [15]. However, the

reported ITO-based flexible transparent electrodes possess complicated structures or require complex processing.

In this study, we propose highly bendable transparent ITO electrodes with simple mesh structures. The proposed electrodes are fabricated by a two-step process that involves photolithography and wet etching. Figure 4.1 shows the concept of a highly flexible ITO electrode with a mesh pattern. The mesh pattern is effective to prevent ITO from cracking by suppressing stress concentration. Furthermore, even if cracks form, the mesh pattern stops their propagation; thereby, conductivity can be maintained. Three different kinds of mesh patterns are designed to investigate the effects of pattern shape and size on electrode performance. In addition, liquid-based OLEDs with mesh-patterned ITO electrodes are fabricated to verify their utility in applications. Liquid organic semiconductors (LOSs) are used as emitters because they possess high potential for use in flexible electronic devices [25-28].

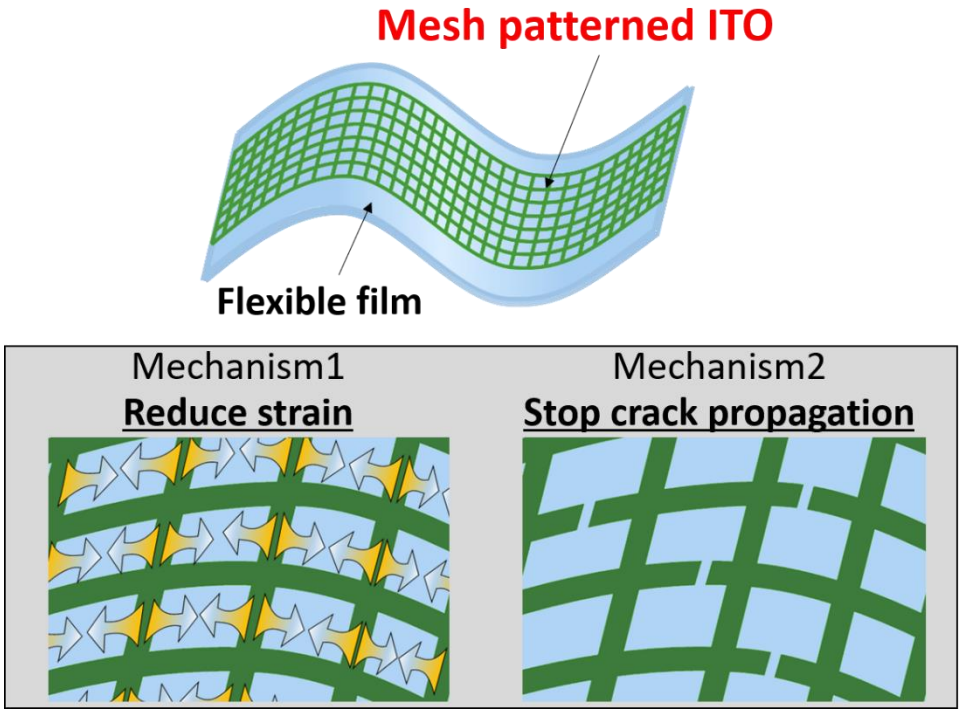

Figure 4.1 Concept of highly bendable transparent mesh-patterned ITO electrodes. The mesh pattern improves electrode flexibility by lowering tensile stress and stopping crack propagation [1].

4.2 Methods

4.2.1 Design of mesh-patterned ITO

The design of a mesh-patterned ITO electrode is shown in Fig. 4.2. An ITO layer with a thickness of 130 nm on a flexible film with a sheet resistance of 30 Ω per square (Kyoei Denshi Co., Ltd.) was used. We used 125-nm-thick polyethylene terephthalate (PET) and polyethylene naphthalate (PEN) as flexible films. A PET film was selected because it is widely used in flexible devices owing to its high optical transparency. To demonstrate the mesh-patterned ITO electrode in an OLED, a PEN film was selected to avoid heat denaturation during OLED fabrication because PEN has a high glass-transition temperature. To investigate the effects of pattern parameters on electrode performance, three kinds of characteristic patterns: square mesh, fine square mesh, and honeycomb mesh, were examined. The dimensions of the mesh patterns were smaller than the size of one pixel in common displays to obtain uniform emission [29].

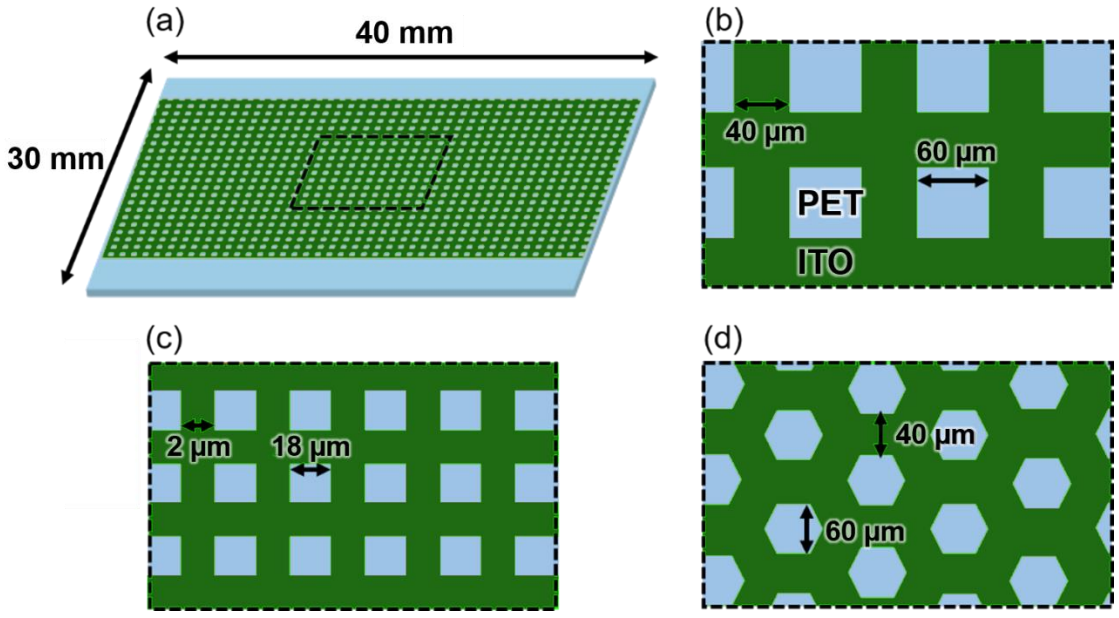

Figure 4.2 (a) Overall view of a mesh-patterned ITO electrode. Design of (b) square, (c) fine square, and (d) honeycomb mesh-patterned ITO electrodes [1].

4.2.2 Fabrication process

The mesh-patterned ITO electrodes were fabricated by a simple two-step fabrication process that involves photolithography and wet etching. First, a commercially produced ITO/PET film (Kyoei Denshi Co.) was cleaned sequentially in acetone and then isopropyl alcohol by ultrasonication for 5 min, before being rinsed with deionized water. A 7-μm-thick photoresist layer (AZ4620, AZ Electronic Materials Co.) was spin-coated on the clean ITO/PET film. Subsequently, the resist patterns used as etching masks were prepared by UV exposure (436 nm, 250 mJ/cm^2). Then, the ITO layer was etched by diluted aqua regia ($HCl : HNO_3 : H_2O = 5 : 1 : 6$), which was diluted to lower the etching rate. Finally, the mesh-patterned photoresist layer was removed with organic solutions. This process did not affect the surface properties of ITO because its surface was protected by a mask layer during patterning that was completely removed after the fabrication.

4.2.2 Evaluation

The flexibility of the mesh-patterned ITO electrodes was evaluated by cyclic bending tests, as shown in Fig. 4.3. An unpatterned ITO electrode on PET was also evaluated as a reference. The radius of curvature of the electrodes was fixed at 6.85 mm with a cylinder. The distance between contact probe pads was kept at 30 mm. Each electrode was bent 1000 times along its long side. Changes of resistance were measured using a digital resistance meter (DT-117, Hozan Tool Industrial Co. Ltd.). The surfaces of the ITO electrodes before and after cyclic bending tests were evaluated by SEM (Hitachi High-Technologies Co., SU-8240 and S-4800). To clearly reveal defects, SEM images of the mesh-patterned ITO electrodes were obtained in a bent state. Moreover, the optical properties of the mesh-patterned ITO electrodes were evaluated using a UV-vis spectrophotometer (U-3900, Hitachi High-Technologies, Ltd.).

To evaluate the performance of the mesh-patterned ITO electrodes in devices, liquid-based OLEDs with planar or mesh-patterned ITO electrodes were fabricated. LOSs, which were first reported in 2009 [30], are liquids at room temperature. Thus,

LOSs prevent detachment or peeling of the emitting layer from electrodes in liquid OLEDs [31]. However, liquid OLEDs with LOSs have showed low efficiency to date, even though LOSs are expected to allow realization of truly flexible devices [25]. Design and energy diagrams of the liquid OLEDs are presented in Fig. 4.4. The OLEDs were fabricated using a heterogeneous bonding technique in accordance with our previous work [25-28]. An LOS as an emitting layer was sandwiched between ITO electrodes with a 6-μm-thick negative-type photoresist spacer (SU-8, MicroChem Corp.). Square mesh-patterned ITO was used as a cathode. An epoxy-terminated SAM (3-glycidodyloxypropyltriethoxysilane; GOPTS) and an amine-terminated SAM (3-aminopropyltriethoxysilane; APTES) were prepared on the ITO anode and cathode, respectively, to increase their bonding strength [32]. In addition, APTES lowers the work function of ITO, which improves electron injection from ITO to the lowest unoccupied molecular orbital (LUMO) of the LOS [28]. The LOS 1-pyrenebutyric acid 2-ethylhexyl ester (PLQ; Nissan Chemical Industries, Ltd.) was selected as the liquid emitting layer. PLQ exhibits EL emission through recombination of holes and electrons injected from the SAM-modified electrodes. The area of the emitting layer was 2 mm^2. Mesh-patterned ITO electrodes before and after bending 100 times were used as cathodes in the liquid OLEDs. $J-V-L$ characteristics of the devices were measured under DC operation by a source meter (2400, Keithley) and photodetector (1936-R, Newport).

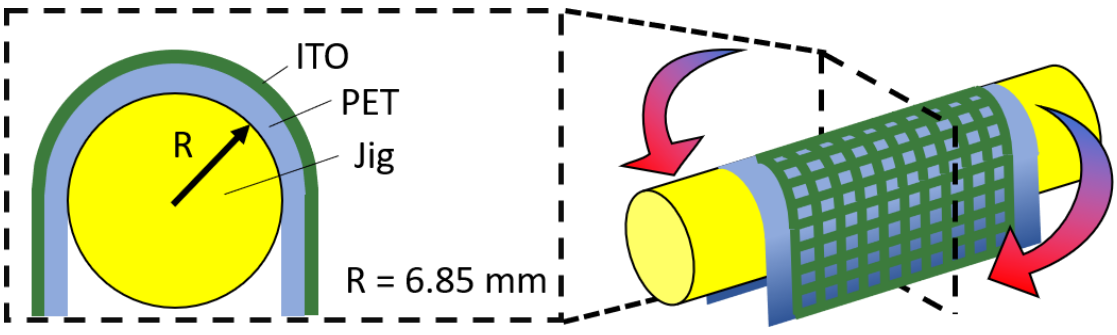

Figure 4.3 Experimental setup used to evaluate the flexibility of mesh-patterned ITO electrodes. The radius of curvature of the electrode was fixed to 6.85 mm with a cylinder [1].

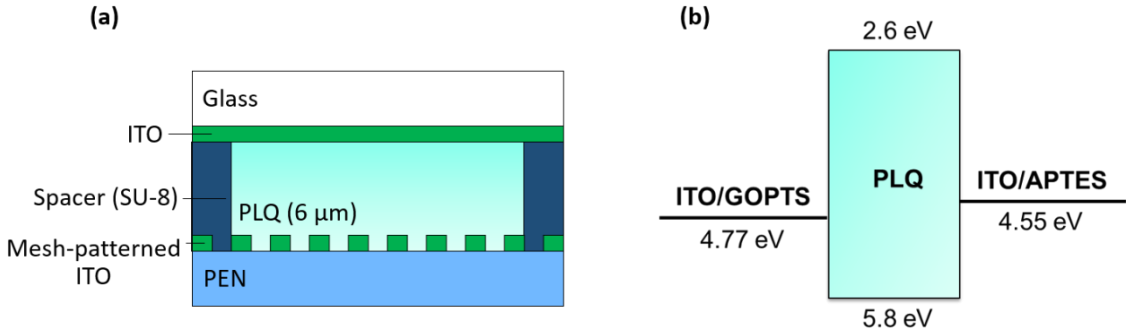

Figure 4.4 (a) Device structure and (b) energy diagram of a liquid OLED using a mesh-patterned ITO electrode.

4.3 Results and discussion

4.3.1 Numerical simulation using the finite element method

To verify the concept of the flexible mesh-patterned ITO electrodes, the tensile stress and strain on them in the bent state were simulated using the finite element method (COMSOL Multiphysics software ver. 5.1, COMSOL AB). An unpatterned ITO electrode and ones with square, fine square, and honeycomb mesh patterns were evaluated in elastic regime. In the models, the thickness of the PET film was decreased to 2 μm to perform the calculations with finite elements of sufficiently small size. The short side of the PET film was fixed, and the opposite side was moved through displacement to bend the film with a constant radius of curvature. The detailed calculation parameters and material properties are summarized in Fig. 4.5 and Table 4.1, respectively. The radius of curvature used in the calculations was 7 μm to reflect the thickness of the PET film model.

Table 4.1 Material parameters used in the simulation. The parameters are cited from a previous report [33].

	Young's modulus (GPa)	Poisson's ration
ITO	1.18×10^2	0.30
PET	2.9	0.37

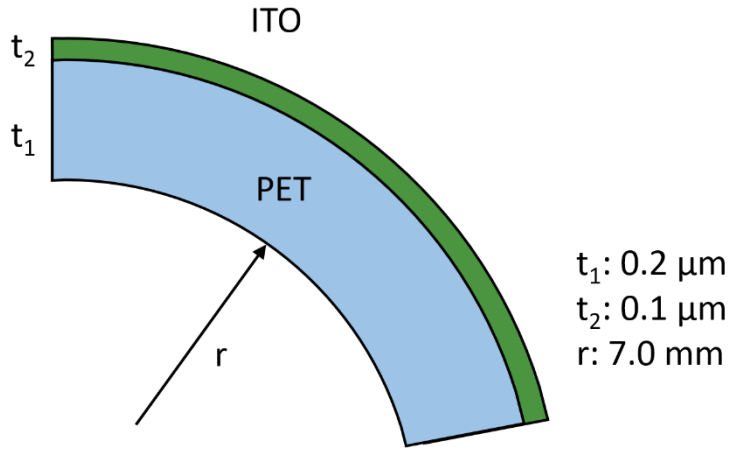

Figure 4.5 Schematic diagram of the simulation model [1].

Figure 4.6(a) shows the calculated tensile stress of ITO in the vicinity of the ITO/PET interface. The tensile stress decreased considerably along the short side of the model. The average in-plane tensile stress, which was the mean value of the center area of each model to avoid the influence from the edges, of the models is summarized in Table 4.3. The average tensile stress on ITO near the ITO/PET interface was lowered by more than 10% by introducing the mesh patterns. The fine square mesh pattern exhibited lower stress than the other patterns; thus, the finer pattern displayed higher flexibility than the coarser ones. The strain of the PET film is illustrated in Figure 4.6(b). These results indicate that the strain escaped from ITO to the flexible substrate along the mesh pattern. The strain can escape to the flexible film in the models with mesh-patterned ITO because they have ITO-free areas. In contrast, planar ITO does not have ITO-free areas, so the strain remains in ITO. Thus, it is predicted that the mesh pattern can suppress crack formation in ITO because of its lower tensile stress than that of a solid ITO film. The stress of the honeycomb pattern was slightly higher than those of the other patterns. It is believed that the honeycomb structure does not allow stress to readily escape because of its high mechanical strength [13].

In conventional flexible electrodes, flexibility has been realized by enhancing material properties; in addition, nano/microstructures have been used to obtain transparency [10-12]. As a result, it is difficult to realize flexible electrodes

from rigid materials using the conventional concept. Our concept is different from the conventional concept based on material properties. The above results indicate that our concept is useful to develop novel flexible electrodes based on rigid materials including metal oxides.

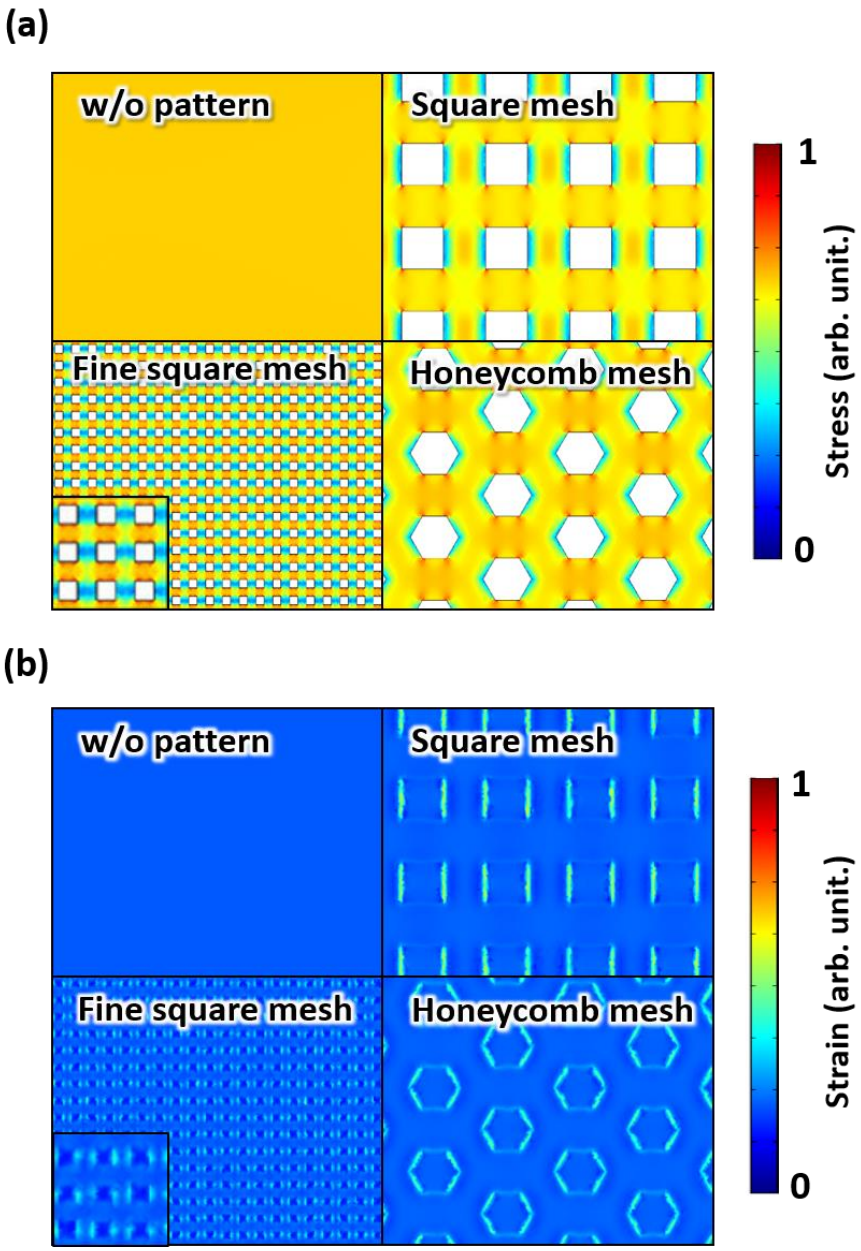

Figure 4.6 Simulation results. (a) Stress in ITO in the vicinity of the ITO/PET interface. (b) Strain in PET near the ITO/PET interface. Inset: Enlarged image of the result for the fine square mesh-patterned ITO electrode [1].

Table 4.2 Average relative tensile stress of the center area of the planar ITO electrode and square, fine square, and honeycomb mesh-patterned ITO electrodes.

	Tensile stress (a.u.)
Planar	1.00
Square	8.66×10^{-1}
Finer square	8.01×10^{-1}
Honeycomb	8.89×10^{-1}

4.3.2 Performance evaluation of mesh-patterned ITO electrodes

Optical microscope images of the fabricated mesh-patterned ITO electrodes are shown in Fig. 4.7(a)-(c). The etching rate of diluted aqua regia was 6 nm/s. The mesh patterns were successfully fabricated via the simple two-step fabrication process with an error of 10% or less as compared with the design parameters. The edges of the mesh patterns were rounded in the etching process. This is desirable because rounded corners help to avoid stress concentration at the edges of the pattern [34,35].

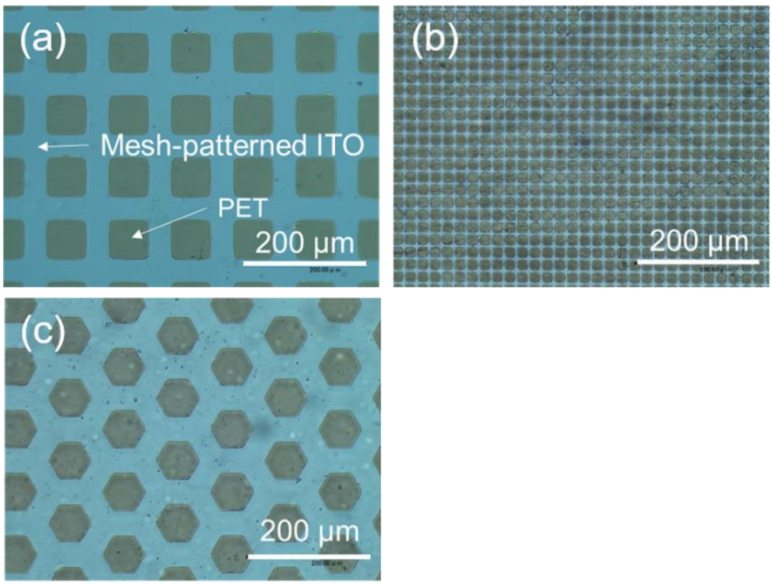

Figure 4.7 Optical microscope images of (a) square, (b) fine square, and (c) honeycomb mesh-patterned ITO electrodes [1].

Figure 4.8 shows the increase of the resistance ratio (R_n/R_0) versus the number of bending times of the unpatterned (planar) and patterned ITO electrodes during cyclic bending tests, where R_0 and R_n are the initial resistance and that after bending n times, respectively. The R_n/R_0 values of various other mesh patterns are also presented in the Fig. 4.8. The resistances and increase ratio (R_{1000}/R_0) before and after 1000 times bending are summarized in Table 4.3. R_0 of the planar ITO electrode was 55.7 Ω. R_n increased by approximately 1700 times after 1000 cycles ($R_{1000} = 9.14 \times 10^4$ Ω). In contrast, R_0 of the mesh-patterned ITO electrodes was slightly higher than that of the planar ITO electrode because of the patterning. R_n/R_0 values of the ITO electrodes with square, fine square, and honeycomb mesh patterns after bending 1000 times were 1.83, 1.05, and 14.7, respectively, which were lower than that of the planar ITO electrode by at least two orders of magnitude (Table 4.3). It is considered that these results were caused by the lower tensile stress of the patterned ITO compared with that of planar ITO, as predicted by the simulation (Section 4.3.1). Comparing the shapes of the mesh patterns, the fine square mesh showed the lowest increase of R_n/R_0 and the honeycomb mesh exhibited the highest. This tendency also agreed well with the simulation results for tensile stress and the in-plane average tensile stress values for the different patterns.

Table 4.3 Electrical resistance of ITO electrodes with and without mesh patterns before and after bending 1000 times and their resistance increase ratios.

	Resistance before bending (Ω)	Resistance after 1000 times bending (Ω)	Increase rate
Planar	5.57×10^1	9.41×10^4	1.69×10^3
Square	1.71×10^2	3.14×10^2	1.83
Fine square	1.51×10^2	1.59×10^2	1.05
Honeycomb	1.02×10^2	1.50×10^3	1.47×10^1

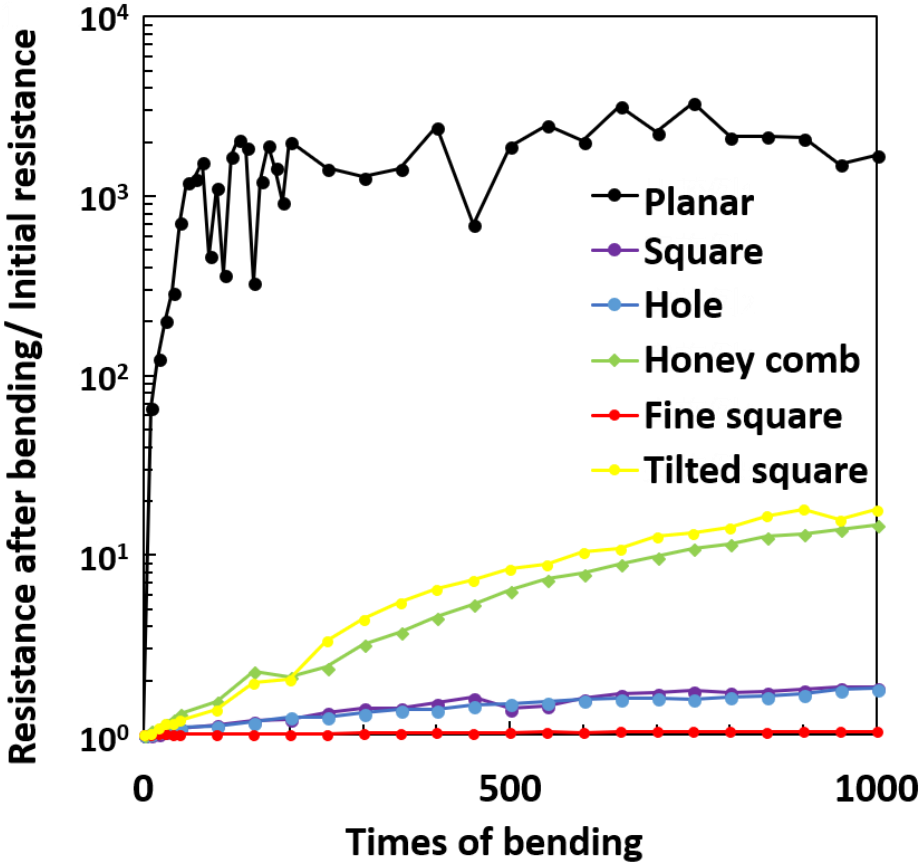

Figure 4.8 Change of electrical resistance versus the number of bending cycles for a planar ITO electrode and ones with various mesh patterns [1].

SEM images of the ITO electrode surfaces are presented in Fig. 4.9. Obvious cracks formed in the planar electrode after the bending test (Fig. 4.9(a) and (b)). The planar ITO electrode cracked easily during cyclic bending because of its rigidity. In contrast, only a few cracks were observed in the mesh-patterned ITO electrodes (Fig. 4.9(c)-(f)). Thus, cracking was suppressed in the mesh-patterned ITO electrodes, which is accounted for by the simulation results. In addition, crack propagation was stopped by the patterns. This effect supports the low increase of R_n/R_0 of the mesh-patterned ITO electrodes during bending testing. Therefore, it is confirmed that the flexibility of the mesh-patterned ITO electrode was obtained by suppression of the stress and hindered crack propagation.

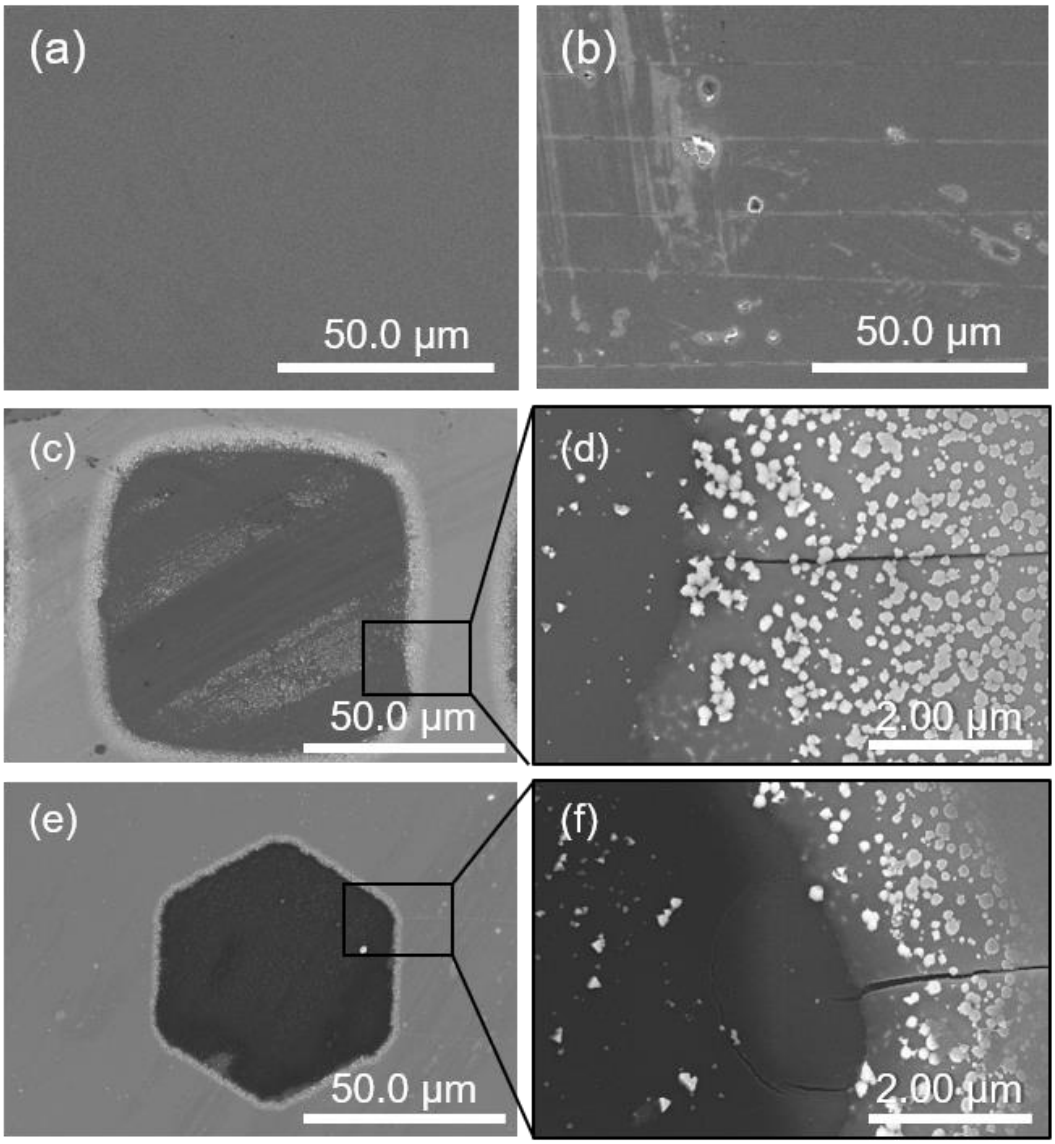

Figure 4.9 SEM images of the mesh-patterned ITO electrodes. Planar ITO surface (a) before and (b) after bending 1000 times. Surface of the square mesh-patterned ITO electrode after bending 1000 times at (c) low and (d) high magnification. Surface of the honeycomb mesh-patterned ITO electrode at (e) low and (f) high magnification. The light spots present on ITO are considered to be ITO particles that adhered to the electrodes during the etching process [1].

The optical properties of the mesh-patterned ITO electrodes were evaluated using UV-vis spectroscopy. Figure 4.10 shows the light transmittance of the planar and mesh-patterned ITO electrodes before and after bending. The different transmittance of the planar and mesh-patterned ITO electrodes is thought to be

caused by the areas without ITO in the patterned electrodes. The square and honeycomb meshes showed slightly higher transmittance than that of the fine square mesh. Moreover, it was confirmed that the transmittance of the square mesh pattern decreased after bending, whereas that of the other patterns was not markedly affected by bending. Optimization of the mesh pattern from an optical perspective will be required in the future.

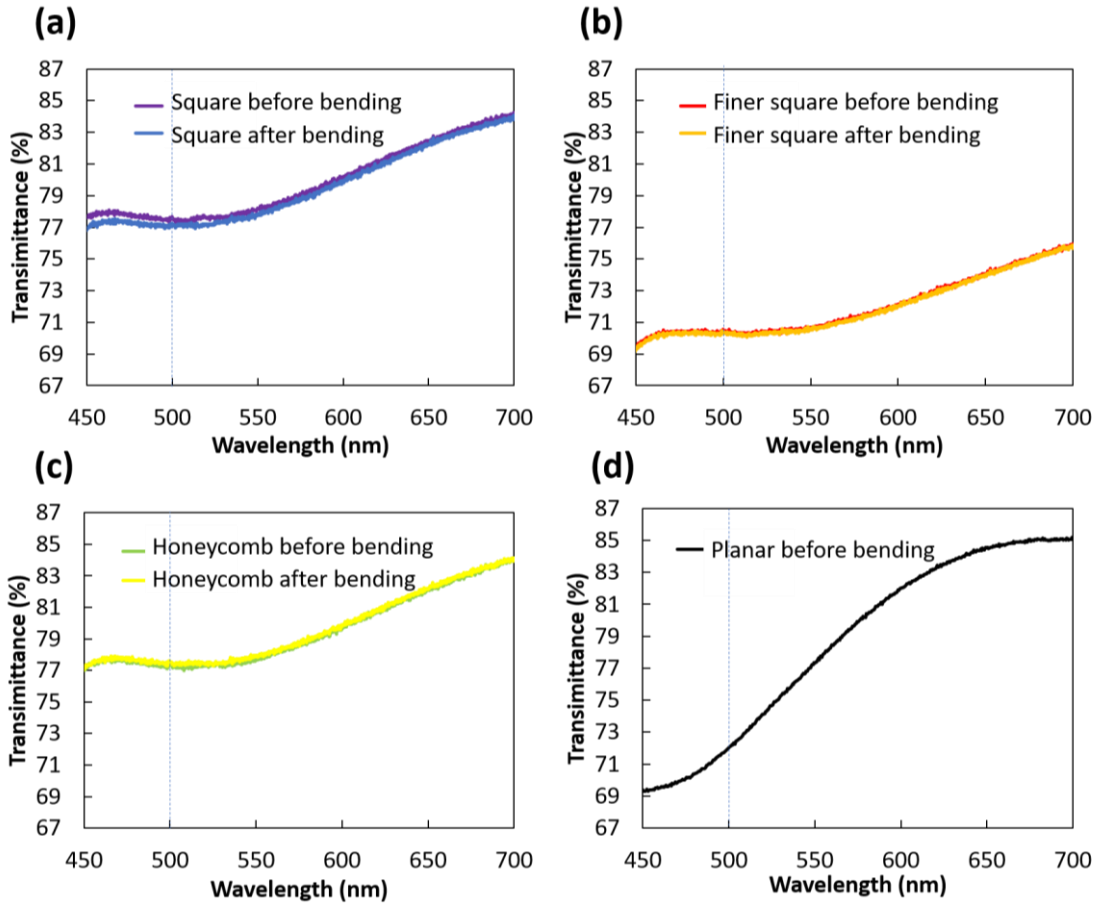

Figure 4.10 Transmittance of (a) square, (b) fine square, and (c) honeycomb mesh-patterned and (d) planar ITO electrodes. The peak wavelength of EL emission of PLQ is indicated by a blue dashed line in each spectrum [1].

4.3.3 Evaluation of liquid-based OLEDs with mesh-patterned ITO electrodes

Square mesh-patterned ITO electrodes on PEN films before and after bending 100 times were used in OLEDs. PEN has similar mechanical properties to those of PET, so the mesh-patterned ITO electrode on a PEN film should display the

same characteristics as those of the electrode on a PET film. Planar ITO electrodes before and after bending 100 times were also used in OLEDs as references.

The $J-V-L$ characteristics of the OLEDs are shown in Fig. 4.11. The experiment was repeated two or three times; the same results were obtained, indicating sufficient reproducibility. Figure 4.12 presents representative data for the OLEDs. J and L were calculated by dividing the measured values by the active device area (2 mm^2). The $J-V-L$ characteristics of the OLEDs with the planar and mesh-patterned ITO electrodes before bending were similar. That is, J was proportional to V^2; namely, the OLEDs showed space-charge-limited current behavior [31,16]. This indicates that stable carrier injection was achieved from the mesh-patterned ITO electrode. The OLED with a mesh-patterned ITO electrode before bending exhibited lower J and L values compared to those of the OLED with a planar ITO electrode before bending. This is because the actual areas of the electrodes were different; thus, the calculated values were shifted according to the electrode area.

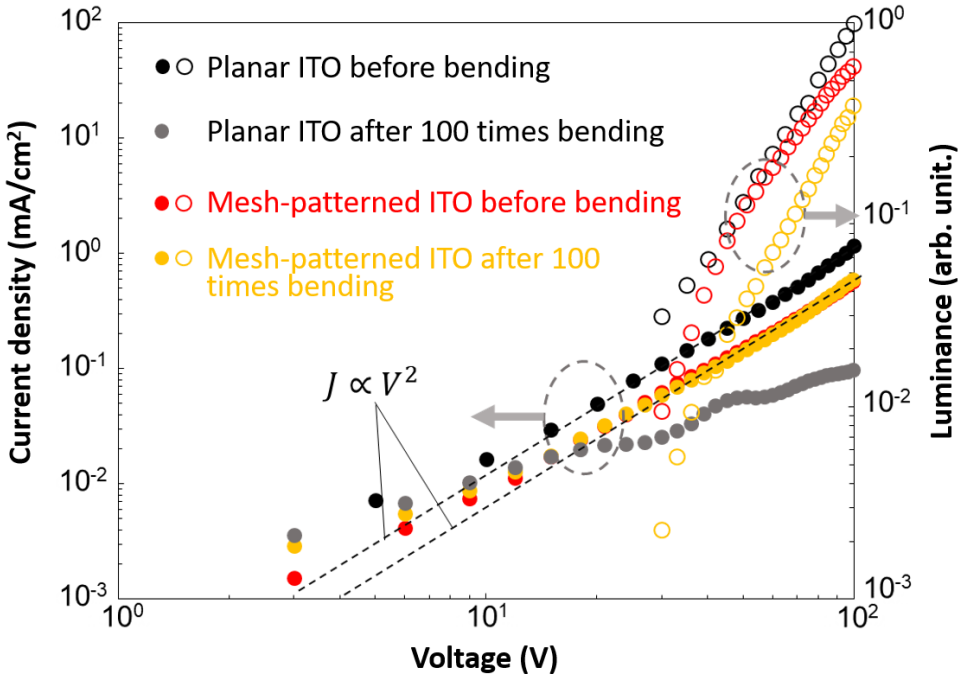

Figure 4.11 J-V (closed dot) and L-V (open dot) characteristics of liquid-based OLEDs with planar or mesh-patterned ITO electrodes before or after bending 100 times. The device containing a planar ITO electrode after bending 100 times did not work [1].

The OLED with the planar ITO electrode after 100 bending times showed low J values and did not emit light. In contrast, the OLED with the mesh-patterned ITO electrode after bending 100 times displayed the same $J-V$ curve as those of the planar and mesh-patterned ITO electrodes before bending. These results indicate the stable performance of the mesh-patterned ITO electrode in a flexible device. The same $L-V$ curve was obtained for the OLEDs with mesh-patterned ITO electrodes before and after bending, whereas the $L-V$ curve shifted downwards for the device with the mesh-patterned ITO electrode after bending 100 times. It is considered that a decrease of transmittance caused by small cracks forming in the square mesh-patterned ITO electrode during bending was one of the reasons for the shift of L, as shown in Fig. 4.10. In addition, because the refractive indices of PEN, ITO, and PLQ are 1.7 [37], 1.9 [38], and 1.6, respectively, total reflection could occur in the damaged electrode depending on the incident angle of the crack. In contrast, total reflection did not occur in the undamaged ITO electrodes. Therefore, it is inferred that propagated light was trapped in the ITO layer by the cracks formed during repeated bending cycles.

Figure 4.12 shows the EL curves of the OLEDs with mesh-patterned ITO electrodes before and after bending 100 times under 70-V DC operation. Uniform EL emission was obtained from both OLEDs, indicating that the pattern size was fine enough not to affect the emission. In addition, cyclic bending did not have an obvious effect on the EL behavior of the device. It is considered that there is no limitation of the flexibility of mesh-patterned ITO from the viewpoint of electrical conductivity of the device, because J did not change much after bending 100 times and the resistance of the mesh-patterned ITO did not increase after bending 100 times. However, consideration from both electrical and optical perspectives will be required to further improve the performance of flexible devices.

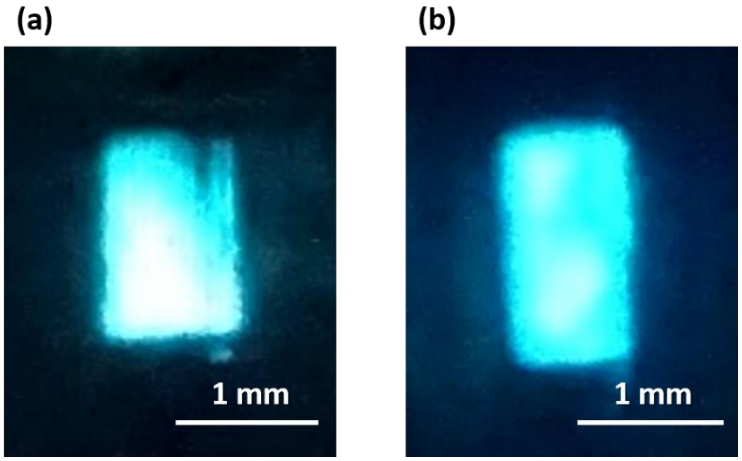

Figure 4.12 Electroluminescence from liquid-based OLEDs containing mesh-patterned ITO electrodes (a) before and (b) after bending 100 times. The operating voltage was 70 V [1].

4.4 Summary

We developed a highly bendable transparent ITO electrode structure based on simple mesh patterns. Mesh-patterned ITO electrodes were successfully fabricated via a simple two-step process involving photolithography and wet etching. Simulation results implied that the mesh patterns lowered the tensile stress of ITO. The increases of R_n/R_0 after bending 1000 times for the square, fine square, and honeycomb mesh-patterned ITO electrodes were smaller than that of the planar ITO electrode by at least two orders of magnitude. SEM images verified that the mesh-patterned ITO electrodes showed excellent flexibility compared with that of the planar ITO electrode by suppressing crack propagation. This effect is not the same as that of conventional concepts to obtain flexible devices, which are based on malleability or ductility of materials. Our results indicated that mesh patterning will be a useful approach to increase the flexibility of metal oxides regardless of their rigidity. In addition, the *J-V-L* characteristics of an OLED containing a mesh-patterned ITO electrode after bending 100 times were the same as those of an OLED with a planar ITO electrode before bending. Moreover, the OLED with a mesh-patterned ITO electrode after bending 100 times exhibited uniform EL emission.

Finally, we compared previously reported flexible ITO electrodes and our mesh-patterned ITO electrode, as shown in Fig. 4.13. The developed mesh-patterned ITO is not the most flexible type of ITO produced to date, although it realizes top-level flexibility using a simple structure and fabrication process, unlike the other electrodes. Overall, the developed mesh-patterned ITO electrodes are attractive for use in future practical flexible electronic devices.

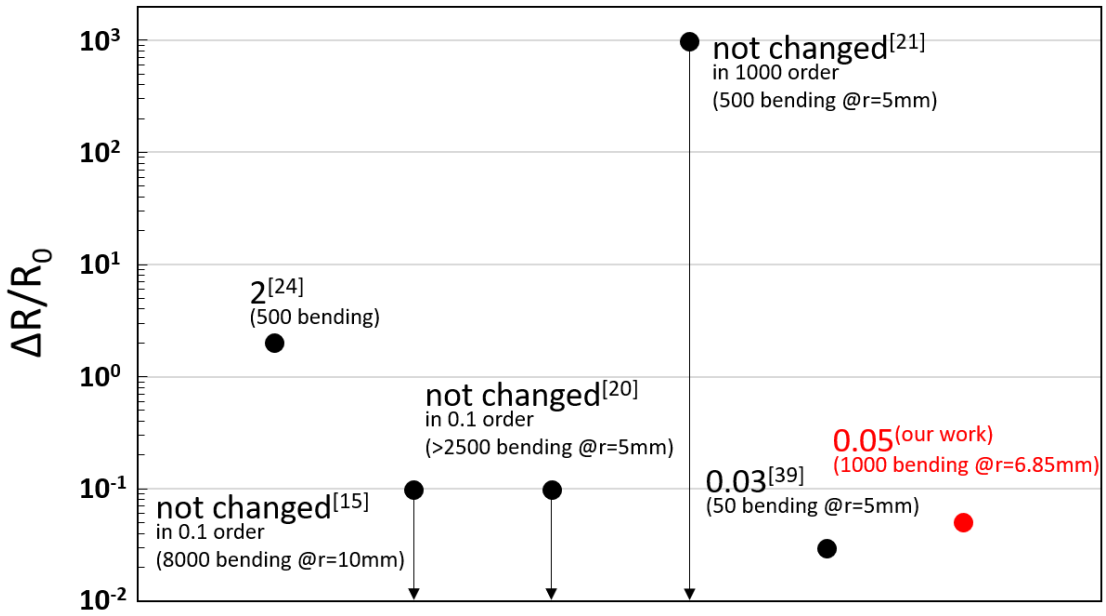

Figure 4.13 Performance comparison of reported flexible ITO electrodes and the developed mesh-patterned ITO electrode. Some previous reports stated that the resistance did "not change, although the measured minimum range differs between papers. Therefore, if the previous report stated “not changed”, we show the resistance change here as the measured minimum range.

References

[1] K. Sakamoto, H. Kuwae, N. Kobayashi, A. Nobori, S. Shoji and J. Mizuno, "Highly flexible transparent electrodes based on mesh-patterned rigid indium tin oxide," Sci. Rep., vol. 8, pp. 2825, 2018.

[2] V. Zardetto, T. M. Brown, A. Reale and A. Di Carlo, "Substrates for flexible electronics: A practical investigation on the electrical, film flexibility, optical, temperature, and solvent resistance properties," J. Polym. Sci. B Polym. Phys., vol. 49, pp. 638-648, 2011.

[3] S. M. Bergin, Y. Chen, A. R. Rathmell, P. Charbonneau, Z. Li and B. J. Wiley, "The effect of nanowire length and diameter on the properties of transparent, conducting nanowire films," Nanoscale, vol. 4, pp. 1996-2004, 2012.

[4] D. Wang, W. Zhou, H. Liu, Y. Ma and H. Zhang, "Performance improvement in flexible polymer solar cells based on modified silver nanowire electrode," Nanotechnology, vol. 27, pp. 335203, 2016.

[5] K. Azuma, K. Sakajiri, H. Matsumoto, S. Kang, J. Watanabe and M. Tokita, "Facile fabrication of transparent and conductive nanowire networks by wet chemical etching with an electrospun nanofiber mask template," Mater Lett, vol. 115, pp. 187-189, 2014.

[6] G. Yang, B. Liu, K. Cheng and Z. Du, "Modulation of optical transmittance and conductivity by the period, linewidth and height of Au square mesh electrodes," Opt. Express, vol. 23, pp. A62-A70, 2015.

[7] M. Vosgueritchian, D. J. Lipomi and Z. Bao, "Highly conductive and transparent PEDOT: PSS films with a fluorosurfactant for stretchable and flexible transparent electrodes," Adv. Funct. Mater., vol. 22, pp. 421-428, 2012.

[8] Z. Wu, Z. Chen, X. Du, J. M. Logan, J. Sippel, M. Nikolou, K. Kamaras, J. R. Reynolds, D. B. Tanner, A. F. Hebard and A. G. Rinzler, "Transparent, conductive carbon nanotube films," Science, vol. 305, pp. 1273-1276, 2004.

[9] D. S. Hecht, L. Hu and G. Irvin, "Emerging transparent electrodes based on thin films of carbon nanotubes, graphene, and metallic nanostructures," Adv. Mater., vol. 23, pp. 1482-1513, 2011.

[10] J. Zou, H. Yip, S. K. Hau and A. K. Jen, "Metal grid/conducting polymer hybrid transparent electrode for inverted polymer solar cells," Appl. Phys. Lett., vol. 96, pp. 96, 2010.

[11] J. Van De Groep, P. Spinelli and A. Polman, "Transparent conducting silver nanowire networks," Nano Lett., vol. 12, pp. 3138-3144, 2012.

[12] J. W. Lim, Y. T. Lee, R. Pandey, T. Yoo, B. Sang, B. Ju, D. K. Hwang and W. K. Choi, "Effect of geometric lattice design on optical/electrical properties of transparent silver grid for organic solar cells," Opt. Express, vol. 22, pp. 26891-26899, 2014.

[13] M. Yamashita and M. Gotoh, "Impact behavior of honeycomb structures with various cell specifications—numerical simulation and experiment," Int. J. Impact Eng., vol. 32, pp. 618-630, 2005.

[14] H. Lin and W. Hsu, "Electrode patterning of ITO thin films by high repetition rate fiber laser," Appl. Surf. Sci., vol. 308, pp. 58-62, 2014.

[15] K. Choi, J. Kim, Y. Noh, S. Na and H. Kim, "Ag nanowire-embedded ITO films as a near-infrared transparent and flexible anode for flexible organic solar cells," Sol. Energy Mater. Sol. Cells, vol. 110, pp. 147-153, 2013.

[16] Y. Park, V. Choong, Y. Gao, B. R. Hsieh and C. W. Tang, "Work function of indium tin oxide transparent conductor measured by photoelectron spectroscopy," Appl. Phys. Lett., vol. 68, pp. 2699-2701, 1996.

[17] J. Kim, M. Granström, R. Friend, N. Johansson, W. Salaneck, R. Daik, W. Feast and F. Cacialli, "Indium–tin oxide treatments for single-and double-layer polymeric light-emitting diodes: The relation between the anode physical, chemical, and morphological properties and the device performance," J. Appl. Phys., vol. 84, pp. 6859-6870, 1998.

[18] E. N. Dattoli and W. Lu, "ITO nanowires and nanoparticles for transparent films," MRS Bull, vol. 36, pp. 782-788, 2011.

[19] R. G. Gordon, "Criteria for choosing transparent conductors," MRS Bull, vol. 25, pp. 52-57, 2000.

[20] J. Yun, Y. H. Park, T. Bae, S. Lee and G. Lee, "Fabrication of a completely

transparent and highly flexible ITO nanoparticle electrode at room temperature," ACS Appl. Mater. Interfaces, vol. 5, pp. 164-172, 2012.

[21] X. Zhang, X. Liu, Y. Zhang, R. Bao, D. Peng, T. Li, G. Gao, W. Guo and C. Pan, "Rational design of an ITO/CuS nanosheet network composite film as a counter electrode for flexible dye sensitized solar cells," J. Mater. Chem. C, vol. 4, pp. 8130-8134, 2016.

[22] D. R. Cairns, R. P. Witte, D. K. Sparacin, S. M. Sachsman, D. C. Paine, G. P. Crawford and R. Newton, "Strain-dependent electrical resistance of tin-doped indium oxide on polymer substrates," Appl. Phys. Lett., vol. 76, pp. 1425-1427, 2000.

[23] S. K. Park, J. I. Han, D. G. Moon and W. K. Kim, "Mechanical stability of externally deformed indium–tin–oxide films on polymer substrates," Jpn. J. Appl. Phys., vol. 42, pp. 623, 2003.

[24] K. Choi, J. Jeong, J. Kang, D. Kim, J. K. Kim, S. Na, D. Kim, S. Kim and H. Kim, "Characteristics of flexible indium tin oxide electrode grown by continuous roll-to-roll sputtering process for flexible organic solar cells," Sol. Energy Mater. Sol. Cells, vol. 93, pp. 1248-1255, 2009.

[25] T. Kasahara, S. Matsunami, T. Edura, J. Oshima, C. Adachi, S. Shoji and J. Mizuno, "Fabrication and performance evaluation of microfluidic organic light emitting diode," Sens. Actuators. A Phys., vol. 195, pp. 219-223, 2013.

[26] M. Tsuwaki, T. Kasahara, T. Edura, S. Matsunami, J. Oshima, S. Shoji, C. Adachi and J. Mizuno, "Fabrication and characterization of large-area flexible microfluidic organic light-emitting diode with liquid organic semiconductor," Sens. Actuators. A Phys., vol. 216, pp. 231-236, 2014.

[27] N. Kobayashi, T. Kasahara, T. Edura, J. Oshima, R. Ishimatsu, M. Tsuwaki, T. Imato, S. Shoji and J. Mizuno, "Microfluidic white organic light-emitting diode based on integrated patterns of greenish-blue and yellow solvent-free liquid emitters," Sci. Rep., vol. 5, pp. 14822, 2015.

[28] T. Kasahara, S. Matsunami, T. Edura, R. Ishimatsu, J. Oshima, M. Tsuwaki, T. Imato, S. Shoji, C. Adachi and J. Mizuno, "Multi-color microfluidic organic

light-emitting diodes based on on-demand emitting layers of pyrene-based liquid organic semiconductors with fluorescent guest dopants," Sens. Actuators B Chem., vol. 207, pp. 481-489, 2015.

[29] H. Yang, H. Lin and H. Tsao, "The Method of 2/3 Sampled Sub-Pixel Rendering for AMOLED Display," Journal of Display Technology, vol. 12, pp. 158-164, 2016.

[30] D. Xu and C. Adachi, "Organic light-emitting diode with liquid emitting layer," Appl. Phys. Lett., vol. 95, pp. 207, 2009.

[31] S. Hirata, H. J. Heo, Y. Shibano, O. Hirata, M. Yahiro and C. Adachi, "Improved device lifetime of organic light emitting diodes with an electrochemically stable π-conjugated liquid host in the liquid emitting layer," Jpn. J. Appl. Phys., vol. 51, pp. 041604, 2012.

[32] L. Tang and N. Y. Lee, "A facile route for irreversible bonding of plastic-PDMS hybrid microdevices at room temperature," Lab. Chip, vol. 10, pp. 1274-1280, 2010.

[33] C. Lee, Y. Shih, C. Wu, C. Tsai, S. Yeh, Y. Peng and K. Chen, "Development of robust flexible OLED encapsulations using simulated estimations and experimental validations," J. Phys. D, vol. 45, pp. 275102, 2012.

[34] M. Isida, "On the tension of an infinite strip containing a square hole with rounded corners," Bulletin of JSME, vol. 3, pp. 254-259, 1960.

[35] J. P. Benthem, "Stresses in the region of rounded corners," Int. J. Solids Structures, vol. 23, pp. 239-252, 1987.

[36] P. Mark and W. Helfrich, "Space - charge - limited currents in organic crystals," J. Appl. Phys., vol. 33, pp. 205-215, 1962.

[37] H. Nakamura, Y. Shirakawa, H. Kitamura, T. Yamada, Z. Shidara, T. Yokozuka, P. Nguyen, T. Takahashi and S. Takahashi, "Blended polyethylene terephthalate and polyethylene naphthalate polymers for scintillation base substrates," Radiat. Measur., vol. 59, pp. 172-175, 2013.

[38] T. A. Kӧnig, P. A. Ledin, J. Kerszulis, M. A. Mahmoud, M. A. El-Sayed, J. R. Reynolds and V. V. Tsukruk, "Electrically tunable plasmonic behavior of

nanocube–polymer nanomaterials induced by a redox-active electrochromic polymer," ACS Nano, vol. 8, pp. 6182-6192, 2014.

[39] Q. Dong, Y. Hara, K. T. Vrouwenvelder, K. T. Shin, J. A. Compiano, M. Saif and R. Lopez, "Superflexibility of ITO Electrodes via Submicron Patterning," ACS Appl. Mater. Interfaces, vol. 10, pp. 10339-10346, 2018.

Chapter 5
Suppression of external quantum efficiency roll-off in nanopatterned organic light-emitting diodes

We developed OLEDs with nanopatterned current flow regions using EB lithography with the aim of suppressing SPA. Nanopatterns composed of lines and circles were used in the current flow regions of nano-line and nano-dot OLEDs, respectively. Excitons partially escape from the current flow regions where SPA occurs. As such, the current densities at which EQEs were half of their initial values (J_0) increased as line width and circle diameter were decreased to close to the exciton diffusion length. Circles were more efficient at enhancing exciton escape and increasing J_0 than lines. The J_0 increase in the nano-dot OLEDs containing nanopatterned circles with a diameter of 50 nm was approximately 41 times that of a conventional OLED with a current flow region of 4 mm^2. The dependence of J_0 on the size and shape of the nanopatterns was well explained by an SPA model that considered exciton diffusion. The results demonstrated that nanopatterning of OLEDs is a feasible method to obtain large J_0.

The contents of this chapter have been published in the following journal article:

"Suppression of external quantum efficiency roll-off of nanopatterned organic-light emitting diodes at high current densities", Journal of Applied Physics, vol.118, pp. 15501, 2015 [1].

5.1 Introduction

Over the past few decades, OLEDs have been extensively developed because of advantages like low-cost fabrication, light weight, flexibility, and a wide variety of emission wavelengths [2-4], which make it possible to use OLEDs as displays [5], lighting [6], and excitation sources for fluorescent detection systems [7]. Additionally, organic materials that show optical gain are attractive options for producing on-chip coherent light sources. In fact, there have been many reports on optically pumped organic semiconductor lasers [8-10]. However, despite a number of intensive studies, electrically pumped OSLDs have not yet been realized [11-14]. There are four major hurdles that need to be overcome to obtain OSLDs: (i) high current density injection and transport of over a few kA/cm^2 to achieve population inversion of excitons, (ii) suppression of bimolecular or heat annihilation processes [14-20], (iii) minimization of waveguide loss, such as light absorption by metal electrodes, and (iv) minimization of absorption loss by triplet excitons and polarons. Under optical pumping, these hurdles are surmounted because population inversion is easily obtained, few triplet excitons and polarons are formed, and metal electrodes are not required. In contrast, it is extremely difficult to overcome these issues simultaneously under electrical pumping.

Amplified spontaneous emission (ASE) from a multilayered OLED containing a bis-styrylbenzene derivative as a laser dye under optical pumping has been reported [20,21]. From the results, it was estimated that the current density required to induce electrical ASE was greater than kA/cm^2 from its optical ASE threshold energy. Operation of OLEDs at high current density (over kA/cm^2) has already been demonstrated by managing Joule heating using a small active area and substrate with high thermal conductivity [15,20,20-24]. In addition, short pulse operation can also suppress Joule heating [26-28]. However, dramatic roll-off of EQEs at high current densities was observed in these OLEDs because of the presence of bimolecular annihilation such as singlet–singlet annihilation (SSA) [14,15], singlet–triplet annihilation (STA) [16,17], and SPA [14,18-20]. Furthermore, singlet–heat annihilation (SHA) [15,22] causes efficiency roll-off of OLEDs operated at high

current densities because exciton dissociation induced by Joule heating cannot be neglected. The annihilation processes can be written as follows:

$$\textbf{SSA:}\ S_1 + S_1 \xrightarrow{k_{SS}} S_1 + S_0 \tag{5.1}$$

$$\textbf{STA:}\ S_1 + T_1 \xrightarrow{k_{ST}} S_0 + T_1 \tag{5.2}$$

$$\textbf{SPA:}\ S_1 + S_0^+ \ (or\ S_0^-) \xrightarrow{k_{SP}} S_0 + S_0^+ \ (or\ S_0^-) \tag{5.3}$$

$$\textbf{SHA:}\ S_1 + Phonon\ (heat) \xrightarrow{k_{heat}} S_0^+ + S_0^- \tag{5.4}$$

where k_{SS}, k_{ST}, k_{SP}, and k_{heat} are the exciton annihilation rate constants for SSA, STA, SPA, and SHA, respectively. S_0, S_1, T_1, and S_0^+ (or S_0^-) represent the ground state, singlet excited state, triplet excited state, and trapped charge carriers, which are assumed to annihilate singlet excitons, respectively. The influence of SSA and STA can be decreased by minimizing the overlap of the PL spectrum and the absorption spectrum of excited states using optimal materials. When OLEDs are electrically excited, electrons and holes injected from the electrodes and transported through the organic layers recombine in the emitting layer to generate excitons. Strong SPA occurs before the excitons decay radiatively because a number of excitons and charge carriers (polarons) coexist in the current flow region. To realize OSLDs, the above annihilation processes must be prevented to suppress efficiency roll-off.

In this study, to overcome this problem, we propose OLEDs with nanocurrent flow regions patterned by EB lithography. These devices are termed "nano-OLEDs", and the concept was developed in collaboration with Prof. Adachi's group at Kyushu University [25]. The mechanism of the nano-OLEDs is shown in Fig. 5.1(a). The charge carriers, which are trapped by the electric field, exist near the current flow region, while the excitons, which are electrically neutral, escape from the current flow region. Thus, our strategy to suppress SPA is to allow the generated excitons to escape from the current flow region (charge carriers) by decreasing the area of the current flow region to close to the exciton diffusion length. In addition, Joule heating is suppressed by the small size of the current flow regions. We prepared OLEDs with circular current flow regions, which are termed nano-dot

OLEDs, and linear current flow regions, coined nano-line OLEDs [25], to examine the effects of the current flow region shape on device characteristics, as shown in Fig. 5.1. We show that the nano-dot OLEDs are superior to the nano-line OLEDs in terms of both SPA suppression and higher current density injection. Moreover, we successfully explain the size- and shape-dependent SPA characteristics of the OLEDs using a theoretical SPA model that takes into account the directional dependence of the exciton diffusion length. Understanding the relationships between the shape and size of current flow regions, exciton diffusion, and SPA is an important step toward realizing OSLDs.

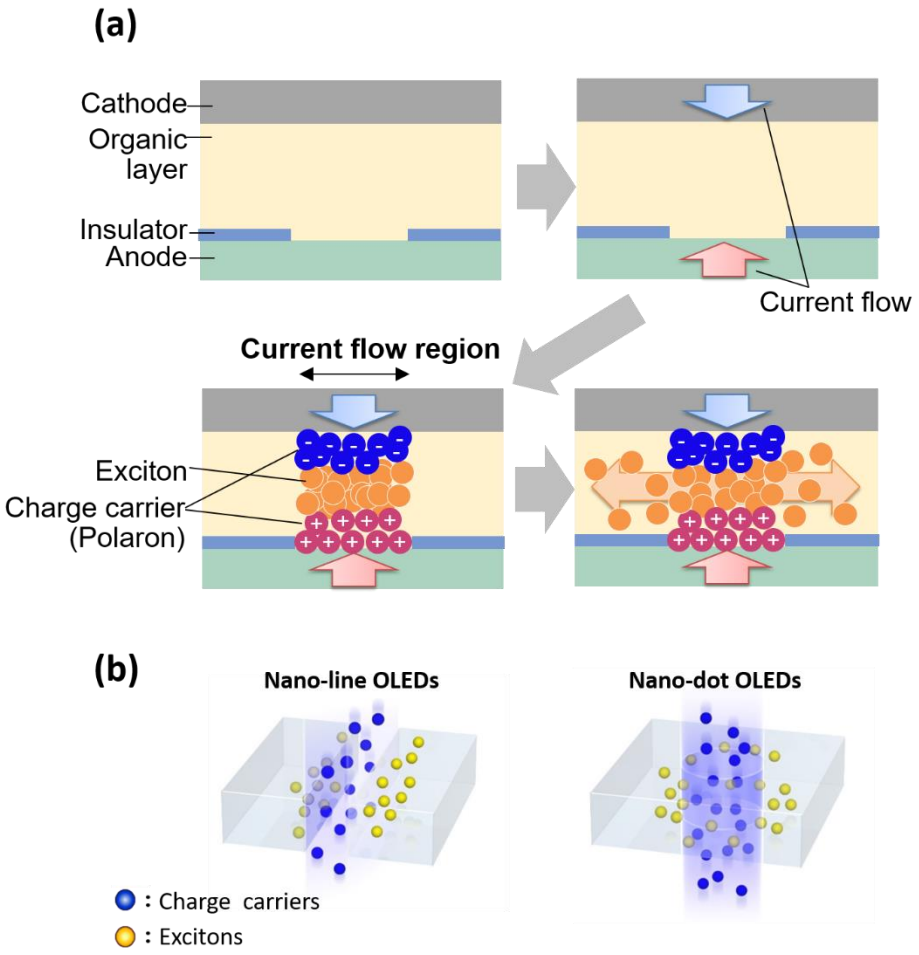

Figure 5.1 (a) Schematic diagram of exciton diffusion in nanopatterned OLEDs. (b) Exciton diffusion in one direction in a nano-line OLED (left) and diffusion in all directions in a nano-dot OLED (right) [1].

5.1.1 Theory for nano-OLEDs

The charge carrier mobility in an organic semiconductor is much lower than that in an inorganic semiconductor because of the potential barrier between the molecules. The electron and hole mobilities of 4,4´-bis[(N-carbazole)styryl]biphenyl (BSB-Cz), which is a promising material as the emitter of OSLDs and we used in the nano-OLEDs, are about μ_e~3×10^{-4} cm^2/Vs and μ_h~7×10^{-4} cm^2/Vs, respectively [19]. In addition, the diffusion coefficient of charge carrier (D_C) is given by the Einstein relationship:

$$D_C = \frac{kT\mu}{q} \tag{5.5}$$

,where k is Boltzmann's constant, T is the temperature, μ is the charge carrier mobility, and q is the electric charge. The time of flight (τ_C) of the charge carrier in the OLEDs is

$$\tau_C = \frac{d_f}{\mu E} = \frac{{d_f}^2}{\mu V} \tag{5.6}$$

,where d_f is the film thickness, E is the electrical field that is created in the film by the applied voltage (V). The spatial extent of charge carrier diffusion (L_c) is estimated by $L_c = \sqrt{\tau_C D_C}$. Therefore, L_c in the OLEDs is represented as follows:

$$L_c = d_f \sqrt{\frac{kT}{Vq}} \tag{5.7}$$

The L_c of 3 nm (at d_f = 100 nm, V = 30 V, and room temperature) is derived from the relationship, and it is minimized with increasing applied voltage.

In contrast, exciton is electrically neutral and stable at room temperature because the excitons in OLEDs are Frenkel excitons [29,30]; thus, they can diffuse based on Förester type energy transfer [31,32]. The previously reported exciton diffusion length of BSB-Cz is 13 nm [25]. Therefore, the difference between the diffusion lengths allows the charge carrier and the excitons to be separated.

5.2 Experiment

Nano-OLEDs were fabricated as illustrated in Fig. 5.2. ITO-coated glass substrates (100 nm ITO, Atsugi Micro Co.) were cleaned by conventional ultrasonication. A layer of hexamethyldisilazane (HMDS) was fabricated on each ITO surface by spin coating. A 35-nm-thick resist layer was spin-coated on each of the HMDS-treated substrates from a solution of ZEP-520A (Zeon Co.) diluted with anisole (1:3 v/v) and then heated at 180 °C for 3 min. The resist layers were pattered with lines with a length of 2 mm and width (d) of 80–230 nm or circles with a diameter (Φ) of 50–200 nm by EB lithography (JBX-5500, JEOL or ELS-7700W, Elionix Co.). The patterns were exposed with different dose amount from 6 μC/cm^2 to 160 μC/cm^2 by the acceleration of 75 kV. To enhance luminance from the nano-dot OLEDs, the circles were patterned on an area of 200 × 200 μm with a 200 nm interval between the edges of circles. The line patterns were developed by soaking the resist layers in developer (ZED-N50, Zeon Co.) at room temperature. To obtain precisely defined circular patterns, a cold development method where the developer was cooled below −10 °C [33,34] was used. The line and circle patterns formed on the resist layers were observed using scanning electron microscopy (SEM; S8240, Hitachi).

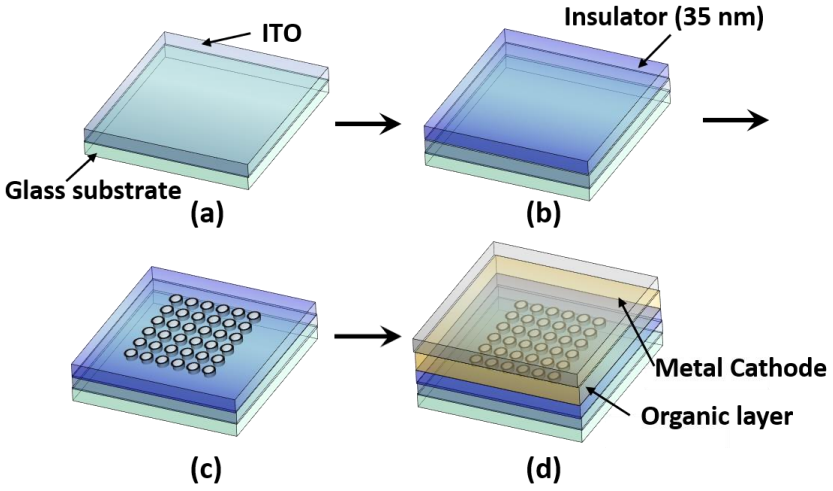

Figure 5.2 Schematic diagrams outlining the fabrication process of nano-dot OLEDs and the resulting OLED structure. (a) Glass substrate with a 100-nm-thick ITO anode layer. (b) Spin-coating resist on ITO as an insulator. (c) Development of nanopatterns by EB lithography. (d) Deposition of organic layers and metal cathode [1].

Several organic layers and a metal electrode were then vacuum-deposited on the line- and circle-patterned insulators under a base pressure of 10^{-4} Pa to fabricate OLEDs with the following architecture, as shown in Fig. 5.3(a): glass substrate/ITO anode (100 nm)/α-NPD hole-transport layer (60 nm)/mCP electron-blocking layer (10 nm)/BSB-Cz emitting layer (20 nm)/BCP hole-blocking layer (10 nm)/PoPy2 electron-transport layer (30 nm)/LiF electron-injection layer (0.8 nm)/Al cathode (100 nm), where α-NPD, mCP, BSB-Cz, BCP, and PoPy2 stand for 4,4´-bis[N-(1-naphthyl)-N-phenylamino]biphenyl, N,N-dicarbazolyl-3,5-benzene, 2,9-dimethyl-4,7-diphenyl-1,10-phenanthroline, and phenyldipyrenylphosphine oxide, respectively. The structures of these molecules are depicted in Fig. 5.3(b). BSB-Cz was used as the emitter because it shows a very low ASE threshold energy [24,35,36]. The resist layers left on the ITO surfaces acted as insulators. Therefore, the current flow regions of the OLEDs were limited to the line and circle regions. Reference OLEDs with a 2 × 2 mm current flow region, which was defined by the overlapping area of patterned ITO and Al, were fabricated without a resist insulating layer. The deposition rate was fixed at 0.2 nm/s for the organic layers, 0.01 nm/s for LiF, and 0.2 nm/s for Al. J–V–η_{ext} characteristics of the OLEDs were measured using an integrating sphere system (A10094, Hamamatsu Photonics) at room temperature.

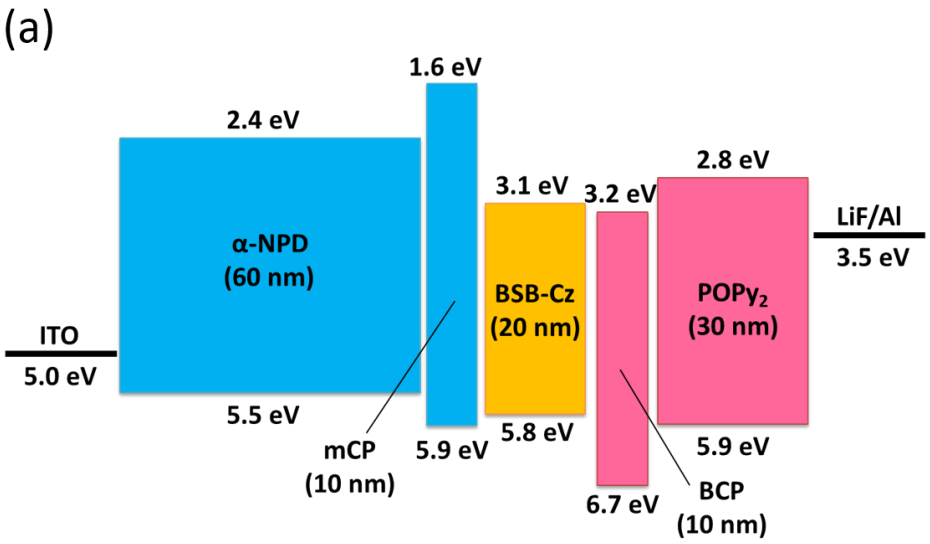

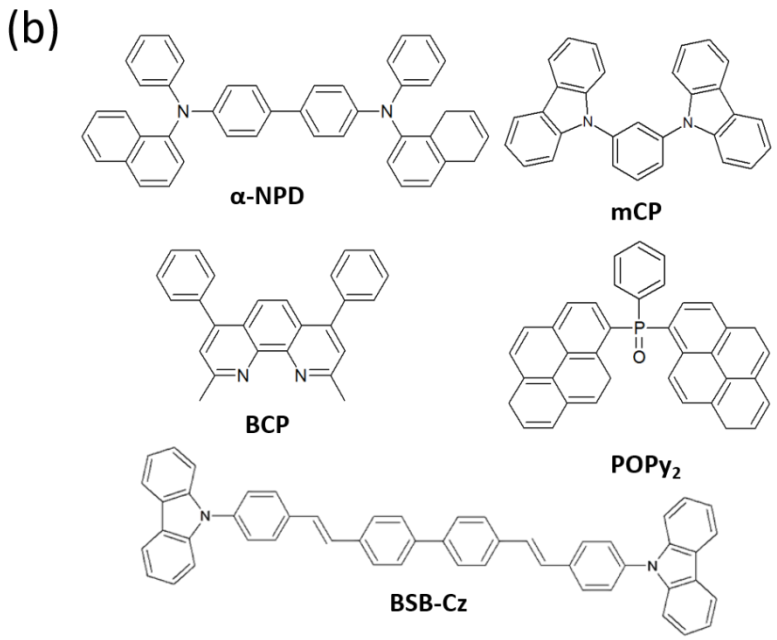

Figure 5.3 (a) Architecture and energy diagram of the nano-OLEDs. (b) Molecular structures of organic compounds used in the nano-OLEDs.

5.3 Results and discussion

5.3.1 Nanomask patterning with a cold development method

Figure 5.4 shows SEM images of the circle patterns fabricated with and without using the cold development method. When the circle patterns were developed at room temperature (Fig. 5.4(a)), the obtained Φ (approximately 139 nm) was much larger than the design value of 100 nm. This is because it is difficult to form precisely defined patterns in a very thin EB resist layer (ZEP-520A) spin-coated on an ITO layer as there is excess exposure of the resist layer by electrons backscattered from the ITO layer [37]. In contrast, the cold development method gave well-defined circle patterns with Φ = ~103 nm, very close to the design value of 100 nm, as illustrated in Fig. 5.4(b). This is because intermediate-molecular-weight chain segments in the unnecessarily exposed regions of the resist layer were frozen out and not developed by the cold developer, as reported by Ocola and Stein [34,35].

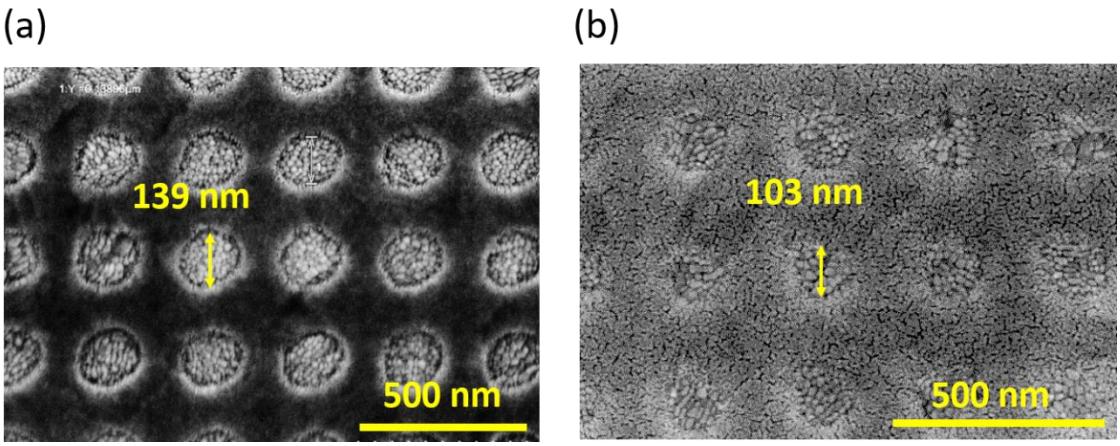

Figure 5.4 Effect of development method on the exposed area for a pattern design with Φ = 100 nm. Dot patterns formed in a 35-nm-thick resist layer using (a) conventional room-temperature development and (b) cold development [1].

SEM images of the line and circle patterns with different d and Φ are presented in Fig. 5.5. Well-defined linear patterns could be obtained without using the cold development method because the electron backscattering effect is not large when fabricating "single" line patterns. The errors of d and Φ between the obtained and designed patterns were less than 5%. Additionally, no resist residue was left inside the patterns because ITO grains are clearly visible. Figure 5.6 shows photographs of the nano-line and nano-dot OLEDs under DC operation. The EL emission was line- or dot-shaped and no EL was observed in the insulating resist regions, indicating that the current flow regions were successfully limited to inside the line and dot regions.

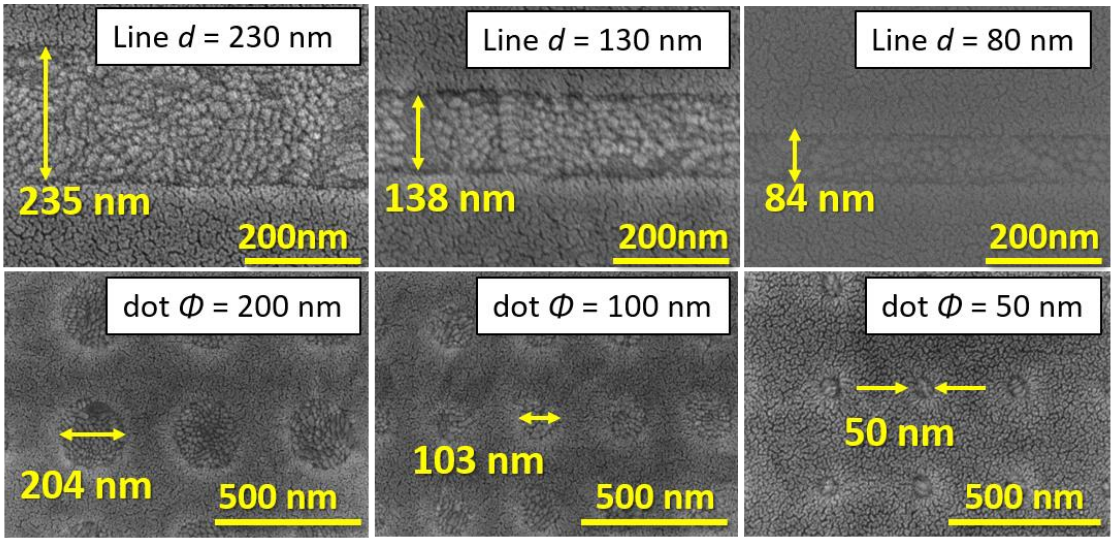

Figure 5.5 SEM images of line- and circle-patterned insulator layers [1].

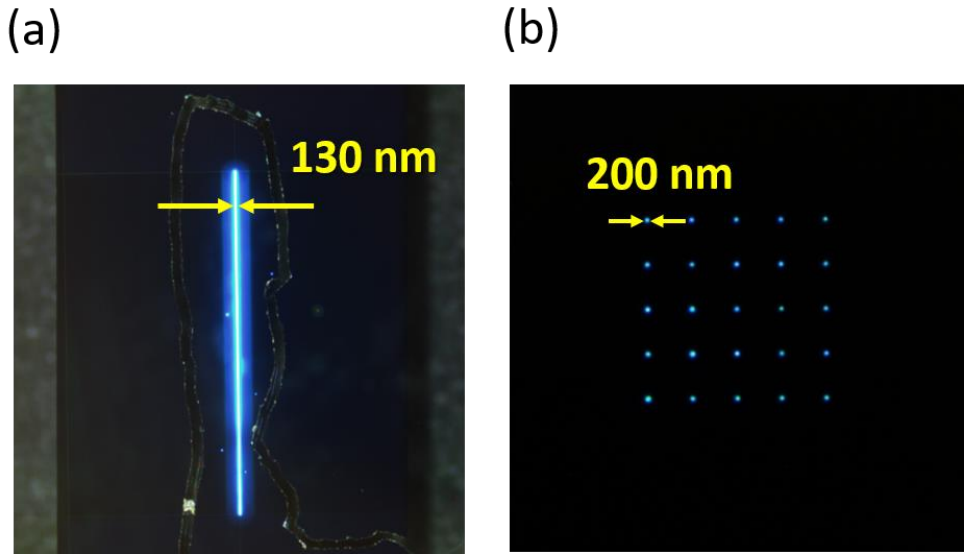

Figure 5.6 Top-view photomicrograph of EL emission from the nano-OLEDs with (a) line pattern (d = 130 nm) and (b) circle pattern (Φ = 200 nm) [1].

5.3.3 Evaluation of nano-OLEDs

Figure 5.7 illustrates the $J-V$ characteristics of the nanoline, nanodot, and reference OLEDs operated under DC conditions. J was calculated by dividing the measured currents by the pattern areas estimated from the SEM images. All OLEDs displayed the same $J-V$ curves, indicating that the estimations of the pattern area

and J were correct. For the reference OLEDs, the maximum current density (J_{max}) observed just before device breakdown was as small as 1.0 A/cm^2. However, J_{max} dramatically increased as d and Φ decreased. The highest J_{max} was 65.3 A/cm^2 for the nano-line OLED with the smallest d of 80 nm and 113 A/cm^2 for the nano-dot OLED with the smallest Φ of 50 nm. Previous studies showed that OLED breakdown is related to the melting of organic layers induced by Joule heating [38,39]. Therefore, Joule heating is suppressed, especially in the nano-dot OLEDs, because the generated Joule heat can diffuse from the current flow regions to the surrounding resist layers [15,22,25,39].

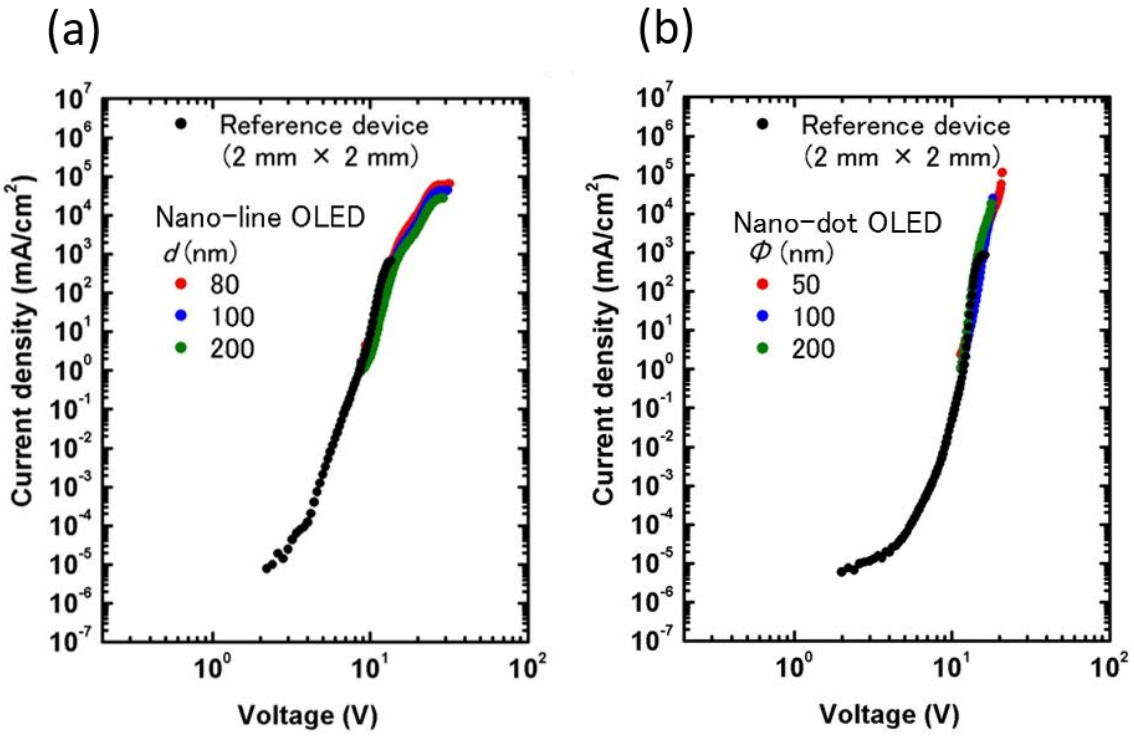

Figure 5.7 Current density (J)–voltage (V) characteristics of (a) nanoline and (b) nano-dot OLEDs along with those of the reference OLED [1].

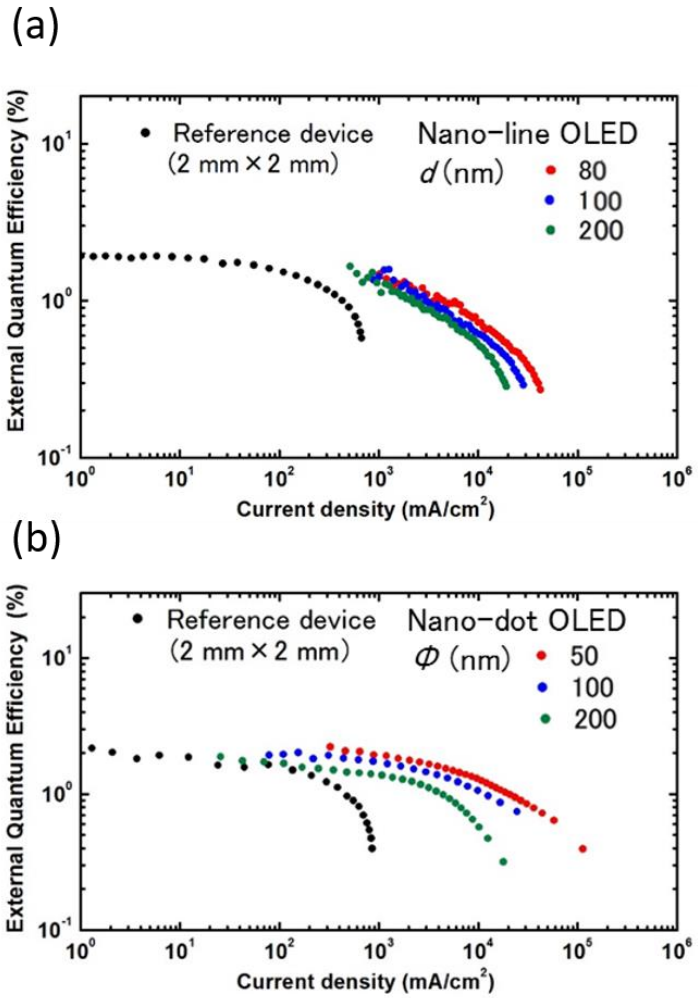

Figure 5.8 External quantum efficiency (η)–current density (J) characteristics of (a) nano-line and (b) nano-dot OLEDs along with those of the reference OLED [1].

The $\eta-J$ characteristics of the nanoline, nanodot, and reference OLEDs are presented in Fig. 5.8. Substantial roll-off of η was observed for the reference OLED when J exceeded 0.1 A/cm^2. BSB-Cz shows ASE with a low threshold energy [24,36,37] and the spectral overlap between its emission and triplet absorption is very small [37], indicating that SSA and STA are likely to be negligible. Therefore, the observed η roll-off is mainly attributable to either SPA or SHA. In contrast, the η roll-off was strongly suppressed as d and Φ decreased. Figure 5.9 shows plots of current density when the efficiency is half the initial value (J_0) against d and Φ for the nano-line and nano-dot OLEDs, respectively. The J_0-d plots of the nano-line

OLEDs are consistent with those reported previously [25]. The increase of J_0 at smaller Φ of the nano-dot OLEDs was larger than the equivalent change of the nano-line OLEDs, suggesting that the escape of excitons is more efficient in the nano-dot OLEDs than in the nano-line ones.

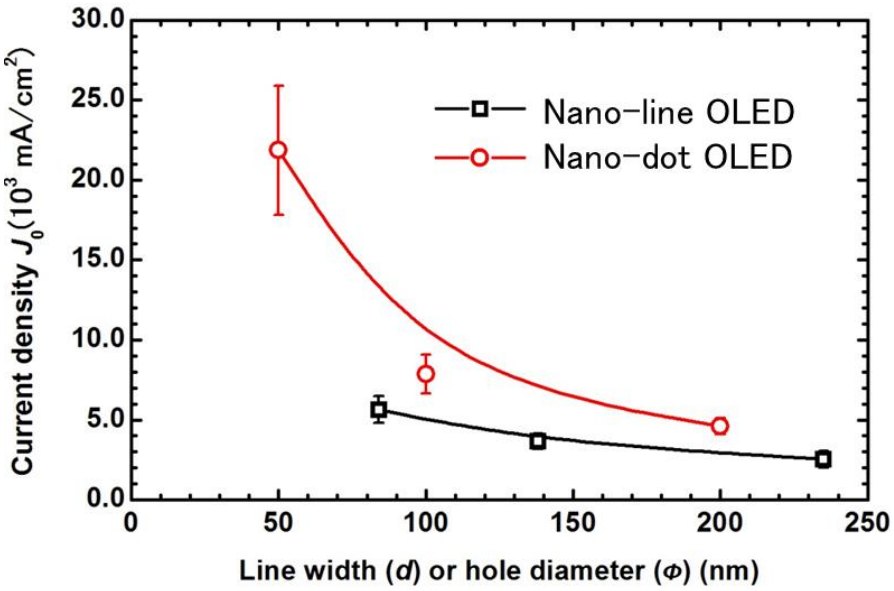

Figure 5.9 Plots of pattern size (d and Φ) against current density when the efficiency is half the initial value (J_0) obtained from the comparison of the $\eta-J$ characteristics of the nano-line and nano-dot OLEDs [1].

5.3.3 Comparison with theoretical model

We discuss the dependence of J_0 on d and Φ using an SPA model. First, the effect of device size on roll-off in the nano-OLEDs was considered based on an SPA model (Eq. (5.3)). Here, the concentration of singlet excitons ($[S_1^*]$) follows [25]:

$$\frac{d[S_1^*]}{dt} = -\frac{[S_1^*]}{\tau} - k_{SP}[n_c]\left[\underline{S_1^*}\right] + \frac{J}{4qd_t} \tag{5.8}$$

where τ is the lifetime of singlet excitons, d_t is the thickness of the recombination zone, $[n_c]$ represents the concentration of trapped charge carriers, and $\left[\underline{S_1^*}\right]$ represents the concentration of excitons confined in the current flow region

interacting with polarons. The exciton generation denoted by $\frac{J}{4qd_t}$ was used to account for the singlet to triplet generation ratio of 1:3 based on spin statistics [40]. Thus, $\left[\underline{S_1^*}\right]$ can be decreased, leading to the suppression of SPA and roll-off. Here, we defined $\left[\underline{S_1^*}\right]$ as $(1-z)[S_1^*]$ using the unconfinement factor (z), which represents the ratio of excitons that escape from the carrier flow region; these excitons do not interact with polarons. Because $[n_c]\sim CJ^{\frac{1}{l+1}}$ based on the trapped-charge-limited current model [24,40-42], Eq. (5.8) can be modified as follows:

$$\frac{d[S_1^*]}{dt} = -\frac{[S_1^*]}{\tau} - k_{SP}(1-z)[S_1^*]CJ^{\frac{1}{l+1}} + \frac{J}{4qd_t} \tag{5.9}$$

$$C = \left[\left(\frac{l+1}{2l+1}\right)\left(\frac{l+1}{l}\right)\left(\frac{{N_t}^l\varepsilon}{d_t q^2 \mu N_C}\right)\right]^{\frac{1}{l+1}} \quad , \quad l = \frac{E_t}{kT} \tag{5.10}$$

where N_C is the density of states, N_t is the trap density, E_t is the trap depth, and ε is the permittivity. The current density dependence of EQE can be calculated based on the SPA model from the steady-state solutions of Eq. (5.9), giving

$$\frac{\eta}{\eta_0} = \frac{1}{1+\left(\frac{J}{J_0}\right)^{1/(l+1)}}. \tag{5.11}$$

Here, η_0 is the quantum efficiency in the absence of SPA, and

$$J_0 = \left(\frac{1}{\tau k_{SP} C(1-z)}\right)^{l+1} = \left(\frac{1}{\tau k_{SP} C}\right)^{l+1}\left(\frac{1}{1-z}\right)^{l+1} \tag{5.12}$$

is the current density at $\eta = \eta_0/2$. The observed J_0 of the reference device under pulsed operation yielded $\left(\frac{1}{\tau k_{SP} C(1-z)}\right)^{l+1}$ = 1920 mA/cm^2, because z was almost zero and the Joule heating effect was negligible. Then, we found l by fitting the roll-off characteristics of the reference device under pulsed operation by Eq. (5.11). The experimental curve was well fitted by the SPA model when l = 1.41 and J_0 = 2.88 A/cm^2 because SPA occurred and SHA was suppressed in the reference device under pulsed excitation, as shown in Fig. 5.10 [20,22].

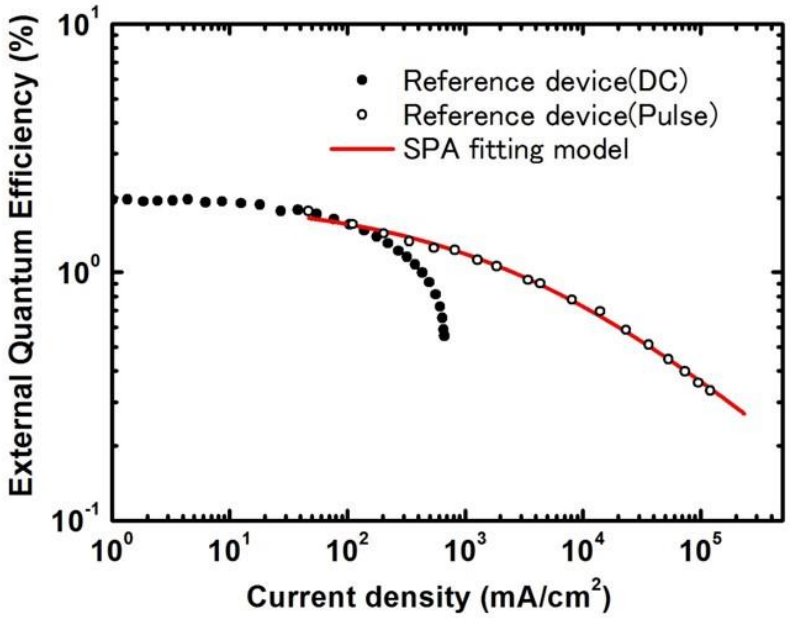

Figure 5.10 η–J characteristics of the reference device under DC and pulse operation and SPA model fitting [1].

Next, to find the theoretical values of J_0, we calculated z by solving the following singlet exciton diffusion equations:

Nano-line OLEDs:

$$D_{\mathrm{S}}\frac{d^2[\mathrm{S}_1^*]}{dx^2} - (k_{\mathrm{r}} + k_{\mathrm{nr}} + k_{\mathrm{isc}})[\mathrm{S}_1^*] + k_{\mathrm{risc}}[\mathrm{T}_1^*] + k_{\mathrm{tta}}[\mathrm{T}_1^*]^2 + R = 0 \tag{5.13}$$

Nano-dot OLEDs:

$$D_{\mathrm{S}}\left(\frac{d^2[\mathrm{S}_1^*]}{dx^2} + \frac{d^2[\mathrm{S}_1^*]}{dy^2}\right) - (k_{\mathrm{r}} + k_{\mathrm{nr}} + k_{\mathrm{isc}})[\mathrm{S}_1^*] + k_{\mathrm{risc}}[\mathrm{T}_1^*] + k_{\mathrm{TT}}[\mathrm{T}_1^*]^2 + R = 0 \tag{5.14}$$

$$D_{\mathrm{S}} = \frac{{L_{\mathrm{D}}}^2}{\tau} \quad , \quad R = \frac{J}{4qd_{\mathrm{t}}} \tag{5.15}$$

where $[\mathrm{T}_1^*]$ is the triplet exciton density, D_{S} is the singlet exciton diffusivity, L_{D} is the exciton diffusion length in the emitting layer, R is the rate of singlet exciton generation, q is the electric charge, d_{t} is the thickness of the recombination area, k_{r} is the rate of radiative decay, k_{nr} is the rate of nonradiative decay, k_{isc} is the

rate of ISC, k_{risc} is the rate of RISC, and k_{TT} is the rate of triplet–triplet annihilation (TTA) [44]. In the calculations, we used $\tau = 1.0 \times 10^{-9}$ s, $q = 1.6 \times 10^{-19}$ C, $d_{\mathrm{t}} = 20$ nm, $k_{\mathrm{r}} = 1.0 \times 10^{9}$ /s, $k_{\mathrm{nr}} = 1.0 \times 10^{6}$ /s, and $k_{\mathrm{isc}} = 1 \times 10^{6}$ /s. As a first approximation, we omitted exciton upconversion and TTA processes for simplicity. Fig. 5.11 presents the exciton distribution calculated (Mathematica, Wolfram Research) using Eq. (5.14) for the reference and nano-dot OLEDs with $\Phi = 200$ and 50 nm, where J is a constant value of 1 A/cm^2, and L_{D} of a neat film of BSB-Cz is 13 nm [25]. Although almost all of the generated excitons existed inside the carrier flow region in the reference device, the rate that excitons escaped the carrier flow region increased as the diameter of the circles in the nano-dot OLEDs decreased, and 39% of excitons diffused out of the carrier flow region of the nano-dot OLEDs with the smallest Φ of 50 nm. The results of the calculation of z for the nano-line and nano-dot OLEDs are summarized in Fig. 5.12. These results indicate that decreasing d or Φ promotes the separation of excitons from polarons, and this tendency toward separation is greater in the nano-dot OLEDs than in the nano-line OLEDs.

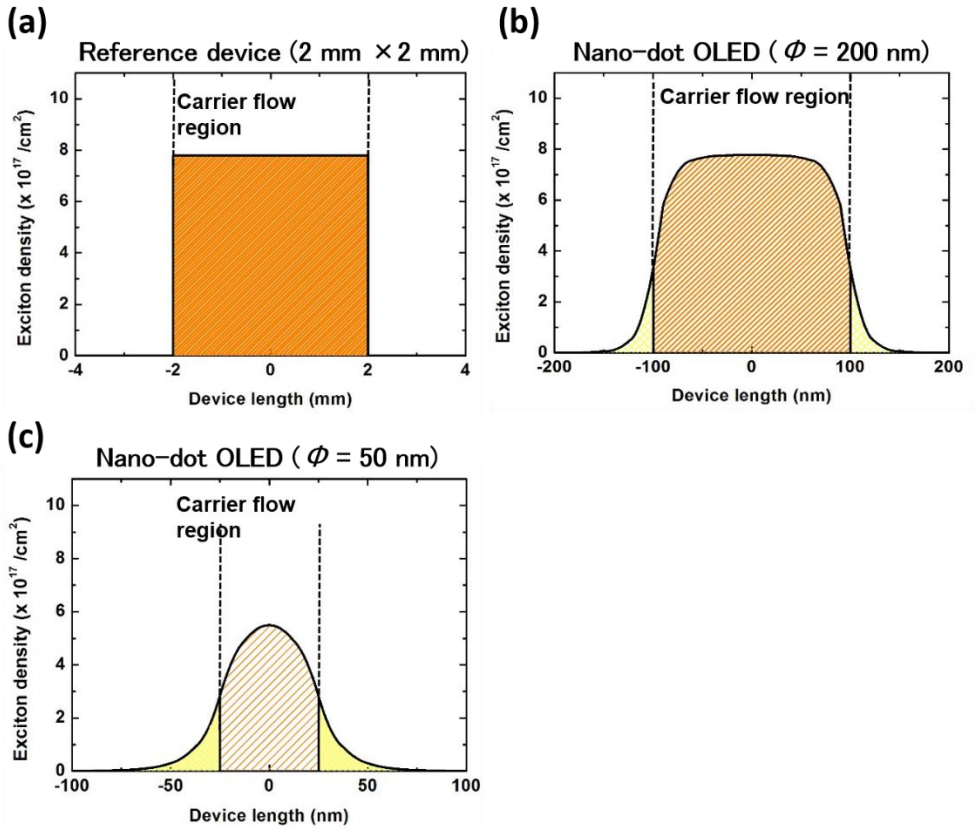

Figure 5.11 Solutions of the exciton diffusion simulations for (a) the reference device and nano-dot OLEDs with (b) Φ = 50 and (c) Φ = 200 nm [1].

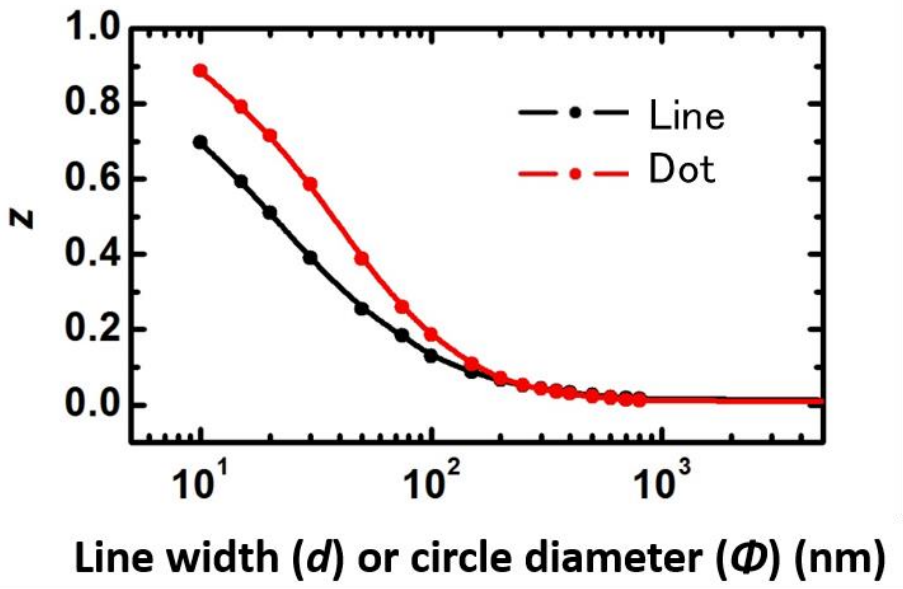

Figure 5.12 Plots of the calculated unconfinement factor of excitons (z) against pattern size (d and Φ) in nano-line and nano-dot OLEDs, respectively [1].

Now, we discuss the roll-off characteristics of the devices based on the above SPA model by comparing the experimental and theoretical J_0 values. Figure 5.13(a) and (b) show J_0–d plots for the nano-line OLEDs and J_0–Φ plots for the nano-dot OLEDs, respectively. The black, green, orange, and blue lines are the theoretical curves of the SPA model with L_D = 13, 18, 21, and 24 nm, respectively. The experimental data are the average values and their standard deviations obtained from OLEDs fabricated in different batches. For both types of devices, the experimental data are close to the theoretical curves calculated using L_D = 18 and 24 nm, although these curves are higher than the curve calculated using the previously reported value of L_D = 13 nm [25].

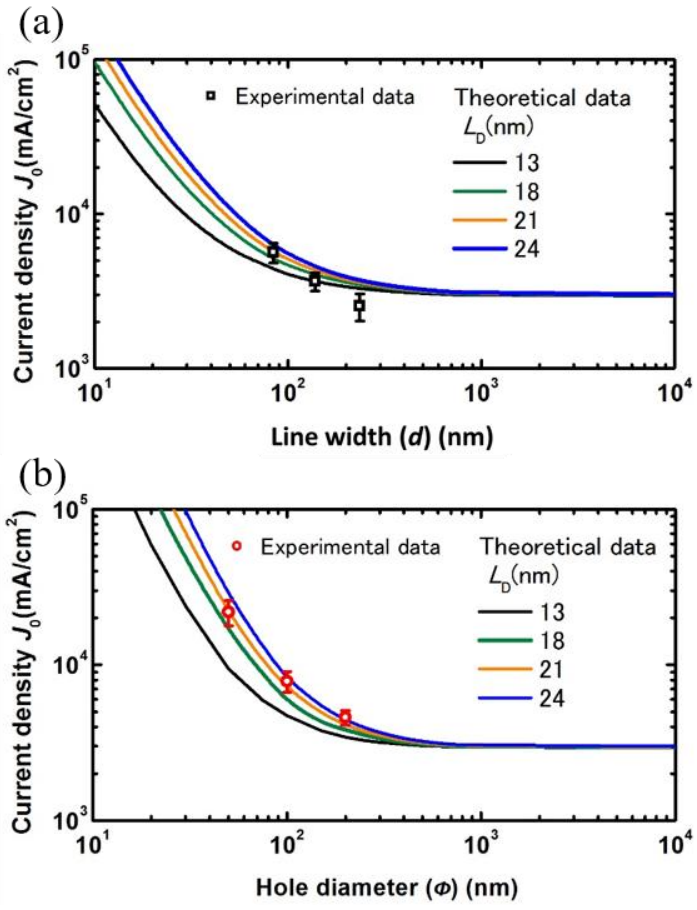

Figure 5.13 Dependence of (a) current density when the efficiency is half the initial value (J_0)–d characteristics of nano-line OLEDs and (b) J_0–Φ characteristics of nano-dot OLEDs determined from the SPA model using exciton diffusion lengths (L_D) of 13, 18, 21, and 24 nm [1].

To explain the above results, we took into consideration the orientation of BSB-Cz molecules. Because the reported experimental L_D value was calculated using a PL quenching method, this value indicates the exciton diffusion length normal to the substrate plane [25,45,46]. However, knowledge of the lateral diffusion length is necessary to solve the diffusion equation. If the molecular orientation of the emitting layer is completely random, the diffusion length in both directions should be the same. However, BSB-Cz exhibits molecular orientation even in an amorphous film [47]. Therefore, the vertical and lateral diffusion lengths of BSB-Cz would be slightly different from one another. The diffusion length is expressed as

$$L_D = \sqrt{\frac{\kappa^2 \Phi_F}{8\pi n^4} \frac{\sigma}{a^4}} = \frac{1}{\sqrt{6}} \frac{{R_0}^3}{a^2}, \tag{5.16}$$

$$\begin{aligned} \kappa^2 &= (\cos\theta_{DA} - 3\cos\theta_D \cos\theta_A)^2 \\ &= (\sin\theta_D \sin\theta_A \cos\varphi - 2\cos\theta_D \cos\theta_A)^2, \end{aligned} \tag{5.17}$$

where Φ_F is the fluorescence yield, κ is the transition dipole orientation factor, σ is the overlap integral between the emission and absorption spectra, n is the index of refraction at the wavelength where σ is at its maximum, a is the lattice constant of a simple cubic lattice, R_0 is the Förster radius within a film of homogeneous composition, θ_{DA} is the angle between the transition moments of the donor and acceptor (θ_D and θ_A, respectively, are the angles between the transition moments), and φ is the angle between the projections of the transition moments on a plane perpendicular to the line through the centers of each molecule [48,49]. When we took into account that the BSB-Cz molecules in the film were nearly parallel [47], the value of κ was different in the vertical and lateral directions.

We then assumed that all of the BSB-Cz molecules in the film were in a horizontally oriented amorphous state and calculated κ for the vertical and lateral directions. That is, κ for BSB-Cz molecules in the vertical direction was calculated using Eq. (5.17) with $\theta_D = \theta_A = 0°$ and $\theta_{DA} = \varphi$, while κ for BSB-Cz molecules in the lateral direction was calculated with $\varphi = 0°$ or $\varphi = 180°$. According to these calculations, the value of κ in the lateral direction was 1.58 times greater than that

in the vertical direction, i.e., the lateral diffusion length of BSB-Cz was 1.58 times greater than that in the vertical direction, and estimated to be 21 nm. Figure 5.14 shows the experimental and theoretical J_0–d and J_0–Φ plots for the nano-OLEDs with L_D = 21 nm. The experimental data closely agree with the theoretical curves; therefore, we conclude that the roll-off behavior of the devices was suppressed based on the above SPA model by making the pattern size smaller. The experimental data for the nano-line OLEDs deviates from the theoretical curve as d increases; this can be ascribed to the decrease in J_0 caused by Joule heating.

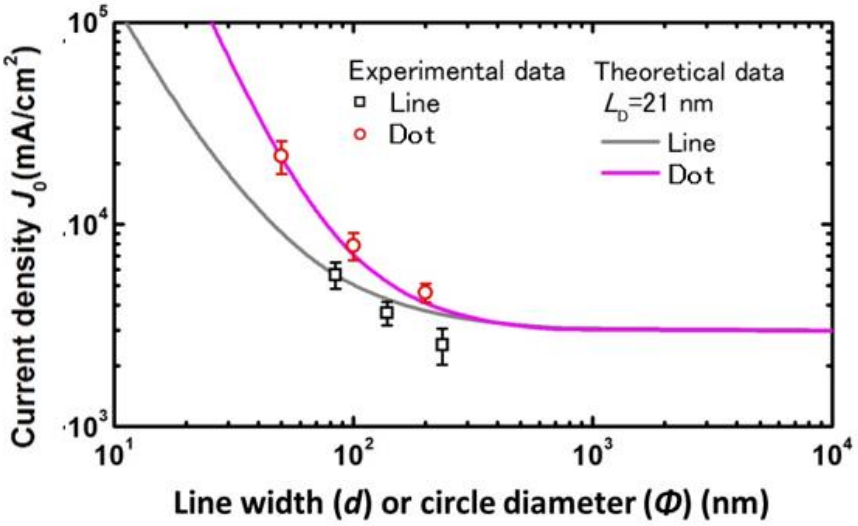

Figure 5.14 Recalculated J_0–pattern size (d and Φ) characteristics of the nano-OLEDs determined from experimental results and the theoretical results obtained using Eq. (5.16) [1].

5.4 Summary

We demonstrated the suppression of the η roll-off of nano-OLEDs by decreasing the device area to close to the exciton diffusion length by introducing dot- or line-patterned insulator layers. Roll-off was less pronounced in the nano-dot OLEDs than in the nano-line OLEDs, and J_0 was greater than 20 A/cm^2 when Φ of the circle patterns was 50 nm. Therefore, such a circle pattern is applicable for practical OSLDs and high-brightness applications.

The achievements in this study are depicted in Fig. 5.15. The nano-OLED cannot completely suppress the roll-off behavior; however, we believe that the remaining roll-off is a result of the short exciton diffusion length of the BSB-Cz layer. We expect that other materials with a longer exciton diffusion length, such as single-crystal films, can be used in these structured devices to help suppress the remaining η roll-off. In addition, high current injection to the nano-OLEDs by using a substrate with high thermal conductivity or short pulse operation and lowering the ASE threshold itself by including a resonator structure in the nano-OLEDs are promising approaches to realize OSLDs.

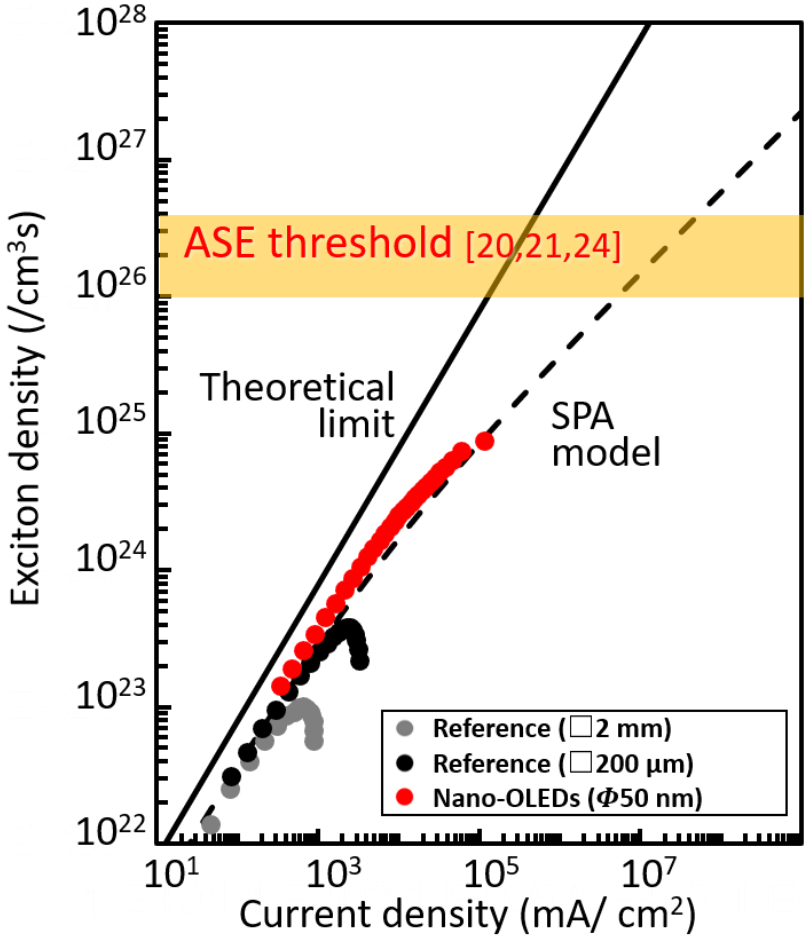

Figure 5.15 Exciton density–current density (J) characteristics of the nano-OLEDs and reference device. The ASE threshold of BSB-Cz reported previously is shown.

References

[1] H. Kuwae, A. Nitta, K. Yoshida, T. Kasahara, T. Matsushima, M. Inoue, S. Shoji, J. Mizuno and C. Adachi, "Suppression of external quantum efficiency roll-off of nanopatterned organic-light emitting diodes at high current densities," J. Appl. Phys., vol. 118, pp. 155501, 2015.

[2] C. W. Tang and S. VanSlyke, "Organic electroluminescent diodes," Appl. Phys. Lett., vol. 51, pp. 913-915, 1987.

[3] S. R. Forrest, "The path to ubiquitous and low-cost organic electronic appliances on plastic," Nature, vol. 428, pp. 911-918, 2004.

[4] C. D. Müller, A. Falcou, N. Reckefuss, M. Rojahn, V. Wiederhirn, P. Rudati, H. Frohne, O. Nuyken, H. Becker and K. Meerholz, "Multi-colour organic light-emitting displays by solution processing," Nature, vol. 421, pp. 829-833, 2003.

[5] L. Xiao, Z. Chen, B. Qu, J. Luo, S. Kong, Q. Gong and J. Kido, "Recent Progresses on Materials for Electrophosphorescent Organic Light‐Emitting Devices," Adv. Mater., vol. 23, pp. 926-952, 2011.

[6] B. W. D'Andrade and S. R. Forrest, "White organic light‐emitting devices for solid‐state lighting," Adv. Mater., vol. 16, pp. 1585-1595, 2004.

[7] F. Lefevre, A. Chalifour, L. Yu, V. Chodavarapu, P. Juneau and R. Izquierdo, "Algal fluorescence sensor integrated into a microfluidic chip for water pollutant detection," Lab. Chip, vol. 12, pp. 787-793, 2012.

[8] D. Moses, "High quantum efficiency luminescence from a conducting polymer in solution: A novel polymer laser dye," Appl. Phys. Lett., vol. 60, pp. 3215-3216, 1992.

[9] F. Hide, M. A. Diaz-Garcia, B. J. Schwartz, M. R. Andersson, Q. Pei and A. J. Heeger, "Semiconducting polymers: a new class of solid-state laser materials," Science, vol. 273, pp. 1833-1836, 1996.

[10] V. Kozlov, V. Bulović, P. Burrows and S. Forrest, "Laser action in organic semiconductor waveguide and double-heterostructure devices," Nature, vol. 389, pp. 362-364, 1997.

[11] N. Tessler, G. Denton and R. Friend, "Lasing from conjugated-polymer

microcavities," Nature, vol. 382, pp. 695-697, 1996.

[12] F. Hide, M. A. Diaz-Garcia, B. J. Schwartz, M. R. Andersson, Q. Pei and A. J. Heeger, "Semiconducting polymers: a new class of solid-state laser materials," Science, vol. 273, pp. 1833-1836, 1996.

[13] V. Kozlov, V. Bulovic, P. Burrows, M. Baldo, V. Khalfin, G. Parthasarathy, S. Forrest, Y. You and M. Thompson, "Study of lasing action based on Förster energy transfer in optically pumped organic semiconductor thin films," J. Appl. Phys., vol. 84, pp. 4096-4108, 1998.

[14] M. Baldo, R. Holmes and S. Forrest, "Prospects for electrically pumped organic lasers," Phys. Lett. B, vol. 66, pp. 035321, 2002.

[15] H. Nakanotani, H. Sasabe and C. Adachi, "Singlet-singlet and singlet-heat annihilations in fluorescence-based organic light-emitting diodes under steady-state high current density," Appl. Phys. Lett., vol. 86, pp. 213506-213506-3, 2005.

[16] C. Gärtner, C. Karnutsch, U. Lemmer and C. Pflumm, "The influence of annihilation processes on the threshold current density of organic laser diodes," J. Appl. Phys., vol. 101, pp. 023107, 2007.

[17] Y. Zhang and S. R. Forrest, "Triplets contribute to both an increase and loss in fluorescent yield in organic light emitting diodes," Phys. Rev. Lett., vol. 108, pp. 267404, 2012.

[18] E. List, C. Kim, A. Naik, U. Scherf, G. Leising, W. Graupner and J. Shinar, "Interaction of singlet excitons with polarons in wide band-gap organic semiconductors: A quantitative study," Phys. Rev. B, vol. 64, pp. 155204, 2001.

[19] A. Howard, J. M. Hodgkiss, X. Zhang, K. R. Kirov, H. A. Bronstein, C. K. Williams, R. H. Friend, S. Westenhoff and N. C. Greenham, "Charge recombination and exciton annihilation reactions in conjugated polymer blends," J. Am. Chem. Soc., vol. 132, pp. 328-335, 2009.

[20] Y. Setoguchi and C. Adachi, "Suppression of roll-off characteristics of electroluminescence at high current densities in organic light emitting diodes by introducing reduced carrier injection barriers," J. Appl. Phys., vol. 108, pp.

064516, 2010.

[21] H. Yamamoto, T. Oyamada, H. Sasabe and C. Adachi, "Amplified spontaneous emission under optical pumping from an organic semiconductor laser structure equipped with transparent carrier injection electrodes," Appl. Phys. Lett., vol. 84, pp. 1401-1403, 2004.

[22] H. Nakanotani, T. Oyamada, Y. Kawamura, H. Sasabe and C. Adachi, "Injection and Transport of High Current Density over 1000 A/cm¬¬2 in Organic Light Emitting Diodes under Pulse Excitation," Jpn. J. Appl. Phys., vol. 44, pp. 3659, 2005.

[23] T. Matsushima and C. Adachi, "High-current Injection and Transport on Order of kA/cm2 in Organic Light-emitting Diodes Having Mixed Organic/Organic Heterojunction Interfaces," Jpn. J. Appl. Phys., vol. 46, pp. L861, 2007.

[24] M. Inoue, K. Goushi, K. Endo, H. Nomura and C. Adachi, "Reduced amplified spontaneous emission threshold in organic semiconductor laser structure with relaxed roll-off characteristics under high current densities," J. Lumin., vol. 143, pp. 754-758, 2013.

[25] K. Hayashi, H. Nakanotani, M. Inoue, K. Yoshida, O. Mikhnenko, T. Nguyen and C. Adachi, "Suppression of roll-off characteristics of organic light-emitting diodes by narrowing current injection/transport area to 50 nm," Appl. Phys. Lett., vol. 106, pp. 093301, 2015.

[26] K. Yoshida, T. Matsushima, H. Nakanotani and C. Adachi, "Quantification of temperature rise in unipolar organic conductors during short voltage-pulse excitation using electrical testing methods," Org. Electron., vol. 31, pp. 191-197, 2016.

[27] K. Yoshida, H. Nakanotani and C. Adachi, "Effect of Joule heating on transient current and electroluminescence in pin organic light-emitting diodes under pulsed voltage operation," Org. Electron., vol. 31, pp. 287-294, 2016.

[28] K. Yoshida, T. Matsushima, Y. Shiihara, H. Kuwae, J. Mizuno and C. Adachi, "Joule heat-induced breakdown of organic thin-film devices under pulse operation," J. Appl. Phys., vol. 121, pp. 195503, 2017.

[29] N. S. Sariciftci, Primary Photoexcitations in Conjugated Polymers: Molecular Excitation Versus Semiconductor Band Model. World Scientific, 1997.

[30] P. K. Nayak and N. Periasamy, "Calculation of electron affinity, ionization potential, transport gap, optical band gap and exciton binding energy of organic solids using 'solvation'model and DFT," Org. Electron., vol. 10, pp. 1396-1400, 2009.

[31] T. Förster, "Zwischenmolekulare energiewanderung und fluoreszenz," Annalen Der Physik, vol. 437, pp. 55-75, 1948.

[32] S. D. Babenko, V. A. Benderskii, V. I. Gol'danskii, A. G. Lavrushko and V. P. Tychinskii, "Annihilation of singlet excited states in anthracene solutions," Chem. Phys. Lett., vol. 8, pp. 598-600, 1971.

[33] W. W. Hu, K. Sarveswaran, M. Lieberman and G. H. Bernstein, "Sub-10 nm electron beam lithography using cold development of poly (methylmethacrylate)," J. Vac. Sci. Technol. B, vol. 22, pp. 1711-1716, 2004.

[34] L. Ocola and A. Stein, "Effect of cold development on improvement in electron-beam nanopatterning resolution and line roughness," J. Vac. Sci. Technol. B, vol. 24, pp. 3061-3065, 2006.

[35] T. Aimono, Y. Kawamura, K. Goushi, H. Yamamoto, H. Sasabe and C. Adachi, "100% fluorescence efficiency of 4, 4′ -bis [(N-carbazole) styryl] biphenyl in a solid film and the very low amplified spontaneous emission threshold," Appl. Phys. Lett., vol. 86, pp. 071110-071110-3, 2005.

[36] H. Nakanotani, C. Adachi, S. Watanabe and R. Katoh, "Spectrally narrow emission from organic films under continuous-wave excitation," Appl. Phys. Lett., vol. 90, pp. 231109-231109-3, 2007.

[37] R. Hawryluk, A. M. Hawryluk and H. I. Smith, "Energy dissipation in a thin polymer film by electron beam scattering," J. Appl. Phys., vol. 45, pp. 2551-2566, 1974.

[38] N. Tessler, N. Harrison, D. Thomas and R. Friend, "Current heating in polymer light emitting diodes," Appl. Phys. Lett., vol. 73, pp. 732-734, 1998.

[39] T. Matsushima, H. Sasabe and C. Adachi, "Carrier injection and transport

characteristics of copper phthalocyanine thin films under low to extremely high current densities," Appl. Phys. Lett., vol. 88, pp. 033508-033508-3, 2006.

[40] W. Helfrich and W. Schneider, "Recombination radiation in anthracene crystals," Phys. Rev. Lett., vol. 14, pp. 229, 1965.

[41] P. Mark and W. Helfrich, "Space - charge - limited currents in organic crystals," J. Appl. Phys., vol. 33, pp. 205-215, 1962.

[42] P. Burrows and S. Forrest, "Electroluminescence from trap - limited current transport in vacuum deposited organic light emitting devices," Appl. Phys. Lett., vol. 64, pp. 2285-2287, 1994.

[43] P. Burrows, Z. Shen, V. Bulovic, D. McCarty, S. Forrest, J. Cronin and M. Thompson, "Relationship between electroluminescence and current transport in organic heterojunction light - emitting devices," J. Appl. Phys., vol. 79, pp. 7991-8006, 1996.

[44] Y. Luo, H. Aziz, G. Xu and Z. D. Popovic, "Effect of exciton diffusion on electroluminescence of organic light-emitting devices," Org. Electron., vol. 9, pp. 1128-1131, 2008.

[45] P. Peumans, A. Yakimov and S. R. Forrest, "Small molecular weight organic thin-film photodetectors and solar cells," J. Appl. Phys., vol. 93, pp. 3693-3723, 2003.

[46] S. R. Scully and M. D. McGehee, "Effects of optical interference and energy transfer on exciton diffusion length measurements in organic semiconductors," J. Appl. Phys., vol. 100, pp. 034907, 2006.

[47] D. Yokoyama, A. Sakaguchi, M. Suzuki and C. Adachi, "Horizontal orientation of linear-shaped organic molecules having bulky substituents in neat and doped vacuum-deposited amorphous films," Org. Electron., vol. 10, pp. 127-137, 2009.

[48] B. Valeur and M. N. Berberan-Santos, Molecular Fluorescence: Principles and Applications. John Wiley & Sons, 2012.

[49] S. M. Menke and R. J. Holmes, "Exciton diffusion in organic photovoltaic cells," Energy Environ. Sci., vol. 7, pp. 499-512, 2014.

Chapter 6
Conclusion

This thesis provides an answer of the following question: is that the only way to develop next generation OLEDs through improvement of organic molecules or the architecture? I proposed an OLEDs system technology based on the NEMS/MEMS concept of modulating mechanical and electrical characteristics by fine structuring. The proposed technologies improve the properties of OLED systems property, even if we applied same organic molecules or the architecture previously used.

Summary of Contributions

The contributions of this research are summarized as follows:

[Chapter 2]

A key strategy to fabricate fine nanostructures via UV-NIL was developed. By combining UV-NIL with silicon anisotropic etching, the fabricated pattern size was decreased from that of the original mold. Thus, the final pattern size does not depend on that of the original imprint mold in the developed method. Our method does not require with a specific object size.

[Chapter 3]

Bridged glass nanopillar structures with high scratch resistance were developed. We established a method to dramatically improve the mechanical properties of glass nanopillars by considering stress distribution and optimizing submicron structure. The fabricated glass substrates with bridged glass nanopillars displayed self-cleaning ability while maintaining the durability of the underlying glass substrate.

[Chapter 4]

Highly flexible transparent ITO electrodes were fabricated for use in flexible

OLEDs. The developed strategy is different from that of previously reported flexible electrodes. The developed approach can increase the flexibility of not only ITO but also other rigid materials using a mesh structure.

[Chapter 5]

We developed a methodology to suppress EQE roll-off caused by SPA using a nanopatterned mask layer on an ITO electrode. The cold development method enabled nanopatterning of a thin resist layer on ITO. The theoretical model considering exciton diffusion direction readily explained the interaction between polaron and excitons in the OLEDs. By considering exciton diffusion direction, we were able to establish exciton control through nanostructure engineering.

Broader Impact

The research in this thesis has more than only direct impact. The durable self-cleaning glass with bridged glass nanopillars can be used in other types of displays as well as OLEDs. In addition, because the self-cleaning glass does not require solar power, it can be used indoors, such as in show cases and windows. The most important advantage of the mesh-patterned flexible ITO developed here is that we do not need to consider the compatibility between flexible electrodes and OLED structure, because the ITO electrode, which is the most common electrode in the rigid OLEDs, can be used directly in flexible OLEDs. Nano-OLEDs are potentially applicable as TADF OLEDs, which are currently being paid the most attention by OLED researchers. The roll-off of TADF caused by TTA may be suppressed by controlling the triplet exciton density using a nanopatterned mask layer.

Looking forward

We proposed and developed OLED system technology based on NEMS/MEMS in the work of this thesis. While our developed system can lead to great improvements in the OLED field, the presented system exhibits some limitations that would be interesting to explore in the future. We discuss the

limitations of our OLED system and propose future research directions in this section.

Fabrication method (Chapter 2): In Chapter 2, we fabricated 32-nm patterns using the developed method, although the required pattern resolution for NGL has reached less than ten nanometers. Optimization of the process conditions, such as milling time, wet etching quality, and thickness of Al_2O_3 deposited by ALD, should enable pattern resolution to be further increased. Moreover, the proposed process is not cost effective. However, the structure fabricated using the developed method is also applicable as a new fine nanomold after removing the metal.

Optical properties (Chapter 3 and 4): The bridged glass nanopillars and mesh-patterned ITO have promising mechanical properties. However, the optical properties of these materials, such as interference colors, and transmittances, have not yet been thoroughly studied. Optical simulation of these structures should lead to development of further functionalized structures.

Lasing (Chapter 5): The nano-OLEDs are still not to be able to realize lasing because there are some issues that need to be solved, including the remaining roll-off and insufficient current density. The remaining roll-off suggests that SPA still occurred; however, nano-OLEDs with smaller patterns did not work because the organic layer cannot fill the nanopattern. We expect that nano-OLEDs with organic single-crystal films, which have a longer exciton diffusion length than that of the presented emitting layer (BSB-Cz) used in nano-OLEDs, should help to suppress the remaining roll-off. In addition, we plan to develop OLEDs with heat management using the same idea as that of the nano-OLEDs. That is, nanopatterned layers are expected to allow the generated Joule heat to diffuse away from the organic layers in accordance with the thermal conductivity of the surrounding areas.

It is believed that demand for OLEDs will be accelerated in the coming internet of things society. This thesis presented studies that aimed to improve OLED performance from multiple directions. Highly functionalized OLED systems with NEMS/MEMS fine structure should become a fundamental technology for not only next-generation OLEDs, but also all organic electronics fields.

List of achievements

Related to the thesis

Journal papers, refereed

[1] Naofumi. Kobayashi[1], Hiroyuki Kuwae[1], Juro Oshima, Ryoichi Ishimatsu, Shuya Tashiro, Toshihiko Imato, Chihaya Adachi, Shuichi Shoji, Jun Mizuno, "A Wide-Energy-Gap Naphthalene-Based Liquid Organic Semiconductor Host for Liquid Deep-Blue Organic Light-Emitting Diodes", Journal of Luminescence, vol. 200, 19-23, 2018.
([1]These authors contributed equally to this article.)

[2] Kousuke Sakamoto[1], Hiroyuki Kuwae[1], Naofumi Kobayashi, Atsuki Nobori, Shuichi Shoji, Jun Mizuno, "Highly flexible transparent electrodes based on mesh-patterned rigid indium tin oxide", Scientific Reports, vol. 8, 2825, 2018.
([1]These authors contributed equally to this article.)

[3] Takumi Kamibayashi, Hiroyuki Kuwae, Shuichi Shoji, and Jun Mizuno, "Fabrication of Hole-Patterned Self-Standing Curved Film Using Large-area Spherical Soft UV Imprint Lithography", Transactions of The Japan Institute of Electronics Packaging, vol. 10, E17-002-1-E17-002-6, 2017.

[4] Takashi Kasahara, Hiroyuki Kuwae, Naofumi Kobayashi, Atsuki Nobori, Juro Oshima, Jun Mizuno, "Recent advances in research and development of microfluidic organic light-emitting devices", J. Photopolym. Sci. Technol., vol. 30, 467-474, 2017.

[5] Takeshi Komino, Hiroyuki Kuwae, Akiko Okada, Weixin Fu, Jun Mizuno, Jean-Charles Ribierre, Yuji Oki, Chihaya Adachi, "In-plane anisotropic molecular orientation of pentafluorene and its application to linearly polarized electroluminescence", ACS Applied Materials & Interfaces, vol. 9, 27054–27061, 2017.

[6] Kou Yoshida, Toshinori Matsushima, Yu Shiihara, Hiroyuki Kuwae, Shuichi Shoji, Jun Mizuno, Chihaya Adachi, "Joule heat-induced breakdown of organic thin-film devices under pulse operation", Journal of Applied Physics, vol. 121,

1995503, 2017.

[7] 桑江 博之, 須藤 健成, 岡田 愛姫子, 高山 公介, 庄子 習一, 水野 潤, “橋架け構造により高い擦り耐性を実現するガラスナノピラーの作製”, 電気学会論文誌E(センサ・マイクロマシン部門誌), vol. 137, 72-77, 2017.

[8] Hiroyuki Kuwae, Akiko Okada, Shuichi Shoji, Jun Mizuno, “Sub-50-nm structure patterning by combining nanoimprint lithography and anisotropic wet etching without considering original mold resolution”, Microelectronic Engineering, vol. 169, 39-42, 2017.

[9] Hiroyuki Kuwae, Atsushi Nitta, Kou Yoshida, Takashi Kasahara, Toshinori Matsushima, Munetomo Inoue, Shuichi Shoji, Jun Mizuno, Chihaya Adachi, “Suppression of external quantum efficiency roll-off of nanopatterned organic-light emitting diodes at high current densities”, Journal of Applied Physics, vol. 118, 15501, 2015.

Conference, refereed

[1] Hiroyuki Kuwae, Kazuaki Mizokami, Seren Maeda, Shuichi Shoji, Jun Mizuno, “Preparation and charterization of high performance activated carbon fibers by vaccum ultaraviolet surface treatment”, The 2017 MRS Fall Meeting & Exhibits, Boston, USA, December 2017.

[2] Hiroyuki Kuwae, Takenari Sudo, Kousuke Takayama, Shuichi Shoji, Jun Mizuno, “Fabrication of Mechanical Durable Glass Nanopillar with Bridged Structure”, International Conference on Solid State Devices and Materials (SSDM) 2017, Sendai, Japan, September 2017.

[3] Hiroyuki Kuwae, Shuichi Shoji, Jun Mizuno, “Suppression of external quantum efficiency roll-off of nanopatterned organic-light emitting diodes at high current densities”, Research and Education Consortium for Innovation of Advanced Integrated Science (CIAiS) 2017, Tokyo, Japan, February 2017.

[4] Hiroyuki Kuwae, Atsushi Nitta, Takashi Kasahara, Kou Yoshida, Shuichi Shoji, Chihaya Adachi, Jun Mizuno, “Nano-structured organic light emitting diode for suppression of roll-off characteristics toward electrically-pumped organic

semiconductor laser diodes", The 2015 International Chemical Congress of Pacific Basin Societies (Pacifichem), Honolulu Hawaii, USA, December 2015. (Student Poster Competition Finalists)

[5] 桑江博之、新田篤志、笠原崇史、吉田功、庄子習一、 安達千波矢、水野潤、"電流励起有機半導体レーザー光源に向けた高電流密度・高発光効率同時実現のためのNano-OLEDsの作製"、第32回「センサ・マイクロマシンと応用システム」シンポジウム、新潟、2015年10月.

[6] Hiroyuki Kuwae, Takashi Kasahara, Tsubasa Funabashi, Masao Kitajima, Kazuaki Mizokami, Shuichi Shoji, Jun. Mizuno, "Effects of Surface Modification on Lignocellulosic Porous Carbon Pellets by Vacuum Ultraviolet Treatment ", The 7th International Conference on Green and Sustainable Chemistry (GSC-7), Tokyo, Japan, July 2015.

[7] 桑江博之、岡田愛姫子、笠原崇史、庄子習一、水野潤、"UV ナノインプリントと異方性ウェットエッチングの組み合わせによるナノスケール極微細構造の作製"、第31回「センサ・マイクロマシンと応用システム」シンポジウム、松江、2014年10月.

[8] Hiroyuki Kuwae, Jun Mizuno, Akiko Okada, Shuichi Shoji, "Fine Nanoscale Structure Fabrication Using Combination of UV-Nanoimprint Lithography and Anisotropic Wet Etching Toward Single Nanoscale Interconnects", The 26th International Microprocesses and Nanotechnology Conference (MNC) 2013, Sapporo, Japan, November 2013.

[9] Kosuke Sakamoto, Hiroyuki Kuwae, Naofumi Kobayashi, Atsuki Nobori, Juro Oshima, Chihaya Adachi, Shuichi Shoji, Jun Mizuno, "Luminance Degradation and Recovery of Liquid Organic Semiconductor", The 2017 MRS Fall Meeting & Exhibits, Boston, USA, December 2017.

[10] Atsuki Nobori, Hiroyuki Kuwae, Naofumi Kobayashi, Takashi Kasahara, Juro Oshima, Shuichi Shoji, Jun Mizuno, "Free-Formable Microfluidic Organic Light Emitting Diode Ribbons Using Liquid Organic Semiconductors", 2nd International Symposium on Creation of Life Innovation Materials for Interdisciplinary and International Researcher Development (iLIM-2), Nagoya, Japan, September 2017.

[11] Kosuke Sakamoto, Hiroyuki Kuwae, Naofumi Kobayashi, Atsuki Nobori, Shuichi Shoji, Jun Mizuno, "Highly Bendable Transparent Electrode Using Mesh Patterned Indium Tin Oxide for Flexible Electronic Devices", The 12th Annual IEEE International Conference on Nano/Micro Engineered and Molecular Systemslectro (NEMS 2017), Los Angeles, USA, April 2017.

[12] Naofumi Kobayashi, Hiroyuki Kuwae, Juro Oshima, Ryoichi Ishimatsu, Shuya Tashiro, Toshihiko Imato, Chihaya Adachi, Shuichi Shoji, Jun Mizuno, "Deep-blue light emission with a wide-bandgap naphthalene-derivative liquid organic semiconductor host", SPIE Photonics West 2017, San Francisco, USA, January 2017.

[13] Kenichi Atsumi, Hiroyuki Kuwae, Yu Shihara, Atsuki Nobori, Chihaya Adachi, Shuichi Shoji, Jun Mizuno, "OLEDs with ultra-high thermal conductivity substrate", The 8th Asian Conference on Organic Electronics (A-COE) 2016, Kyoto, Japan, December 2016.

[14] Atsuki Nobori, Naofumi Kobayashi, Hiroyuki Kuwae, Takashi Kasahara, Juro Oshima, Chihaya Adachi, Shuichi Shoji, Jun Mizuno, "Flexible Organic Light Emitting Diode Ribbons Using Three Liquid Organic Semiconductors", The 11th Annual IEEE International Conference on Nano/Micro Engineered and Molecular Systemslectro (NEMS 2016), Matsushima Bay and Sendai, Japan, April 2016.

[15] Takenari Sudo, Jun Mizuno, Shuichi Shoji, Takashi Kasahara, Akiko Okada, Hiroyuki Kuwae, Kousuke Takayama, Yuriko Kaida, "Fabrication of Superhydrophilic Silica Nanostructure Using Simple Photolithography And Dry Etching For Self-Cleaning Glass", The 7th Asia-Pacific Conference on Transducers and Micro/Nano Technologies (APCOT), Daegu, Korea, June 2014.

Conference, invited

[1] Hiroyuki Kuwae, Kazuaki Mizokami, Seren Maeda, Shuichi Shoji, Jun Mizuno, "Effects of surface modification on woody carbon materials by vacuum ultraviolet treatment", 2017 Taiwan-Japan Workshop on Electronic

Interconnection I, Taipei, Taiwan, October 2017, invited. (Best Oral Presentation Award)

[2] Takashi Kasahara, Hiroyuki Kuwae, Naofumi Kobayashi, Atsuki Nobori, Juro Oshima, Shuichi Shoji, Jun Mizuno, "Recent advances in research and development of microfluidic organic light-emitting devices", The 34th International Conference of Photopolymer Science and Technology (ICPST-34), Chiba, Japan, June 2017.

[3] 笠原崇史、小林直史、江面知彦、石松亮一、大島寿郎、津脇美帆、桑江博之、今任稔彦、庄子習一、安達千波矢、水野潤, "マイクロ流体技術のマルチカラー有機発光デバイスへの応用", 第 63 回応用物理学会春季学術講演会、東京、2016 年 3 月.

[4] 安達千波矢、水野潤、笠原崇史、小林直史、桑江博之、庄子習一、"マイクロ流体有機 EL の作製と電界 発光特性"、第 14 回ナノテクノロジー総合シンポジウム(JAPAN NANO 2016)、東京、2016 年 1 月.

Patent

[1] 特願 2018-096756, 塩澤茉由子, 桑江博之、水野潤、魚島勝美、秋葉陽介、「骨成長の促進特性を有する生体埋植材及びその製造方法」

[2] 特願 2017-076016, 水野潤, 庄子習一, 坂本暁祐, 桑江博之,「フレキシブル透明電極及び有機エレクトロルミネッセンス素子」

[3] 特開 2015-179669, 林恭平, 安達千波矢, 井上棟智, 吉田功, 新田篤志, 桑江博之, 水野潤, 笠原崇史,「有機発光素子」

Book

[1] 桑江博之、水野潤、"ナノインプリント技術の動向"、月刊トライボロジー、2017 年 1 月号、pp.24-27.

[2] 安達千波矢、水野潤、笠原崇史、小林直史、桑江博之、庄子習一、"マイクロ流体有機 EL の作製と電界 発光特性"、NanotechJapan Bulletin, Vol.9, No.4, 2016.

Award

[1] 基幹理工学部 学部長賞 最優秀賞, 早稲田大学, 2014.

[2] 電子物理システム学科　優秀賞, 早稲田大学, 2014.

[3] ナノ理工学専攻 学生代表, 早稲田大学, 2016.

[4] 平成 27 年度秀でた利用 6 大成果,ナノテクノロジープラットフォーム.

[5] Best Oral Presentation Award, 2017 Taiwan-Japan Workshop on Electronic Interconnection I, Taipei Taiwan, October 24, 2017.

[6] 若手研究者奨励賞, 早稲田大学アーリーバードプログラム.

Not related to the thesis

Journal papers, refereed

[1] Weixin Fu, Bo Ma, Hiroyuki Kuwae, Shuichi Shoji, Jun Mizuno, "Low-temperature poly(oxymethylene) direct bonding via self-assembled monolayer", Japanese Journal of Applied Physics, vol. 57, 02BB01, 2017.

[2] Hirokazu Noma, Takumi Kamibayashi, Hiroyuki Kuwae, Naoya Suzuki, Toshihisa Nonaka, Shuichi Shoji, and Jun Mizuno, "Au intermediate layer to compensate surface roughness in Cu direct bonding process", Journal of Electronic Materials, published online, 2018.

International conference, refereed

[1] Ayako Suzuki, Hiroko Kato, Takahiro Kawakami, Yoshihiro Kodama, Mayuko Shiozawa, Emi Hoshikawa, Kenta Haga, Aki Shiomi, Atsushi Uenoyama, Issei Saito, Haruaki Hayasaki, Hiroyuki Kuwae, Keito Miwa, Jun Mizuno, and Kenji Izumi, "Development of a Micropatterned Fish Scale Collagen Scaffold to Manufacture a Tissue-Engineered Oral Mucosa", 5th Tissue Engineering and Regenerative Medicine International Society (TERMIS) World Congress-2018, Kyoto, Japan, September 2018, accepted.

[2] Keito Miwa, Hiroyuki Kuwae, Kouske Sakamoto, Shuichi Shoji, Jun Mizuno, "Fabrication of Microchannel-TEM Grid for in Situ Liquid TEM Observation of Interfacial Chemical Reaction", 2018 International Conference on Electronics Packaging and iMAPS All Asia Conference (ICEP-IAAC2018), 2018.04.17-21, Kuwana, Japan, April 2018.

[3] Mayuko Shiozawa, Yosuke Akiba, Katsumi Uoshima, Kaori Eguchi, Hiroyuki Kuwae, Weixin Fu, Shuichi Shoji, Jun Mizuno, "Promoting Proliferation and Elongation of Bone Marrow-Derived Stem Cells via Nano-Grain Deposited Periodic Nanostructures", 2017 MRS Fall Meeting, Boston, USA, November, 2017.

[4] Seren Maeda, Hiroyuki Kuwae, Shuichi Shoji, Jun Mizuno, "Effects of Surface Modification on Lignocellulosic Porous Carbon Materials by Vacuum Ultraviolet Treatment", 2nd International Symposium on Creation of Life Innovation Materials for Interdisciplinary and International Researcher Development (iLIM-2), Nagoya, Japan, September 2017.

[5] Weixin Fu, Bo Ma, Hiroyuki Kuwae, Shuichi Shoji, Jun Mizuno, "A study on low temperature SAM modified POM direct bonding affected by VUV/O3 irradiation", 2017 5th International Workshop on Low Temperature Bonding for 3D Integration (LTB-3D), Tokyo, Japan, May 2017.

[6] Hirokazu Noma, Takumi Kamibayashi, Hiroyuki Kuwae, Naoya Suzuki, Toshihisa Nonaka, Shuichi Shoji, Jun Mizuno, "Cu-Cu direct bonding by introducing Au intermediate layer", 2017 5th International Workshop on Low Temperature Bonding for 3D Integration (LTB-3D), Tokyo, Japan, May 2017.

[7] Takumi Kamibayashi, Hiroyuki Kuwae, Atsuki Nobori, Shuichi Shoji, Jun Mizuno, "Fabrication of Self-standing Curved Film with Pillar Arrays by Large Area Spherical Soft-UV Imprint Lithography", International Conference on Electronics Packaging (ICEP) 2017, Yamagata, Japan, April 2017.

[8] Weixin Fu, Hiroyuki Kuwae, Bo Ma, Shuichi Shoji, Jun Mizuno, "Low Temperature Direct Bonding of Polyoxymethylene (POM) Through Self Assembled Monolayers (SAM)", International Conference on Electronics Packaging (ICEP) 2017, Yamagata, Japan, April 2017.

[9] Haruka Suzaki, Hiroyuki Kuwae, Akiko Okada, Bo Ma, Shuichi Shoji, Jun Mizuno, "Study of LiTaO3/ST-quartz Bonding with Amorphous Interlayer Assisted by VUV/O3 Treatment for SAW Device", 2016 International

Microsystems, Packaging, Assembly and Circuits Technology Conference (iMPACT), Taipei, Taiwan, October 2016.

[10] Bingyang Xu, Hiroyuki Kuwae, Tomohiro Edura, Hidehito Adaniya, Masao Yamashita, Tsumoru Shintake, Shuichi Shoji, Jun Mizuno, "Fabrication of Conductive Diamond Membrane for Functional TEM Grids using Two-step Dry Etching", Asia-Pacific Conference of Transducers and Micro-Nano Technology (APCOT) 2016, Kanazawa, Japan, June 2016.

[11] Haruka Suzaki, Hiroyuki Kuwae, Akiko Okada, Bo Ma, Shuichi Shoji, and Jun Mizuno, "ST-quartz/LiTaO3 Direct Bonding Using SiO2 Amorphous Layers with VUV/O3 Pre-treatment for a Novel 5G Surface Acoustic Wave Device", International Conference on Electronics Packaging (ICEP) 2016, Sapporo, Japan, April 2016.

[12] Bo Ma, Hiroyuki Kuwae, Akiko Okada, Weixin Fu, Shuichi Shoji, and Jun Mizuno, "VUV/O3 assisted single-crystal quartz bonding with amorphous SiO2 intermediated layers for manufacturing optical low pass filter", International Conference on Electronics Packaging (ICEP) 2016, Sapporo, Japan, April 2016.

[13] Bo Ma, Hiroyuki Kuwae, Akiko Okada, Weixin Fu, Shuichi Shoji, Jun. Mizuno, " Low temperature direct bonding of single crystal quartz substrates for high performance optical low pass filter using amorphous SiO2 intermediate layers" The 29th IEEE International Conference on Micro Electro Mechanical Systems (MEMS 2016), Shanghai, China, January 2016.

[14] Sayoko Yamada, Shotaro Ohno, Koji Fukuda, Hiroyuki Kuwae, Jun Mizuno, Yuichi Matsushima, Hiroshi Ishikawa Katsuyuki Utaka, "Fabrication and nonlinear optical property of SWCNT-embedded Si slot waveguide for ultra-fast photonic functional devices", The 7th International Symposium on Ultrafast Photonic Technologies and International Symposium on extremely advanced transmission technology (ISUPT/EXAT 2015), Kyoto, Japan, July 2015.

[15] Jun Mizuno, Hiroyuki Kuwae, Takashi Kasahara, Shuichi Shoji, "Vapor Absorption of Lignocellulosic Porous Carbon Pellets and Effects of Vacuum

Ultraviolet Treatment", The 6th International Symposium on Advanced Materials Development and Integration of Novel Structural Metallic and Inorganic Materials (AMDI-6), Tokyo, Japan, June 2015.

[16] Kouji Fukuda, Sayoko Yamada, Hiroyuki Kuwae, Jun Mizuno, Tadashi Takashima, Yuichi Matsushima, Katsuyuki Utaka, "Nonlinear optical property of CNT embedded in Si slot waveguide", The OptoElectronics and Communication Conference and Australian Conference on Optical Fibre Technology (OECC/ACOFT) 2014, Melbourne, Australia, July 2014.

Domestic conference, refereed

[1] 登惇輝、桑江博之、小林直史、笠原崇史、大島寿郎、庄子習一、水野潤、「液体有機半導体を用いたフレキシブルマイクロ流体有機ELリボン」、第24回「エレクトロニクスにおけるマイクロ接合・実装技術」シンポジウム(Mate 2018)、横浜、2018 年 1 月.

[2] 須崎遥、桑江博之、岸田和人、垣尾省司、庄子習一、水野潤、「非晶質層を用いたLiTa03/QZ 接合 SAW 基板の作製」、第24回「エレクトロニクスにおけるマイクロ接合・実装技術」シンポジウム(Mate 2018)、横浜、2018 年 1 月.

[3] Bingyang Xu, Hiroyuki Kuwae, Shuichi Shoji, Jun Mizuno, "Fabrication of Diamond-Based Transmission Electron Microscopy Grid for High-Resolution Bio-Sample Observation"、 第24回「エレクトロニクスにおけるマイクロ接合・実装技術」シンポジウム(Mate 2018)、横浜、2018 年 1 月.

[4] 坂本暁祐、桑江博之、小林直史、登厚惇輝、庄子習一、水野潤、「フレキシブルエレクトロニクスデバイスへ向けたメッシュパターンを有するフレキシブル酸化インジウムスズ電極」、第34回「センサ・マイクロマシンと応用システム」シンポジウム、広島、2017 年 10 月.

[5] 前田世蓮、桑江博之、庄子習一、水野潤、「高機能木質系炭素材料に向けた真空紫外光表面処理における酸素分圧の影響」、第34回「センサ・マイクロマシンと応用システム」シンポジウム、広島、2017 年 10 月.

[6] 小簑剛、桑江博之、岡田愛姫子、付偉欣、水野潤、Jean-Charles Ribierre、興雄司、安達千波矢、"スピンコート法によるゲスト分子の面内配向制御"、第 11 回分子科学討論会 2017、仙台、2017 年 9 月.

[7] 金田達志、桑江博之、庄子習一、安達千波矢、水野潤、”低分子有機半導体接合を用いた新規有機 EL 作製技術”、第 23 回「エレクトロニクスにおけるマイクロ接合・実装技術」シンポジウム(Mate 2017)、横浜、2017 年 2 月.

[8] 須藤健成、岡田愛姫子、桑江博之、高山公介、庄子習一、水野潤、”橋掛け構造により高い擦り耐性を実現するガラスナノピラー構造の作製”、第 22 回「エレクトロニクスにおけるマイクロ接合・実装技術」シンポジウム (Mate 2016)、横浜、2016 年 2 月.

[9] 須藤健成、桑江博之、岡田愛姫子、笠原崇史、水野潤、 庄子習一、 高山公介、 海田由里子、”金属薄膜を用いた異種材料同時エッチングによる極微細ガラス構造の作製手法”、第 32 回「センサ・マイクロマシンと応用システム」シンポジウム、新潟、2015 年 10 月.

Conference, non-refereed

[1] 林純貴、山谷浩、浅川詩織 、鈴木雅視 、垣尾省司 、桑江博之 、米内敏文、岸田和人、水野 潤、“LiNbO3・LiTaO3 薄板と水晶基板の接合による縦型リーキー弾性表面波の低損失化”、第 47 回 EM シンポジウム、東京、2018 年 6 月.

[2] Akari Otsuka, Hiroyuki Kuwae, Kosuke Sakamoto, Miho Suzuki, Shuichi Shoji, Jun Mizuno, “Fundamental Research for Portable On-Demand Fluorescence Detection System”, 2018 Japan-Taiwan Workshop on Electronic Interconnection II, Kuwana, Japan, April 2018.

[3] Takumi Kamibayashi, Hiroyuki Kuwae, Shuichi Shoji, Jun Mizuno, “Fabrication of Self-Standing Curved Film with Pillar-Shaped Hole Patterns Using Large-Area Spherical Soft UV Imprint Lithography”, 2018 Japan-Taiwan Workshop on Electronic Interconnection II, Kuwana, Japan, April 2018.

[4] 水野潤、付偉欣、桑江博之、河合達志、庄子習一、” Polyoxymethylene (POM) low temperature direct bonding realized by self-assembled monolayer modification”、学際・国際的高度人材育成ライフイノベーションマテリアル創製共同研究プロジェクト(6大学連携プロジェクト)第2回公開討論会、名古屋、2018 年 3 月.

[5] 水野潤、上林拓海、桑江博之、庄子習一、” Fabrication of Self-Standing Curved Film with Hole Patterns using Spherical Soft UV Imprint Lithography”、学際・国際的高度人材育成ライフイノベーションマテリアル創製共同研究プロジェクト(6大

学連携プロジェクト）第2回公開討論会、名古屋、2018 年 3 月.

[6] 水野潤、金田達志、付偉欣、桑江博之、付偉欣、庄子習一、斎藤美紀子、西川宏、”真空紫外光によるダメージレス表面前処理を用いたナノポーラス金接合”、第 2 回 六大連携プロジェクト公開討論会、名古屋、2017 年 3 月.

[7] 水野潤、齋藤美紀子、付偉欣、桑江博之、庄子習一、金田達志、西川宏、”真空紫外光によるダメージレス表面前処理を用いたナノポーラス金接合”、学際・国際的高度人材育成ライフイノベーションマテリアル創製共同研究プロジェクト（6大学連携プロジェクト）第1回公開討論会、名古屋、2017 年 3 月.

[8] 水野潤、岡田愛姫子、付偉欣、桑江博之、庄子習一、” High quality 2-inch GaN template using nanometer-size SiO2 mask structure”、学際・国際的高度人材育成ライフイノベーションマテリアル創製共同研究プロジェクト（6大学連携プロジェクト）第1回公開討論会、名古屋、2017 年 3 月.

[9] 水野潤、岡田愛姫子、桑江博之、付偉欣、庄子習一、後藤博史、山口敦史、碓井彰、”High quality 2-inch GaN template using nanometer-size SiO2 mask structure fabricated by UV nanoimprint lithography”、第 2 回 六大連携プロジェクト公開討論会、名古屋、2017 年 3 月.

[10] 塩澤茉由子、桑江博之、庄子習一、水野潤、「MEMS テクノロジーによる次世代実装技術」、4大学ナノ・マイクロファブリケーションコンソーシアム シンポジウム、神奈川、2017 年 3 月.

[11] 小林直史、桑江博之、庄子習一、水野潤、”ディープブルー発光のためのワイドバンドギャップ液体有機半導体ホスト材料”、早稲田大学ナノテクノロジーフォーラム 第 2 回分科会ワークショップ、東京、2017 年 3 月.

[12] 新田篤志、桑江博之、吉田功、井上棟智、松島敏則、水野潤、安達千波矢、 “ナノ微細構造 OLED を用いた Singlet-Polaron Annihilation の抑制”、 第 62 回応用物理学会春季学術講演会、神奈川、2015 年 3 月.

[13] 山田佐代子、福田晃士、桑江博之、水野潤、高島正、大野翔太郎、松島裕一、石川浩、宇髙勝之、“CNT 含有シリコンスロット導波路の作製と非線形光学特性”、電子情報通信学会技術研究報告、レーザ・量子エレクトロニクス、大阪、2014 年 11 月.

Appendix
Wide-energy-gap liquid organic light-emitting diodes host

The topic of this chapter is not directly connected to the concept of this thesis, although it is an important achievement for future flexible OLEDs. Thus, I decided to add it in the appendix.

We developed a novel naphthalene derivative to function as a wide-energy-gap LOS host material for the limited range of liquid deep-blue light-emitting materials that have been developed to date. The naphthalene derivative 1-naphthaleneacetic acid 2-ethylhexyl ester (NLQ), which shows a low viscosity of 20 mPa·s at 25 °C, was synthesized as a LOS by introducing an ethylhexyl group into naphthalene. We doped 9,10-diphenylanthracene (DPA) into NLQ as a guest deep-blue dye. The highest occupied molecular orbital (HOMO) energy level of NLQ was estimated to be -6.40 eV from photoelectron spectroscopy measurements in air. The energy gap of NLQ was estimated to be 4.08 eV from its absorption spectrum, indicating that NLQ has the widest energy gap of any such host material to date. Deep-blue EL emission in a liquid state was obtained by doping DPA into NLQ. Light emission could be achieved by a combination of Förster resonance energy transfer (FRET) and direct recombination of trapped holes and electrons because the energy gap of DPA is straddled by the wider energy gap of NLQ.

The contents of this chapter have been published in the following journal article:

"A Wide-Energy-Gap Naphthalene-Based Liquid Organic Semiconductor Host for Liquid Deep-Blue Organic Light-Emitting Diodes", Journal of luminescence, vol. 200, pp. 19-23, 2018 [1].

A.1. Introduction

Since the first report of liquid OLEDs by Xu and Adachi in 2009, they have attracted much attention for truly flexible organic electronics applications [2]. Liquid OLEDs have a simple structure that consists of a luminescent LOS layer sandwiched between two transparent electrodes. LOSs show semiconducting behavior in a liquid state without any solvent at room temperature. The light-emitting LOS layer also keeps its liquid state when a driving voltage is applied. Liquid OLEDs have novel characteristics compared to conventional solid-state OLEDs, such as the LOS and electrodes remaining attached when the device is bent and restoration of degraded light emission by the ability to replace deteriorated emitter liquids [3]. Furthermore, multicolor EL can be obtained from liquid OLEDs based on Förster resonance energy transfer (FRET) [2,4] by doping a small amount of a guest solid emitter into a LOS host.

In terms of device structure, liquid OLEDs have been developed for display and lighting applications [3,5-9]. To pattern liquid emitters on a single chip, we proposed microfluidic OLEDs, which combine liquid OLEDs with microfluidic technology [4-8]. Using microfluidic technology, we have demonstrated recovery of emission by reinjecting fresh LOSs [6], multicolor emission by mixing different liquid emitters with a Y-shaped microchannel [7], and EL emission from liquid emitters patterned on rigid and flexible substrates [5,8]. We have also demonstrated white EL emission from an integrated microfluidic structure via the simultaneous emission of greenish-blue and yellow liquid emitters [9].

Deep-blue OLEDs require host materials with a wide energy gap [10]. The current lack of suitable wide-energy-gap hosts is a critical issue that needs to be overcome to expand liquid-OLED applications to full-color displays and light sources for medical treatment [11]. Deep-blue light can increase the color gamut [10,12] and lower power consumption in full-color applications [10]. The host/guest doping strategy is an important approach for this purpose. However, the availability of luminescent LOSs, especially wide-energy-gap hosts, is limited because liquid-OLED technology is still in an early stage of development [2]. The energy gaps of the LOSs

reported to date range from 3.2 to 3.5 eV [2,3,13]. Hirata [3] demonstrated deep-blue light emission using carbazole derivatives as wide-energy-gap LOSs, such as 9-{2-[2-(2-methoxyethoxy)ethoxy]ethyl}-9H-carbazole (energy gap = 3.5 eV) and 9,9′-{2-[2-(2-methoxyethoxy)ethoxy]ethyl}-3,3′-bis(9H-carbazole) (energy gap = 3.5 eV). In addition, there are some other blue emitting liquid molecules, although they were not observed in OLEDs devices [14-18]. To further develop liquid-OLED applications, it is essential to generate systems that display deep-blue light emission using wide-energy-gap LOSs. In addition, such wide-energy-gap host materials can be used not only as host materials for deep-blue deep blue emitters, but also as host materials for co-doping systems, which has been proposed to improve quantum efficiency of conventional fluorescence materials by cascade energy transfer from thermally activated delayed fluorescence materials [19].

In this study, we develop a naphthalene derivative as a novel wide-energy-gap LOS host material for deep-blue light emission. Our naphthalene derivative shows a low viscosity and a wide energy gap, as estimated from its UV-vis absorption edge. The PL spectrum of a guest deep-blue dye and the EL spectrum of the guest-doped naphthalene derivative indicate that deep-blue EL emission derived from the guest dye could be obtained by doping the guest into the LOS host material. Therefore, novel naphthalene-derivative LOSs are promising wide-energy-gap host materials for deep-blue light emission.

A.2. Experimental procedure

A.2.1 Materials

Figure A.1 shows the chemical structures of the wide-energy-gap LOS host and a solid deep-blue emitter guest. We synthesized NLQ by introducing an ethylhexyl group into a naphthalene unit to give a liquid at room temperature. The synthetic details and characterization of NLQ are presented in the Supplementary Information. Naphthalene was selected because of its intrinsic wide energy gap [20]. A mixture of 1-naphthaleneacetic acid (10.0 g, 53.7 mmol), 1-bromo-2-ethylhexane (20.7 g, 107.3mmol), potassium carbonate (22.2 g, 160.9 mmol), and DMF (100 mL)

was stirred for 4 h at 90 °C. After evaporation of the DMF under reduced pressure, chloroform (100 mL) was added to the crude product. The organic phase was washed with H_2O (3 × 100 mL), dried over $MgSO_4$, and filtered. Evaporation of the filtrate gave the crude product. The crude material was purified by column chromatography (silica gel, eluent = 20% volume fraction of chloroform in hexane) to give NLQ as a transparent liquid (12.5 g, 41.9 mmol, 78%). The products were unambiguously characterized by means of ^1H and ^{13}C spectroscopy (Fig. A.2 and A.3, respectively) and HRMS spectrometry. ^1H NMR (600 MHz, $CDCl_3$): δ = 8.00 (d, J = 6.0 Hz, 1H), 7.83 (d, J = 6.0 Hz, 1H), 7.75 (d, J = 9.0 Hz, 1H), 7.50 (t, J = 9.0 Hz, 1H), 7.45 (t, J = 7.5 Hz, 1H), 7.41-7.38 (m, 2H), 4.04 (s, 2H), 3.98 (d, J = 6.0 Hz, 2H), 1.47-1.43 (m, 1H), 1.24-1.09 (m, 8H), 0.80 (t, J = 9.0 Hz, 3H), 0.76 (t, J = 9.0 Hz, 3H). ^{13}C NMR (600 MHz, $CDCl_3$): δ = 171.6, 133.7, 132.0, 130.7, 128.6, 127.9, 126.2, 125.6, 125.3, 123.8, 67.1, 39.3, 38.6, 30.2, 28.7, 23.6, 22.8, 13.9, 10.8. HRMS (m/z) calculated for $C_{20}H_{26}O_2$ [M + Na]: 321.1825, found: 321.1825.

NLQ shows a low viscosity of 20 mPa·s at 25 °C, which was obtained by using cone-plate type viscometer (TVE-22L, TOKI SANGYO). The deep-blue dye 9,10-diphenylanthracene (DPA; Tokyo Chemical Industry Co., Ltd.) [20, 21] was doped into NLQ at a concentration of 2 wt%. To dope the dye into NLQ homogeneously, we first dissolved both NLQ and the dye into dichloromethane (CH_2Cl_2) solution, and mixed them well in a beaker [6]. Subsequently, in order to evaporate CH_2Cl_2, the sample solution was placed in a vacuum oven at 80 °C for 5 hours. Tributylmethylphosphonium bis(trifluoromethanesulfonyl)imide (Tokyo Chemical Industry Co., Ltd.) was used as an electrolyte and doped into the liquid emitter at a concentration of 0.25 wt% [5,6,8,9] to enhance carrier injection.

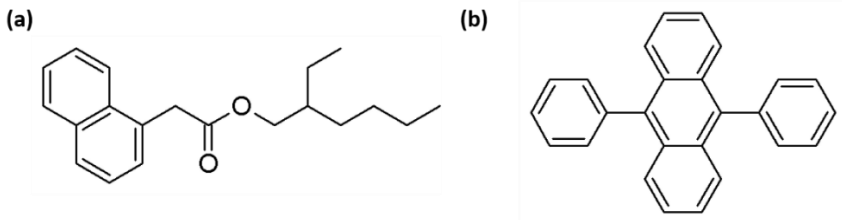

Figure A.1 Chemical structures of (a) the novel naphthalene-derivative NLQ and (b) DPA [1].

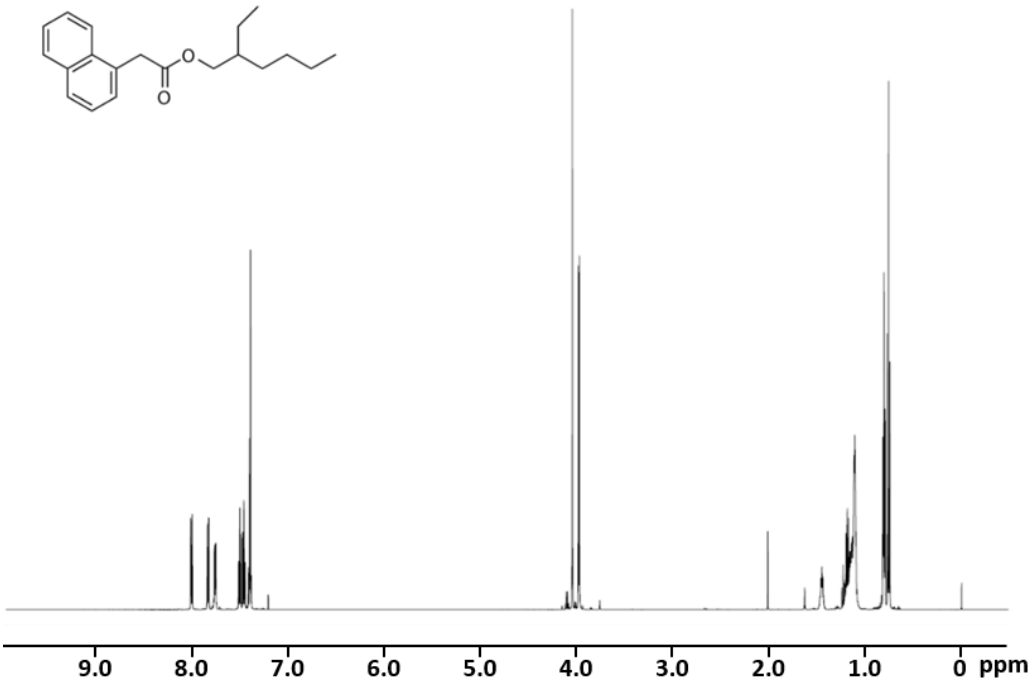

Figure A.2 ^{1}H NMR spectrum of NLQ [1].

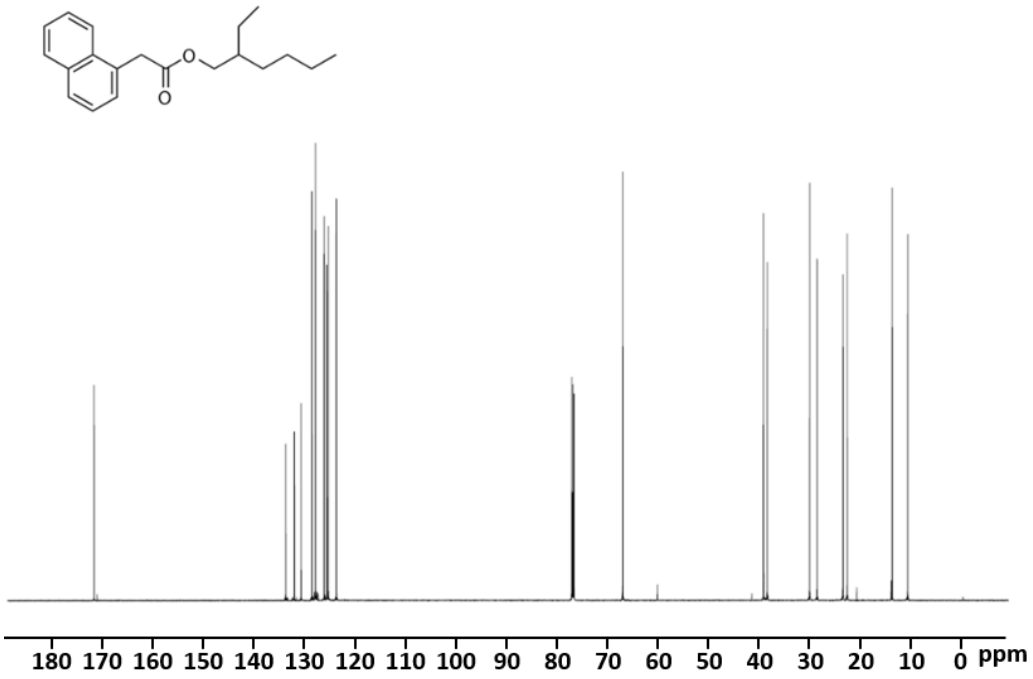

Figure A.3 ^{13}C NMR spectrum of NLQ [1].

A.2.2 Electrochemical properties

To evaluate the chemical stability of our new host, samples were measured by cyclic voltammetry (CV) with a three-electrode electrochemical cell in acetonitrile (MeCN). The device lifetime of a liquid-OLED can be influenced by the chemical stability of radical cations in the liquid emitting layer [3]. A Pt disk (diameter = 3 mm), and Pt and Ag wires were used as working, counter, and reference electrodes, respectively. The Pt disk electrode was polished with an alumina slurry (diameter = 50 nm) before the CV measurements. The applied voltage (E) was calibrated against the standard redox potential (E_0) of ferrocene ($Fc/Fc+$, 0.424 V vs. a saturated calomel electrode (SCE)). Solutions were deoxygenated by N_2 gas bubbling before the CV measurement, and measurements were performed under a N_2 atmosphere. The scan rate was 100 mV/s. The HOMO energy level of NLQ was estimated from the onset voltage of oxidation.

A.2.3 Photophysical properties

The HOMO energy level of NLQ was also estimated by photoemission spectroscopy (PES) in air (AC-3, Riken Keiki Co., Ltd.). Absorption spectra were measured with a UV-vis spectrophotometer (U-3900, Hitachi High-Technologies, Ltd.). PL spectra were measured with a fluorescence spectrophotometer (FP-6200, FP-8200, JASCO). Quartz cells were used for both absorption and PL spectroscopy. PLQY were estimated with an integrating sphere (Quantaurus QY, Hamamatsu Photonics K. K.). Solutions were deoxygenated by bubbling with N_2 gas before the PLQY measurements, which were performed under a N_2 atmosphere. The energy gap of NLQ was estimated from its UV-vis absorption edge. The LUMO energy level of NLQ was estimated by subtracting the energy gap from the HOMO energy level.

A.2.4 Electroluminescent properties

The EL characteristics of the liquid emitters were evaluated in microfluidic OLEDs [5]. The microfluidic OLEDs were fabricated as follows: (a) Anode and cathode substrates were fabricated by photolithography. (b) The two substrates were

bonded by forming epoxy–amine linkages between epoxy- and amine-terminated self-assembled monolayers. (c) A liquid light-emitting layer was formed by injecting liquid emitters into the microchannel of the fabricated microfluidic device. The thickness of the liquid emitting layer was about 6 μm. The active area of the microfluidic OLEDs was adjusted to be 1 × 2 mm^2. EL properties were measured using a source meter (2400, Keithley) with a direct-current power supply and a power meter (1936-R, Newport). EL spectra were measured with a spectrometer (USB4000FL, Ocean Optics).

A.3. Results and discussion

A.3.1 Electrochemical properties

The CV characteristics of 1 mM NLQ dissolved in MeCN are presented in Fig. A.4. An anodic wave was observed in the positive scan direction, which resulted in the generation of a radical cation on NLQ. However, this oxidation process was irreversible. In the negative scan direction, no cathodic wave was detected for NLQ because the reduction wave of NLQ was out of the polarized potential window of MeCN. The irreversibility of the oxidation process suggests that charge transfer may cause chemical changes in the oxidized molecule followed by further reactions [23-25], and also implies that the measured potential is a mix of ionization potential and the energy required for the possible chemical changes occurring during the charge transfer. The contribution of the chemical changes to the potential may be small enough to be ignored because the irreversible peak potential may correspond to within 100 mV of the reversible oxidation potential if the species generated by a reversible electron transfer process is consumed by further reactions [26,27]. The measured onset voltage of oxidation $E_{OX}{}^{onset}$ (vs. SCE) was 1.73 V. Thus, the HOMO energy level of NLQ was estimated to be -6.17 eV according to the empirical equation HOMO = -(4.44 eV + $E_{OX}{}^{onset}$) (vs. SCE) [28,29].

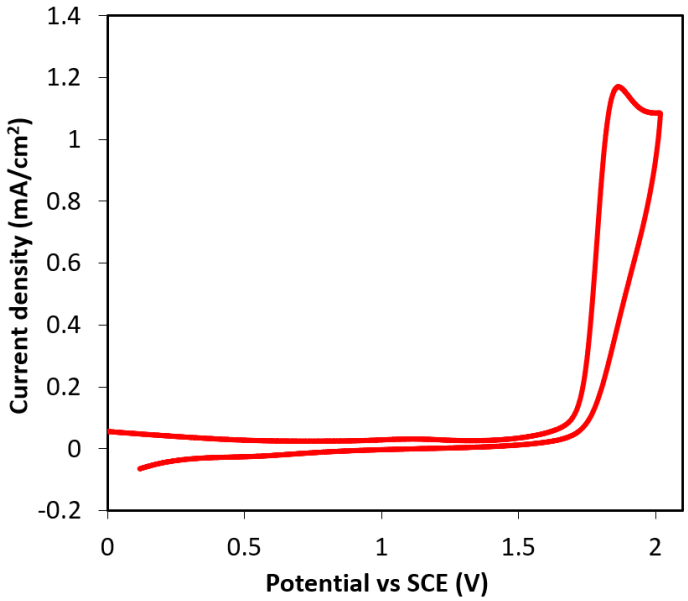

Figure A.4 Cyclic voltammogram of 1 mM NLQ in MeCN. An anodic wave was observed in the positive scan direction, while a cathodic wave was not observed in the negative scan direction, indicating that the oxidation process of NLQ is irreversible [1].

A.3.2 Photophysical properties

In addition to evaluating the HOMO energy level of NLQ from the CV measurements, we also estimated its HOMO energy level through PES. Fig. A.5 shows the PES results for neat NLQ. The HOMO energy level of NLQ estimated from PES data was -6.39 eV. This value is slightly different from that obtained from the CV measurements. Reversible CV characteristics are suitable to evaluate the HOMO energy level of a material. However, the cyclic voltammogram of NLQ was irreversible, which resulted in the underestimation of its HOMO energy level [26]. Therefore, we use the HOMO energy level determined from PES in the following discussion.

The UV-vis absorption spectrum and PL spectrum of NLQ are presented in Fig. A.6. The UV-vis absorption maximum of NLQ was located at 283 nm, while the UV-vis absorption edge of NLQ was at 304 nm. The energy gap of NLQ estimated from the absorption edge was 4.08 eV. Thus, NLQ shows the widest energy gap of any LOS to date [2,3,13]. This result suggests that the wide energy gap of NLQ can

be attributed to the short π-conjugation length of naphthalene [30]. The LUMO energy level of NLQ calculated by subtracting the energy gap from the HOMO energy level was -2.31 eV. The PL spectrum of NLQ obtained following excitation at 280 nm contained a peak with a maximum at 395 nm, which is close to UV position. These results indicate that NLQ is a promising host material that may enable excitation of guest materials that emit light at short wavelength.

The PL spectrum of 1 mM DPA dissolved in MeCN and the absorption spectrum of 5 μM DPA in MeCN are shown in Fig. A.7. There was spectral overlap between the PL spectrum of NLQ and the absorption spectrum of DPA. The maximum PL peak of DPA was located at 439 nm. The PLQY of 20 μM NLQ in MeCN was 18%, while that of 16 μM DPA in MeCN was 98%. Fig. A.8. also shows the PL spectrum of 2 wt% DPA-doped NLQ following 280-nm excitation and the PL spectrum of 1 mM DPA in MeCN. This result shows that PL emission originating from DPA was obtained by selectively exciting NLQ. Moreover, the maximum PL peak of NLQ at 395 nm was quenched in the mixture. These results suggest that FRET occurred from NLQ to DPA.

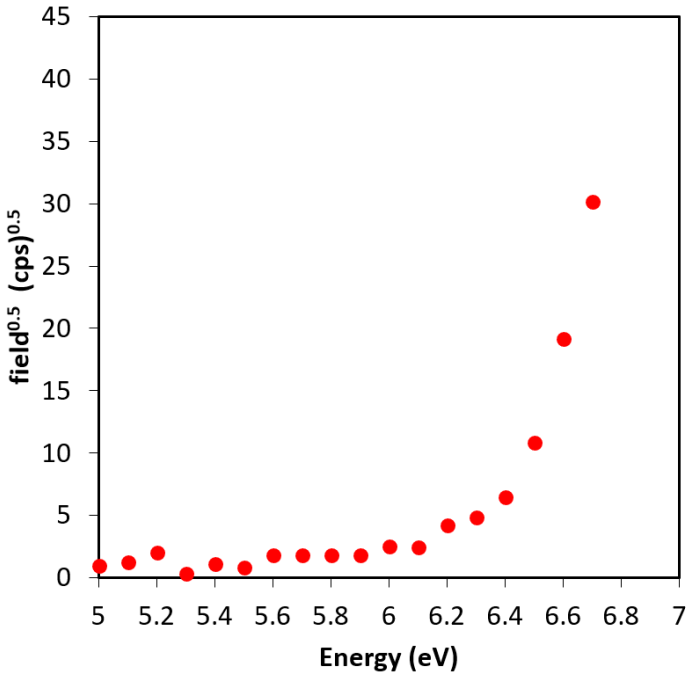

Figure A.5 Photoelectron spectrum of neat NLQ obtained in air [1].

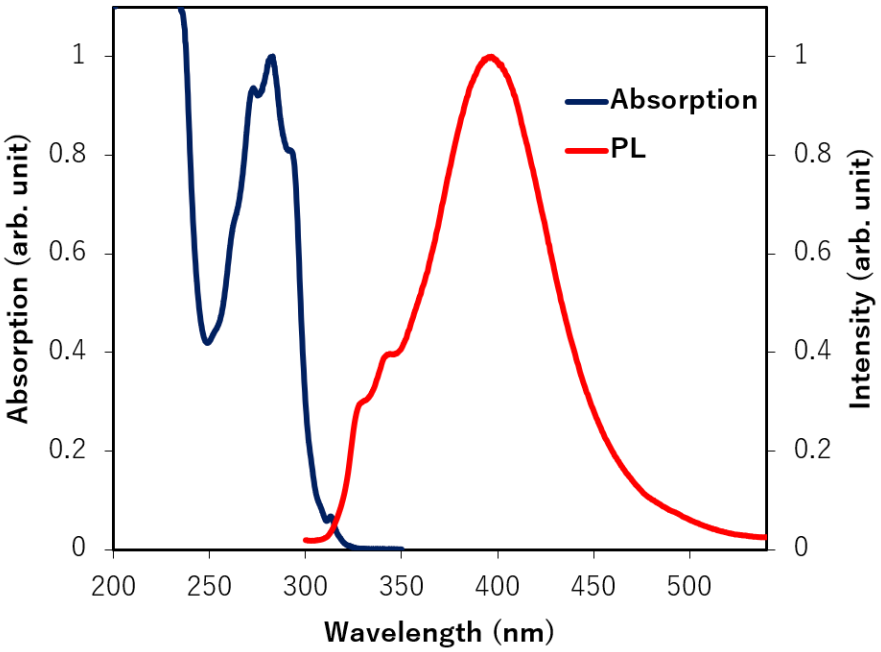

Figure A.6 Absorption spectrum and PL spectrum of NLQ [1].

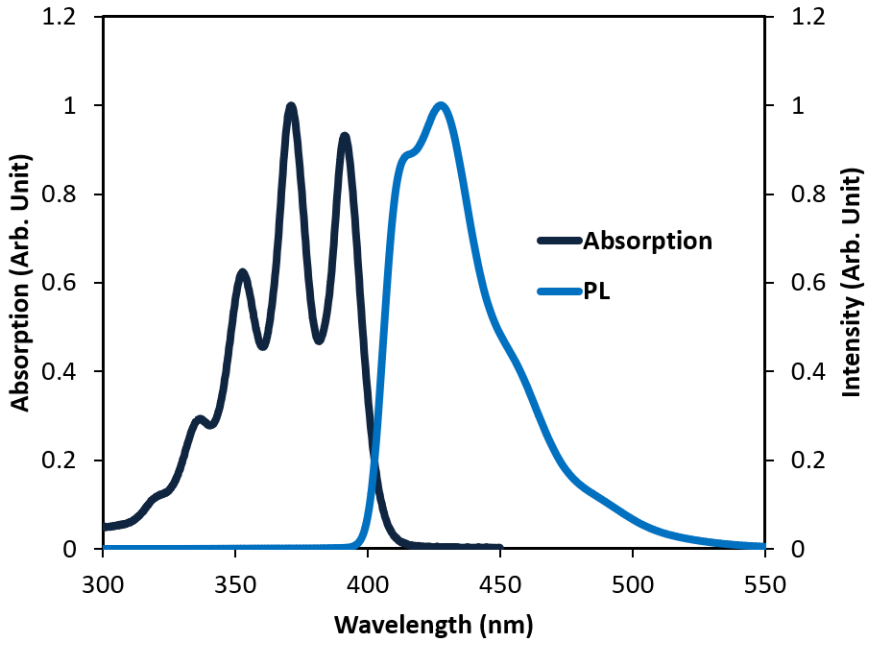

Figure A.7 PL spectrum of 1 mM DPA in MeCN and absorption spectrum of 10 μM DPA in MeCN [1].

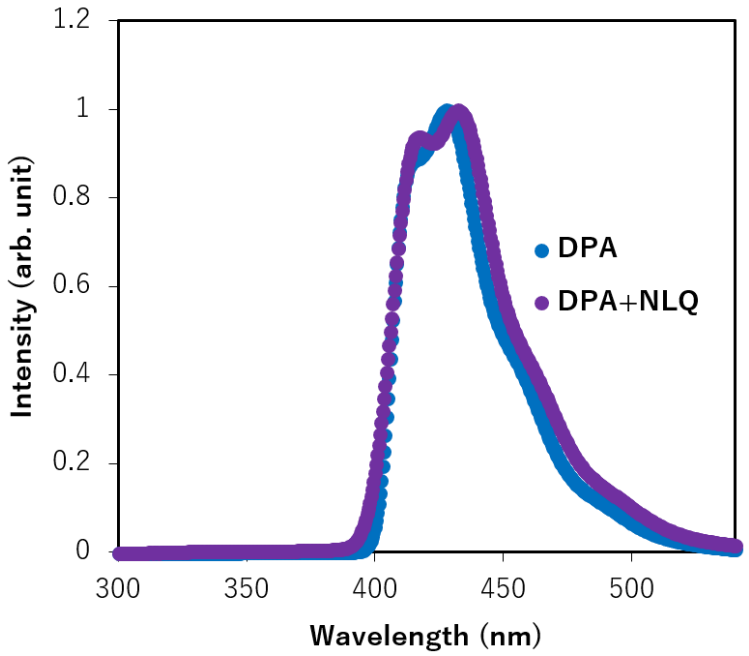

Figure A.8 PL spectrum of 2 wt% DPA-doped NLQ and PL spectrum of 1 mM DPA in MeCN. PL emission derived from DPA was obtained from the mixture of DPA and NLQ upon selectively exciting NLQ [1].

A.3.3 Electroluminescent properties

Directly evaluating the EL properties of neat NLQ was difficult because the peak from NLQ lies in the UV region. Fig. A.9 (a) and (b) show a luminescent image of the EL emission and EL spectrum, respectively, measured for a microfluidic OLED with 2 wt% DPA-doped NLQ at an applied voltage of 50 V. The EL spectrum of the DPA-doped NLQ was similar to the PL spectrum of DPA. This result indicates that deep-blue EL emission derived from DPA was enabled by the wide-energy-gap LOS host. The HOMO and LUMO energies and energy gap of DPA were -5.58, -2.56, and 3.02 eV, respectively, based on the absorption edge of the UV-Vis absorption spectrum of DPA and the onset oxidation voltage of its cyclic voltammogram. These values suggest that the energy gap of DPA is straddled by that of NLQ. Thus, deep-blue EL emission could be obtained not only by FRET but also by direct recombination of the trapped holes and electrons [31].

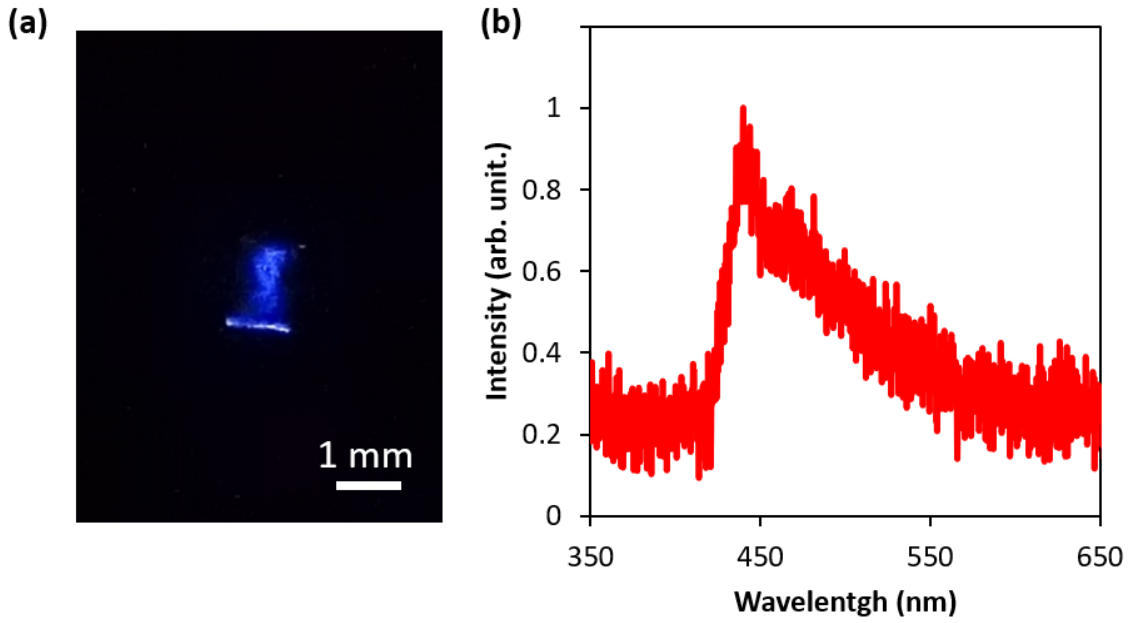

Figure A.9 (a) EL emission and (b) EL spectrum of 2 wt% DPA-doped NLQ in a microfluidic OLED device at an applied voltage of 50 V [1].

Figure A.10 (a) shows the current density (J)–voltage (V) characteristics of 2 wt% DPA-doped NLQ and neat NLQ and Fig. 8(b) displays the luminance (L)–V characteristics of 2 wt% DPA-doped NLQ. Stable carrier injection and transport were observed for both DPA-doped NLQ and neat NLQ because J increased in proportion to V. J of DPA-doped NLQ was higher than that of neat NLQ. This result indicates that carrier transport in the LOS was increased by doping with DPA. Moreover, the L-V characteristics revealed that L = 4.73 cd/m^2 at 50 V was achieved by doping DPA into NLQ. Meanwhile, electroluminescent properties of the DPA doped-NLQ was not much different from those of previously reported LOS systems [2,3,5-9,13], although it was inferior to electroluminescent properties of solid type OLEDs. Therefore, optimization of the devise structure will be required for further improvement.

These results indicate that NLQ is a promising wide-energy-gap LOS host material for deep-blue light emission in liquid-based display and lighting applications. Although we have demonstrated development of LOS materials for liquid-OLEDs, the driving voltage of these devices remains high and their L remains low compared to those of conventional solid-state OLEDs. Therefore, LOS host

materials that enable both a lower driving voltage and higher PLQY are required to further improve the performance of liquid OLEDs

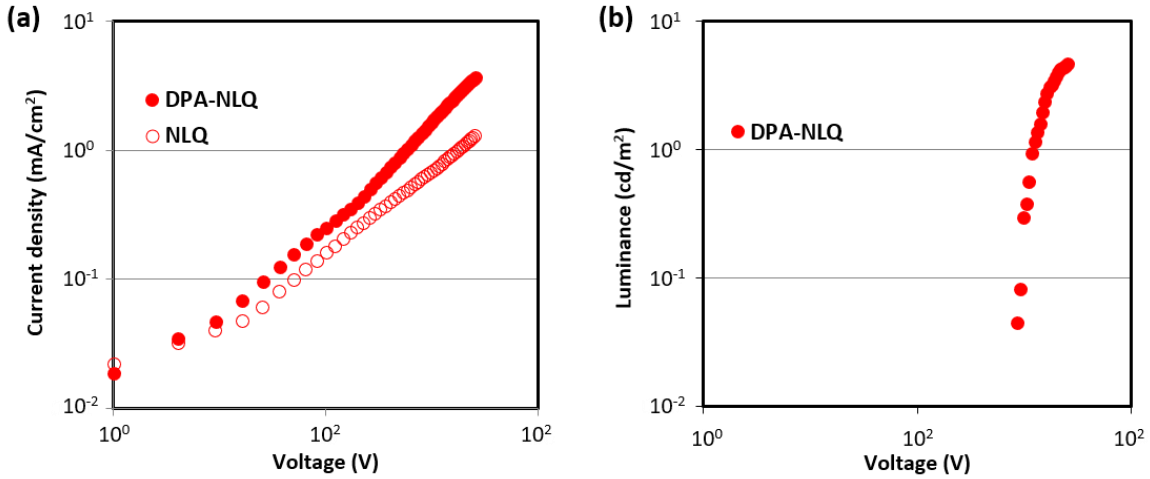

Figure A.10 (a) Current density–voltage characteristics of 2 wt% DPA-doped NLQ and neat NLQ and (b) Luminance–voltage characteristics of 2 wt% DPA-doped NLQ in the microfluidic OLED [1].

A.4. Summary

We developed the novel naphthalene derivative NLQ as a wide-energy-gap LOS host material for deep-blue light emission. The energy gap of NLQ is the largest obtained to date and its PL maximum of NLQ is located at 395 nm as summarized in Fig. A.11. Therefore, NLQ is a potential host material for guest molecules that emit short-wavelength light. A liquid OLED containing NLQ doped with the deep-blue dye DPA as a guest exhibited deep-blue EL emission. This light emission would originate from not only FRET but also direct recombination of trapped holes and electrons. Our results show that NLQ is a promising wide-energy-gap LOS host material for deep-blue light emission in liquid-OLED applications like displays and lighting. However, the proposed LOSs are far from practical use in liquid OLEDs compared to the hosts used in conventional solid-state OLEDs. Further improvement of both LOS materials and device architectures is required for development of liquid-OLEDs.

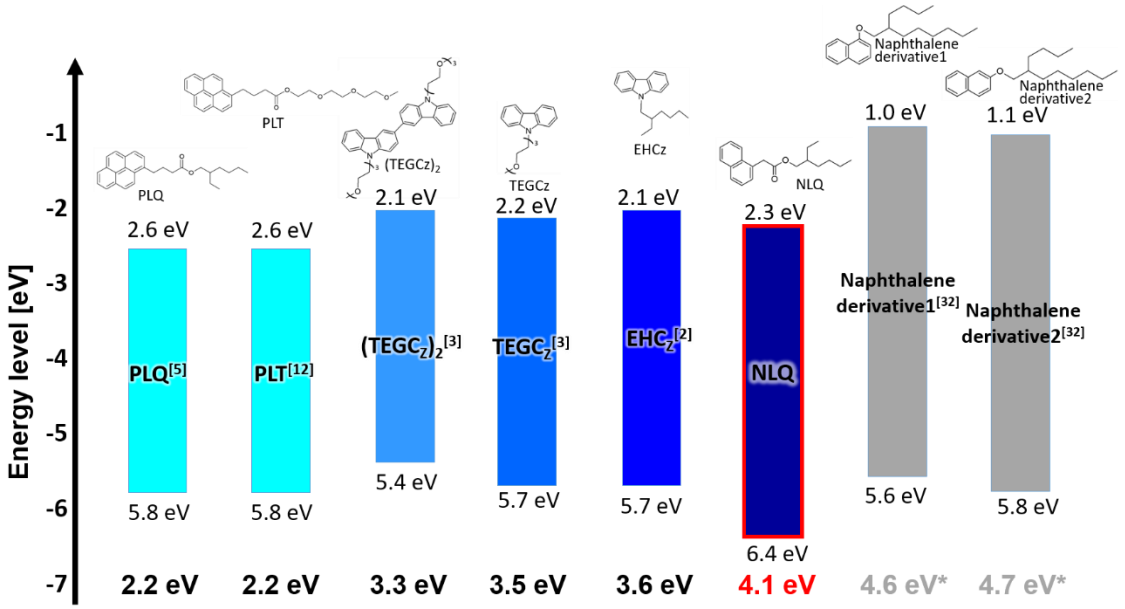

Figure A.11 Energy gap comparison of LOS. Naphthalene derivative1 and 2 show the widest energy gap value, although they are theoretical calculation values. NLQ has the widest energy gap value estimated experimentally.

References

[1] N. Kobayashi, H. Kuwae, J. Oshima, R. Ishimatsu, S. Tashiro, T. Imato, C. Adachi, S. Shoji and J. Mizuno, "A wide-energy-gap naphthalene-based liquid organic semiconductor host for liquid deep-blue organic light-emitting diodes," J. Lumin., vol. 200, pp. 19-23, 2018.

[2] D. Xu and C. Adachi, "Organic light-emitting diode with liquid emitting layer," Appl. Phys. Lett., vol. 95, pp. 207, 2009.

[3] S. Hirata, H. J. Heo, Y. Shibano, O. Hirata, M. Yahiro and C. Adachi, "Improved device lifetime of organic light emitting diodes with an electrochemically stable π-conjugated liquid host in the liquid emitting layer," Jpn. J. Appl. Phys., vol. 51, pp. 041604, 2012.

[4] T. Förster, "Zwischenmolekulare energiewanderung und fluoreszenz," Annalen Der Physik, vol. 437, pp. 55-75, 1948.

[5] T. Kasahara, S. Matsunami, T. Edura, J. Oshima, C. Adachi, S. Shoji and J. Mizuno, "Fabrication and performance evaluation of microfluidic organic light emitting diode," Sens. Actuators. A Phys., vol. 195, pp. 219-223, 2013.

[6] T. Kasahara, S. Matsunami, T. Edura, R. Ishimatsu, J. Oshima, M. Tsuwaki, T. Imato, S. Shoji, C. Adachi and J. Mizuno, "Multi-color microfluidic organic light-emitting diodes based on on-demand emitting layers of pyrene-based liquid organic semiconductors with fluorescent guest dopants," Sens. Actuators B Chem., vol. 207, pp. 481-489, 2015.

[7] T. Kasahara, J. Mizuno S. Matsunami, T. Edura, M. Tsuwaki, J. Oshima, C. Adachi and S. Shoji, "Fabrication and performance evaluation of microfluidic organic light emitting diode," in Transducers 2013, 2013, pp. 2596-2599.

[8] M. Tsuwaki, T. Kasahara, T. Edura, S. Matsunami, J. Oshima, S. Shoji, C. Adachi and J. Mizuno, "Fabrication and characterization of large-area flexible microfluidic organic light-emitting diode with liquid organic semiconductor," Sens. Actuators. A Phys., vol. 216, pp. 231-236, 2014.

[9] N. Kobayashi, T. Kasahara, T. Edura, J. Oshima, R. Ishimatsu, M. Tsuwaki, T. Imato, S. Shoji and J. Mizuno, "Microfluidic white organic light-emitting diode

based on integrated patterns of greenish-blue and yellow solvent-free liquid emitters," Sci. Rep., vol. 5, pp. 14822, 2015.

[10] H. Liu, G. Cheng, D. Hu, F. Shen, Y. Lv, G. Sun, B. Yang, P. Lu and Y. Ma, "A Highly Efficient, Blue - Phosphorescent Device Based on a Wide - Bandgap Host/FIrpic: Rational Design of the Carbazole and Phosphine Oxide Moieties on Tetraphenylsilane," Adv. Funct. Mater., vol. 22, pp. 2830-2836, 2012.

[11] A. Marcello, D. Sblattero, C. Cioarec, P. Maiuri and P. Melpignano, "A deep-blue OLED-based biochip for protein microarray fluorescence detection," Biosens. Bioelectron., vol. 46, pp. 44-47, 2013.

[12] W. -. Liu and W. -. Hao, Opt.Eng., vol. 51, pp. 104001, 2012.

[13] C. Shim, S. Hirata, J. Oshima, T. Edura, R. Hattori and C. Adachi, "Uniform and refreshable liquid electroluminescent device with a back side reservoir," Appl. Phys. Lett., vol. 101, pp. 113302, 2012.

[14] S. S. Babu, J. Aimi, H. Ozawa, N. Shirahata, A. Saeki, S. Seki, A. Ajayaghosh, H. Möhwald and T. Nakanishi, "Solvent - free luminescent organic liquids," Angew. Chem. Int. Ed. Engl., vol. 51, pp. 3391-3395, 2012.

[15] S. S. Babu, M. J. Hollamby, J. Aimi, H. Ozawa, A. Saeki, S. Seki, K. Kobayashi, K. Hagiwara, M. Yoshizawa and H. Möhwald, "Nonvolatile liquid anthracenes for facile full-colour luminescence tuning at single blue-light excitation," Nat. Commun., vol. 4, pp. 1969, 2013.

[16] P. Duan, N. Yanai and N. Kimizuka, "Photon upconverting liquids: Matrix-free molecular upconversion systems functioning in air," J. Am. Chem. Soc., vol. 135, pp. 19056-19059, 2013.

[17] M. Taki, S. Azeyanagi, K. Hayashi and S. Yamaguchi, "Color-tunable fluorescent nanoparticles encapsulating trialkylsilyl-substituted pyrene liquids," J. Mater. Chem. C, vol. 5, pp. 2142-2148, 2017.

[18] F. Lu, T. Takaya, K. Iwata, I. Kawamura, A. Saeki, M. Ishii, K. Nagura and T. Nakanishi, "A Guide to Design Functional Molecular Liquids with Tailorable Properties using Pyrene-Fluorescence as a Probe," Sci. Rep., vol. 7, pp. 3416, 2017.

[19] H. Nakanotani, T. Higuchi, T. Furukawa, K. Masui, K. Morimoto, M. Numata, H. Tanaka, Y. Sagara, T. Yasuda and C. Adachi, "High-efficiency organic light-emitting diodes with fluorescent emitters," Nat. Commun., vol. 5, pp. 4016, 2014.

[20] L. S. Sapochak, A. B. Padmaperuma, P. A. Vecchi, H. Qiao, and P. E. Burrows, "Design strategies for achieving high triplet energy electron transporting host materials for blue electrophosphorescence," in SPIE, Organic Light Emitting Materials and Devices X, 2006, pp. 63330F.

[21] Y. Chen, A. J. H. Spiering, S. Karthikeyan, G. W. M. Peters, E. W. Meijer and R. P. Sijbesma, "Mechanically induced chemiluminescence from polymers incorporating a 1,2-dioxetane unit in the main chain," Nat. Chem., vol. 4, pp. 559-562, 2012.

[22] S. H. Liao, J. R. Shiu, S. W. Liu, S. J. Yeh, Y. H. Chen, C. T. Chen, T. J. Chow and C. I. Wu, "Hydroxynaphthyridine-derived group III metal chelates: Wide band gap and dee blue analogues of green Alq (tris(8-hydroxyquinolate)aluminum) and their versatile applications for organic light-emitting diodes," J. Am. Chem. Soc., vol. 131, pp. 763-777, 2009.

[23] E. R. Triboni, M. R. Fernandes, J. R. Garcia, M. C. Carreira, R. G. S. Berlick, P. B. Filho, L. S. Roman, I. A. Hummelgen, R. Reyes and M. Cremona, "Naphthalimide-derivative with blue electroluminescence for OLED applications," J. Taibah. Univ. Sci., vol. 9, pp. 579-585, 2015.

[24] J. J. Ruiz, A. Aldaz and M. Dominguez, "Mechanism of L ascorbic acid oxidation and dehydro L ascorbic acid reduction on a mercury electrode. I. Acid medium," Can. j. Chem., vol. 55, pp. 2799-2806, 1977.

[25] M. Rueda, A. Aldaz and F. Sanchez-Burgos, "Oxidation of L-ascorbic acid on a gold electrode," Electrochim. Acta, vol. 23, pp. 419-424, 1978.

[26] J. O. Howell, J. M. Goncalves, L. Klasinc, R. M. Wightman, C. Amatore and J. K. Kochi, "Electron Transfer from Aromatic Hydrocarbons and Their p-Complexes with Metals. Comparison of the Standard Oxidation Potentials and Vertical Ionization Potentials," J. Am. Chem. Soc., vol. 106, pp. 3968-3976,

1984.

[27] B. W. D'Andrade, S. Datta, S. R. Forrest, P. Djurovich, E. Polikarpov and M. E. Thompson, "Relationship between the ionization and oxidation potentials of molecular organic semiconductors," Org. Electron., vol. 6, pp. 11-20, 2005.

[28] J. L. Brédas, R. Silbey, D. S. Boudreaux and R. R. Chance, "Chain-Length Dependence of Electronic and Electrochemical Properties of Conjugated S

[29] ystems: Polyacetylene, Polyphenylene, Polythiophene, and Polypyrrole," J. Am. Chem. Soc., vol. 105, pp. 6555-6559, 1983.

[30] H. Meng, J. Zheng, A. J. Lovinger, B. -. Wang, P. G. Van Patten and Z. Bao, "Oligofluorene-thiophene derivatives as high-performance semiconductors for organic thin film transistors," Chem. Mater., vol. 15, pp. 1778-1787, 2003.

[31] S. Sahasithiwat, T. Sooksimuang, L. Kangkaew and W. Panchan, "3,12-Dimethoxy-5,6,9,10-tetrahydro-7,8-dicyano-[5]helicene as a new emitter for blue and white organic light-emitting diodes," Dyes Pigm., vol. 136, pp. 754-760, 2017.

[32] B. Zhao, T. Zhang, B. Chu, W. Li, Z. Su, H. Wu, X. Yan, F. Jin, Y. Gao and C. Liu, "Highly efficient red OLEDs using DCJTB as the dopant and delayed fluorescent exciplex as the host," Sci. Rep., vol. 5, pp. 10697, 2015.

[33] B. Narayan, K. Nagura, T. Takaya, K. Iwata, A. Shinohara, H. Shinmori, H. Wang, Q. Li, X. Sun and H. Li, "The effect of regioisomerism on the photophysical properties of alkylated-naphthalene liquids," Phys. Chem. Chem. Phys., col. 20, pp. 2970-2975, 2018.